Motif-Centered Analyses Reveal Universal and Tissue-Specific Mutagenic Mechanisms Operating in the Human Body

Safia Mahabub Sauty[1], Yun-Chung Hsiao[1], Leszek J. Klimczak[2], Dmitry A. Gordenin[1#]

[1]Genome Integrity and Structural Biology Laboratory, National Institute of Environmental Health Sciences, Durham, NC 27709

[2]Integrative Bioinformatics Support Group, National Institute of Environmental Health Sciences, Durham, NC 27709

#Corresponding author: gordenin@niehs.nih.gov.

Abstract

Somatic mutations are inevitable in human genomes and can lead to tumorigenesis, yet baseline mutagenesis in non-cancerous normal cells remain poorly understood. Here, we analyzed the mutation profiles of 11,949 normal samples across 25 tissues obtained from whole-genome and whole-exome sequencing datasets. We applied stringent statistical hypothesis for detecting enrichment and enrichment-adjusted Minimal Estimate of Mutation Load (MEML) in trinucleotide motifs preferred by known mutagenic processes. We found several cancer-associated mutational motifs in cancer-free tissues. Samples enriched with C→T mutations in nCg motif associated with clock-like spontaneous deamination of meCpG were detected across all tissues. We revealed another clock-like motif, T→C substitutions in aTn motif associated with exposure to small epoxides and other S_N2 electrophiles, in several tissues. Analyses of UV-associated motifs yCn, nTt, and their sub-motifs revealed UV-mutagenesis only in skin. APOBEC-induced C→T and C→G mutations in tCw motif were enriched in bladder, lung, small intestine, liver, and breast with preference for APOBEC3A-like mutagenesis in most. Non-cancerous diseased samples showed significantly higher, age-independent accumulation of aTn and nCg motifs compared to healthy tissues. Together, our analyses elucidated several ongoing mutagenic processes in normal human tissues and provided a robust analytical framework for identifying mutagenic sources from somatic mutation catalogues.

Introduction

Mutations are inevitable in genomes of all species, including humans. Genome sequencing breakthrough more than a decade ago unveiled a massive burden of *de novo* mutations in human cancers (1, 2, 3). Earlier research also led to propose that mutation accumulation in non-cancerous normal somatic cells can be carcinogenic (4, 5). Somatic mutations can also result in disease other than cancer (6, 7, 8). The possible roles of somatic mutagenesis in cancer and other diseases led to questions about the rates and causes of somatic mosaicism and genome instability in humans. Mutation catalogs of somatic cells and tissues can be obtained from conventional whole genome sequencing of cell clones, deep sequencing of micro biopsies, sequencing of multiple single cells from a tissue or by accurate single-molecule sequencing from a non-clonal population of cells derived from a tissue ((9, 10, 11, 12, 13) and references therein). Catalogs of somatic mutations in normal (non-cancerous) human tissues generated in dozens of independent studies were accumulated in the SomaMutDB database (https://vijglab.einsteinmed.edu/SomaMutDB) (14, 15). The collected large volume of mutation data enabled mutational signature extraction to be applied to the entire SomaMutDB dataset, to its' sub-sets including samples from specific tissues, to other datasets and then to use these signatures for addressing specific hypotheses (see e.g., (16, 17)). Agnostic signature extraction turned to be a powerful and popular tool allowing indication of the presence of known as well as yet unknown mutational processes operating in human cancers (3, 18). However, at the very inception of this method it had been stated that "Parameters [of signature deciphering] to which

solutions are sensitive include the number of operative mutational processes, the strength of their exposures, the degree of difference between mutational signatures, the number of analyzed cancer genomes, the number of mutations per cancer genome, and the number of mutation types that are incorporated into the model" (19). These limitations make the determination of the presence of any given signature in an individual sample dependent on other samples of the cohort(s) used for agnostic signature extraction. Moreover, the limitations can be significant in application to signature extraction from the mutational catalogs of normal somatic cells and tissues, where the number of mutations per sample and the sample size of a cohort can be smaller than in cancers. Standard approach with agnostic signatures derived from catalogs of somatic mutations in normal tissues is to align somatic signatures with canonical COSMIC signatures (https://cancer.sanger.ac.uk/signatures/sbs/ (18)) using signature extractor tools and/or calculating cosine similarity (12, 16, 17). This approach allows to highlight presence of some known mutagenic processes but does not assign statistically evaluated P-values to the prevalence of signature(s) in an individual sample.

We previously developed the knowledge-based motif-centered analytical pipeline P-MACD (https://github.com/NIEHS/P-MACD) complimentary to agnostic signature extraction. The pipeline is set to calculate sample-specific enrichment of mutations in trinucleotide motif(s) that have been identified by mechanistic research to be preferred by a single or by a group of related mutagenic factors (see Materials and Methods). The parameters of motif-specific mutagenesis in a sample are just the two odds-ratios, which allows to calculate sample-specific statistics, apply FDR correction, and estimate mutation load caused by a motif-preferring mechanism in each sample of a cohort. Our and others' prior studies have demonstrated several utilities of motif-centered analyses. Motif-specific calculations of enrichment and mutation load were used in several studies in parallel with signature analyses (20, 21, 22, 23, 24, 25, 26, 27, 28, 29, 30, 31, 32, 33, 34, 35, 36, 37, 38, 39, 40). For example, it allowed to distinguish between APOBEC3A and APOBEC3B mutation load in human cancers (36, 37, 38), detect APOBEC mutagenesis in a subset of lung tumor samples from smokers where agnostic extraction did not indicate APOBEC mutagenesis (39), and identify minor UV-induced base substitution and InDel mutational motifs as corroborating evidence for UV-mutagenesis in human skin (40). Motif-centered analyses have also revealed statistically significant presence of a motif identical to COSMIC signature SBS16 in all types of human cancers, while the agnostic extraction assigned SBS16 to only two (at most three) cancer types (41). While the peaks of SBS16 are part of SBS5 which is extracted from all human cancers, SBS16 itself is not extracted from most of cancers where SBS5 was detected (41). Altogether, knowledge-based motif-centered analyses proved useful in several cases, where sample-specific quantitation of the impact of a known mutagenic process in individual samples is sought for.

In this work, we applied motif-centered analyses to mutation catalogues of the vast number of somatic samples curated and made available in SomaMutDB (14, 15). We report findings revealed by motif-centered pipeline applied to mutation catalogs of over ten thousand whole-genome and whole-exome sequenced (WGS and WES) samples from a wide range of normal human tissues obtained from healthy and disease-carrying individuals. We found that enrichment with mechanism-associated motifs previously detected in human cancers also exists in normal tissues. We also revealed association of several motifs with tissue type, donor age, and disease status. The analytical framework presented in our study can be applied to any mutation catalogs of individual somatic samples as well to large sample cohorts.

Materials and methods

Whole genome and exome datasets

Catalogues of somatic mutations in healthy tissues from whole genome and exome sequencing mapped to GRCh38 reference genome were downloaded as VCF (Variant Call Format) files from SomaMutDB (URL: https://vijglab.einsteinmed.edu/SomaMutDB/download/) (14, 15). A general description of VCF file format can be found in (https://docs.gdc.cancer.gov/Data/File_Formats/VCF_Format/). Mutation calls from embryonic stem cells were not included in analyses. Studies reporting mutation calls in donor groups instead of individual samples were also excluded. We also excluded one study reporting variants in endometrium, as the available VCF files only contained indel calls. Catalogues of mutations in diseased tissues from whole genome and exome sequencing mapped to GRCh38 reference genome were downloaded as VCF files from the FAQ section (question 10) of SomaMutDB (URL: https://vijglab.einsteinmed.edu/SomaMutDB/documentation/). Samples with history of carcinoma and chemotherapy were excluded. For single cell brain samples in SMSDB04 and SMSDB33, VCF files were available for the putative, high confidence somatic mutations called by linked-read analysis (LiRA) pipeline and used to estimate SNV/neuron (42, 43). Only 36 out of the 212 individual neurons with available VCF files originating from these two studies were re-called with SCcaller to detect all mutations and were made available in the SomaMutDB database. We used the VCF files reporting the putative mutation catalogues for all 212 neurons to report mutation spectrum and perform sample-specific motif-centered analyses. Neurons from SMSDB04 that were re-analyzed in SMSDB33 were only reported once with the sample IDs from SMSDB04. Mutation calls generated in studies not included in the SomaMutDB database were collected from the Supplementary materials of the cited papers (44, 45, 46) and from associated dbGaP studies (40, 47). Coordinates of mutation calls obtained from Supplementary materials and mapped to GRCh37 reference genome were converted to GRCh38 coordinates using UCSC LiftOver tool (URL: https://genome.ucsc.edu/cgi-bin/hgLiftOver). Overlapping mutation calls were removed for clones and single cells originating from the same donor in the same tissue biospecimen. Duplicate calls were recorded once and were assigned to samples with the highest variant allele frequency where such information was available. All VCF files were converted to MAF (Mutation Annotation Format) files using the vcf2maf tool (URL: https://github.com/mskcc/vcf2maf) to perform motif-centered analysis. A general description of MAF file format can be found in (https://docs.gdc.cancer.gov/Data/File_Formats/MAF_Format/).

Detection of COSMIC SBS signatures in the mutation catalogues of normal tissues

Mutation data for all samples within a tissue or disease group were pooled to generate 96-trinucleotide profiles, which were then refitted with published COSMIC SBS signatures (v3.2) using MutationalPatterns R package (48). A second refitting was performed using SBS signatures contributing >5% of mutations in individual tissue or disease group as the reference set. Relative contribution of signatures in different tissues or disease groups was calculated and plotted. Signature data from *de novo* signature extraction and decomposition utilized for signature-motif correlation were collected from the supplementary materials of previous studies (17, 40, 45, 49, 50).

Detection of enrichment of mutations in trinucleotide motifs and calculation of minimum estimate of mutation load associated with known mutagenic processes

Trinucleotide motifs and their sub-motifs are constructed based on mechanistic knowledge and experimental validation of the mutagenic preferences of the associated mutational processes. Motif-centered analyses to find statistically significant enrichment of specific mutagenic processes were performed using the P-MACD software (URL: https://github.com/NIEHS/P-MACD) as previously described (40, 41, 47, 51). Briefly, enrichment of a mutational motif was calculated by normalizing the incidence of a specific base substitution in a trinucleotide motif to the random incidence of that mutation in the background genomic context. For this calculation, context is

defined as ±20 bases surrounding the mutated base to concentrate on the sequenced part of the genome. This allows to capture only localized effects of lesion formation, TLS, and repair, to avoid epigenomic impacts on mutagenesis in the larger genomic regions within each sample, and to circumvent any regional amplification biases introduced by different sequencing platforms. Reverse complements were included in calculations and motifs were reported as pyrimidine nucleotide of a base pair. The mutated base is shown in capital, and IUPAC codes are used for ambiguous nucleotides. The formula to calculate enrichment is shown below using aTn→aCn mutational motif as an example:

$$Enrichment(aTn \rightarrow aCn) = \frac{[Mutations_{aTn \rightarrow aCn}] \times [Context_t]}{[Mutations_{T \rightarrow C}] \times [Context_{atn}]}$$

We excluded 'complex' mutations, defined as mutations ≤10bp apart, from this calculation as they may arise from the activities of the translesion polymerases and may confound the detection of mutagenic mechanisms with specific motif preferences. We performed one-sided Fisher's Exact test to statistically evaluate the overrepresentation of mutations in a motif over random mutagenesis in individual samples. Ratio of the number of mutations in motif ($Mutations_{(aTn \rightarrow aCn)}$) to mutations that are not in motif (($Mutations_{(T \rightarrow C)}$) - ($Mutations_{(aTn \rightarrow aCn)}$)) were compared to the ratio of the number of bases in the context that conformed to the motif ($Context_{(atn)}$) to bases that did not conform to the motif (($Context_{(t)}$)- ($Context_{(atn)}$)). For samples that show statistically significant enrichment after correction for multiple hypothesis using Benjamini-Hochberg method (enrichment >1, q value ≤0.05), we calculated the minimum estimate of mutation load (referred as MEML) attributable to the mutagenic process associated with the trinucleotide motif. MEML was calculated using the following formula:

$$MEML(aTn \rightarrow aCn) = \frac{[Mutations_{aTn \rightarrow aCn}] \times [Enrichment_{aTn \rightarrow aCn} - 1]}{[Enrichment_{aTn \rightarrow aCn}]}$$

MEML was recorded as zero for samples that did not show statistically significant enrichment of a mutational motif. All figures report sample-specific MEML values unless otherwise indicated.

Statistical analyses and data visualization

All statistical analyses were performed in R statistical software (version 4.4.0) via RStudio. Spearman correlation was performed for all correlation analyses using cor.test() function. Age correlations were performed with average MEML count of all samples originating from a donor. wilcox.test() function was used to perform all tests of significance, followed by correction for multiple hypothesis by Benjamini-Hochberg method using p.adjust() function. Donors in the dataset were divided in three age terciles, and tests of significance were performed for each age group within individual studies that reported both healthy and diseased cohorts to avoid batch effect and minimize the effect of aging in detecting true difference between healthy and diseased tissues. For single cell brain samples in SMSDB04 and SMSDB33, MEML counts calculated by motif-centered analyses of the putative SNVs were prorated by sample-specific multipliers to estimate genome-wide MEML load. Multipliers were calculated as

$$Multiplier = \frac{Estimated\ SNVs}{Total\ Mutations\ Identified}$$

For SMSDB04, numerator values were obtained from the '*Estimated SNVs (per autosomes)*' column and the denominator values were obtained from the '*Total Mutations*

Identified' column of Supplementary_table_S5 (42). For SMSDB33, we used values from Supplementary_table_S6 (43). For numerator of MDA-amplified available VCF files, we used values from column '*Estimated SNVs (per autosomal genome, post-filtering)*' of sheet '*Rates per Neuron (MDA)*'. For numerator of PTA-amplified available VCF files, we used values from column '*Estimated SNVs (per autosomal genome)*' of sheet '*Rates per Neuron (PTA)*'. Values from columns '*Phaseable Mutations Identified*' were used as denominators for all samples from SMSDB33.

Multivariable regression analyses were performed using lm() function using age and disease status as predictor variables and motif-specific MEML as the dependent variable. Unless otherwise indicated, all data visualizations were performed using ggplot2 R package (52) and Adobe Illustrator (53).

Results

Study design

We analyzed the mutation calls from WGS and WES samples of non-cancerous (i.e., normal) human tissues. The mutation calls were retrieved from the somatic mutation database SomaMutDB (https://vijglab.einsteinmed.edu/SomaMutDB) (14, 15), and from the supplementary materials of several papers not included into SomaMutDB (see Materials and Methods) (Supplementary Table S1a). The dataset of mutation calls was categorized into two groups, healthy and diseased normal tissues. The mutation calls in the healthy cohort are from 10,625 samples of 777 individual donors, spread across 25 organs (Supplementary Table S1b). 8,054 of these samples are WGS with total 7,623,352 mutations (sample mutation loads range from zero to 34,629). 2,571 healthy normal samples are WES with total 179,208 mutations (sample mutation loads range from zero to 5,957). Detailed information of both WGS and WES healthy samples, including their mutation loads, are presented in Supplementary Table S1b. The mutation calls in the diseased cohort are from 1,323 samples of 223 Individual donors, spread across 6 tissue types and 15 different disease conditions (Supplementary Table S1c). 1,226 of the diseased samples are WGS (with 3,243,116 total mutations; sample mutation loads range from zero to 18,243) and 96 samples are WES (with total 65,843 mutations; sample mutation loads range from 9 to 2,931). Detailed information of the diseased cohort is available in Supplementary Table S1c.

We first compared the mutation profiles of different normal tissues with the published COSMIC reference SBS signatures derived from large cohorts of cancer mutation catalogs. Then, we performed motif-centered analyses to find enrichment of known mutagenic processes and quantify their presence in individual samples. To conduct motif-centered analyses of the mutation calls, we curated a list of trinucleotide motifs preferred by known mutagenic mechanisms and supported by experimental evidence and mechanistic knowledge (Table 1). In order to resolve potential overlaps between motifs centered around the same base substitution, we built a non-overlapping sub-motif, where needed (Supplementary Table S2).

Table 1: List of knowledge-derived mutational motifs.

Motif name[1]	Reference trinucleotide	Mutant trinucleotide	Motif for SBS correlation	Mechanism	References
aTn	aTn	aCn	aTn→aCn	Epoxide	(41)
yCn	yCn	yTn	yCn→yTn	UV	(40, 47, 54)
nCg	nCg	nTg	nCg→nTg	Spontaneous deamination of meCpG	(40, 47, 55)
nTt	nTt	nCt	nTt→nCt	UV (minor)	(40, 47)
tCw	tCw	tTw	tCw→tTw	APOBEC	(51)
tCw	tCw	tGw	tCw→tGw	APOBEC	(51)
tgC	tgC	tgA	tgC→tgA	Redox	(56))
hTg	hTg	hGg	hTg→hGg	S_N2 alkylation	(57)
aCy	aTy	aCy	aCy→aTy	S_N1 alkylation	(57)
gCn	gCn	gAn	gCn→gAn	Acetaldehyde	(58)
cTg	cTg	cAg	cTg→cAg	Aristolactam (from Aristolochic acid)	(59)

1. Bases within each motif are shown in IUPAC codes

We evaluated statistically significant over-representation of 11 knowledge-based trinucleotide motifs using motif-centered analysis tool P-MACD (https://github.com/NIEHS/P-MACD). P-MACD calculates enrichment of mutations in the trinucleotide context relative to random mutagenesis. It assigns sample-specific P-values and calculates enrichment-adjusted Minimum Estimate of Mutation Load (hereafter referred to as MEML) for samples that have a statistically significant enrichment of mutational motif after correction for multiple-hypothesis testing. By forming a stringent statistical hypothesis and performing sample-specific analyses, we extracted the MEML value that can be attributed to a specific mutagenic mechanism. Conveniently, non-zero MEML value indicates statistically significant enrichment with a motif, so these two terms can be used interchangeably.

Mutation spectrum and the contribution of COSMIC SBS signatures in normal tissues

Dataset of mutations in healthy normal tissues contained a total of 7.8 million single base substitutions (SBS) identified by whole exome or by whole-genome sequencing (hereafter referred as WES or WGS, respectively). Median SBS counts in WGS healthy tissues ranged from 22 to 4,025, while counts in WES healthy tissues ranged from 9 to 499 (Fig. 1A, Supplementary Table S3a). Similar to prior reports of genome-wide mutagenesis in multiple cancer types (1, 3, 18) we observed highest fraction of C to T substitutions across all tissues. Mutation catalogs of normal tissues with noncancer diseases contained 3.3 million substitutions with median SBS count ranging 29 to 6,026 in WGS samples and 35 to 1,135 in WES samples (Fig. S1A, Supplementary Table S3b).

We first performed mutation signature analysis to understand the patterns of mutagenesis in the healthy and diseased tissue cohorts. We limited signature analysis to refitting with published COSMIC SBS signatures and did not perform *de novo* signature extraction due to the extraction method's limitations outlined in the Introduction. We generated 96-channel mutation profiles using all mutation calls from each healthy and disease tissue types and fitted them with COSMIC SBS signatures derived from PCAWG cancer mutation catalogues (18) to estimate the relative contribution of cancer-associated signatures in the mutation loads of normal tissues (Supplementary tables S3c, S3d). In consensus with the originating studies that performed *de novo* signature extractions (17, 45, 49, 50, 60, 61), we detected clock-like signature SBS5 with

no assigned etiology to be the largest contributor in most healthy (18 out of 24) and diseased (10 out of 14) WGS tissue types (Fig 1B, Supplementary Fig. S1B). SBS5 was also detected in two WES healthy tissues (Supplementary Fig. S2A). Another flat signature with no known etiology, SBS40, was readily detected in multiple healthy and diseased WGS tissue types (Fig 1B, Supplementary Fig. S1B). Combined contribution of these two signatures ranged from 0% to 86% of the total mutation pool of different healthy and diseased tissues (Supplementary table S3e).

We detected the contribution of SBS1 associated with meCpG deamination in 17 out of 24 WGS healthy tissues and 9 out of 14 WGS disease types (Fig 1B, Supplementary Fig. S1B, Supplementary tables S3c, S3d). Analyses of WES samples revealed SBS1 in 5 out of 10 healthy and 1 out of 2 disease tissues (Supplementary Fig S2A). UV-associated signatures SBS7a and SBS7b were detected in epidermis and dermis WGS and WES tissues (Fig 1B, Supplementary Fig. S1B, S2A). SBS7b was also detected in stomach, rectum, esophagus, and colon WES tissues where UV-mutagenesis is not expected (Supplementary Fig. S2A). SBS2 and SBS13, signatures associated with deamination by APOBEC enzymes, were detected to have small contributions only in healthy bladder tissue. We noted that the spontaneous deamination of meCpG dinucleotides, which is a known endogenous mutator in human cells, was not reliably identified in all tissues analyzed by signature refitting. In contrast, signatures associated with tissue-specific mutagenesis were reliably detected only in tissues with a high likelihood of exposure, like UV-mutagenesis in skin. Additionally, analyses of WES samples with low number of mutations resulted in assignment of signatures to biologically implausible tissue types. Hence, we proposed that our framework of motif-centered analysis may validate existing mutagenic sources, reveal undetected mechanisms, and quantify sample-specific contributions of known mutagenic sources where signature analysis may be underpowered or unsuitable (see Introduction).

Mutational motifs derived from mechanistic research are enriched in various human tissues and correlate with mutation signatures

We used P-MACD pipeline to assess enrichment of eleven selected trinucleotide mutational motifs in the mutation catalogues of all individual samples. These mutational motifs were previously associated with mutagenic mechanisms indicated in mechanistic studies and were also found in human cancers and in normal human skin (Table 1). Strong experimental support is evident from previous studies for nCg motif characteristic of cytidine deamination in meCpG dinucleotides (55), tCw motifs of APOBEC mutagenesis (51, 62, 63), aTn motif of exposure to small epoxides (41), and yCn motif of UV-mutagenesis (40, 47, 54). We analyzed all WGS samples, as well as WES samples which have 100-fold less mutations compared to the WGS samples.

Analysis of mutational motif enrichment indicated wide-spread presence of the two motifs associated with mutagenic processes in different types of morphologically normal healthy tissues (Fig. 2A). The aTn and nCg, were detected in 4%-100% and 43%-100% of the healthy WGS samples, respectively (Supplementary Table S4a). Statistically significant enrichment with nCg was also detected in 9%-93% of WES samples, while 0%-20% WES samples showed aTn MEML, further validating the robustness of the motif-centered analysis (Supplementary Table S4a, Supplementary Fig. S2B). aTn and nCg were also detected across all diseased tissues (Fig. 2B). aTn was 3-100% of the WGS samples and 4%-12% of the WES samples. nCg MEML was detected in 26%-100% of WGS and 94%-100% of WES diseased samples (Fig. 2B, Supplementary Fig. S2C, Supplementary Table S4b). Other motifs were detected only in some organs and diseased tissues, suggesting tissue-specificity of the underlying mutagenic processes. UV-associated motifs yCn and nTt were detected in multiple tissues with the largest contributions in dermis and epidermis (Supplementary Table S4a, b). C→T and C→G mutations

in APOBEC-associated motif tCw were also detected in multiple tissue and disease types (Supplementary Table S4a, b).

To understand the inter-method agreement between the motif-centered estimates of mutagenesis in mechanistically-linked mutational motifs and mutation load assigned by agnostic extraction of mutation signatures, we sought to perform Spearman correlation analyses between motif MEML and signature exposures for 1,386 healthy samples (1,310 WGS, 76 WES) where sample-specific signature data were reported in the originating studies (17, 40, 45, 49, 50). We performed correlation analyses across all 11 knowledge-derived mutational motifs and all SBS signatures available within each tissue category (Supplementary table S4c). We found that the two ubiquitous motifs aTn and nCg showed significant positive correlation with signatures SBS1 and SBS5 in most tissues analyzed (Fig. 3A, B). Both SBS1 and SBS5 are clock-like signatures (18). SBS1 signature is analogous and mechanistically concordant to the clock-like motif nCg→nTg, whereas SBS5 contains peaks for all 96 trinucleotide motifs including aTn and nCg motifs (Supplementary Fig. S3A). aTn motif has previously been shown to be clock-like in cancers and exhibited significant positive correlations with both SBS1 and SBS5 in the PCAWG cancer cohort (41). The strong correlation of aTn and nCg motifs with both SBS1 (close match to nCg motif) and SBS5 (flat signature) observed in normal cells is likely driven by their shared clock-like properties, as well as partial or total sequence similarity between these motifs and signatures (Fig. 3A, B, Supplementary Fig. S3A). Interestingly, SBS16 signature with close match to aTn motif (Supplementary Fig. S3A) was not detected by agnostic extraction in these samples.

We also detected significant correlations of UV-associated motifs yCn and nTt with UV-associated signatures SBS7a, b, d in dermis and epidermis tissues (Fig. 3C). yCn motif also showed spurious correlations with SBS1 and SBS5 in some tissues, likely due to its complete sequence overlap with nCg motif (Supplementary Fig. S3B). Spurious correlations of nTt motif with SBS1 and SBS5 may be indicative of non-UV lesion motifs that overlap with aTn (Fig. 3C). We detected significant positive correlation between yCn motif and APOBEC-associated signature SBS2 in bladder as well as in dermis (Fig. 3C). This may stem from the overlapping motif preference of UV-induced lesions and APOBEC-mediated deamination of cytosines (see later sections) (Supplementary Fig. S3B). In the same vein, we detected significant correlation between APOBEC-associated motif tCw→tTw with UV-signatures in epidermis (SBS7a, SBS7b, SBS7d) and dermis (SBS7a) (Fig. 3D). We detected significant correlation of both APOBEC-associated motifs with both APOBEC-associated signatures only in WES bladder tissue (Fig. 3D). APOBEC-related tCw→tGw motif aligning with SBS13 showed strong correlations with SBS13 in all tissues where both the motif and the signature were detected. It also correlated with SBS2 reflecting the T→C branch of APOBEC mutagenesis in bladder and in small intestine (Fig. 3D, Supplementary Fig. S3B).

Together, these findings showed that motif analyses can complement signature analyses to cross-validate biological interpretations where signature etiology is understood and offer mechanistic knowledge for signatures with yet unknown etiology (e.g., SBS16). Below we dissect the features of individual motifs in normal healthy tissues and highlight the utility of motif-centered analyses to disentangle confounding mutagenic mechanisms. We then explore association of motif-specific mutagenesis with disease state of noncancer tissues.

The small epoxide mutagenesis motif aTn→aCn is enriched in samples across all human tissues and accumulates along the lifetime.

The aTn→aCn motif (referred to aTn throughout this paper) was experimentally identified as a defining feature of hypermutation caused in a yeast sub-telomeric single-stranded DNA (ssDNA) model system in response to treatment with small epoxide glycidamide – an electrophile reacting with nucleobases via S_N2 mechanism (41). Glycidamide-induced hypermutation in

ssDNA showed clear overrepresentation of A→G substitution in nAt context (T→C in aTn in reverse complement). The base preference of glycidamide showed similarity with the chemical preference of S_N2 reacting electrophiles in ssDNA and with the mutagenic preference of another electrophilic alkylating agent reacting via S_N2 mechanism, methyl methanesulfonate (MMS), supporting the hypothesis about an aTn motif preference not only by small epoxides, but by a broader class of S_N2 reacting electrophiles ((41, 57) and references therein). Analysis of mutation catalogs from PanCancer Analysis of Whole Genomes (PCAWG) (32) detected widespread enrichment and clock-like accumulation of aTn motif in multiple cancer types. Ubiquitous nature of aTn motif further suggested that it may be a feature of a broader class of mutagens instead of glycidamide alone. Prevalence of aTn motif was shown to have strong positive correlations with mutation loads assigned to COSMIC signatures SBS1, SBS4, SBS5 and SBS16 in tumors where these signatures were detected. In cancers with smoking as a risk factor, aTn mutation load showed a strong and significant association with the smoking history of the patients. Smoking-related aTn mutation load in lung tumors largely exceeded age-dependent presumably endogenous level of mutagenesis. Age-dependent aTn accumulation was also detected in healthy skin and brain cells (41).

We detected aTn motif prevalence in morphologically healthy samples across all tissue types. While aTn→aCn MEML contributed only a modest fraction to a median 9.03% (95% confidence interval: 6.7%-10.4%) of total AT pair mutations (A→C, A→G, A→T, including reverse complements), its' statistically significant enrichment was detected in WGS samples across all tissue types (Fig. 4A, Supplementary Table S5a). This indicates the motif's utility for evaluating the level of epoxide- or even broader class of S_N2 electrophile-induced mutagenic exposure. The aTn motif-associated mutagenesis was also detected in WES samples, albeit at lower prevalence as compared to WGS mutation catalogs. Multiple samples showing non-zero aTn MEML were detected in all tissue types except epidermis and heart, (Fig. 4B, Supplementary Table S5b).

T→C substitutions are central to aTn motif, however other mutagenic processes causing the same substitutions can confound statistical evaluation of aTn enrichment. Another motif centered around T→C, nTt→nCt (nTt in abbreviated format) is generated by the error-prone trans-lesion synthesis (TLS) across UV-induced cyclo-pyrimidine dimers (CPDs) formed by two adjacent thymines. It was revealed as a secondary minor UV-associated motif (40, 47, 54). Importantly, aTn motif is a part of nTt motif and vice a versa – i.e. the motifs overlap (See Supplementary Table S2). Such an overlap would not allow an unambiguous assignment of mutagenic mechanism, UV or S_N2 reacting electrophiles, because of mutually confounding effects of respective diagnostic enrichment and MEML estimates of aTn and nTt motifs. This difficulty can be resolved using non-overlapping parts (i.e., sub-motifs) of mutually confounding motifs (Supplementary Table S2). To identify the presence of bona fide aTn contribution into MEML, we performed Spearman correlation tests between MEML counts of the aTn and its sub-motif, aTr (Supplementary Table S5c). In the aTr motif, thymine is followed by either an adenine or a guanine which eliminates any contribution of UV-mediated thymine-thymine dimers of the nTt motif. Significant positive correlation was detected between aTn and aTr MEML across all tissue types except appendix, epidermis, and tonsil (Fig. 4C, Supplementary Fig. S4, S5A). Lack of significant aTn-aTr correlation in epidermis and tonsil can be attributed to the low number of samples with both aTn and aTr MEML (Supplementary Fig. S4, S5A), however confounding effect of other mutagenic mechanisms cannot be excluded, especially in epidermis where UV mutagenesis could occur. Correlation analyses excluding either aTn MEML=0 or aTr MEML=0 further confirms that the strong contribution of aTn MEML in most tissues cannot be explained by confounding UV-mutagenesis (Supplementary Fig. S5A, Supplementary Table S5c).

Next, we asked if the aTn MEML accumulation shows clock-like feature across normal human tissues as previously identified in cancers and in healthy skin (41). We calculated mean

MEML load in each donor and performed spearman correlation analyses with donor age within each tissue (Supplementary Table S5d). We detected significant positive correlation with age in all tissues where aTn and aTr was detected, except in bladder (Fig. 4D, Supplementary Table S5e). Of note, aTr shows a stronger correlation with age than aTn in dermis, suggesting a UV-like component (nTt) that is not age dependent. Correlation analyses between donor age and aTn or aTr MEML excluding zero MEML values reproduced same finding (Supplementary Fig. S5B). Together, our analyses showed similar features of aTn motif in healthy tissues as detected in tumors and generalizes its' cock-like feature to include multiple tissue types.

Clock-like mutagenesis caused by deamination of 5-methylcytosine motif nCg→nTg is highly enriched in multiple human tissues

In mammalian genomes, 70%-80% of the cytosines in CpG dinucleotides (nCg motifs) are methylated, and spontaneous 5-methylcytosine deamination results in C→T substitutions (55). This nCg motif mutagenesis is ubiquitously detected across all tumor types in WES and WGS TCGA the PCAWG catalogs, shows clock-like accumulation, and corresponds with COSMIC signature SBS1 (3, 18).

In our cohort of WGS samples in healthy tissues, we detected nCg MEML across all tissue types with 14.15% median nCg→nTg MEML contribution in total CG-pair mutations (95% confidence interval: 9.6%-20.7%) (Fig. 5A). WES samples showed 15.5% median nCg contribution in CG-pair mutations (95% confidence interval: 3.7%-40.9%) (Fig. 5A) (Supplementary Table S6a). Samples with nCg MEML were detected across all tissue types with sample-specific MEML ranging from zero to 2,010 in WGS samples, and from zero to 1,456 in WES samples (Fig 5B, Supplementary Table S6b). Median nCg MEML detected across WGS samples is 61 (95% confidence interval: 59-63) and that in WES samples is 3 (95% confidence interval: 3-4).

Multiple mutagenic processes cause cytosine deamination in mammalian tissues including CpG deamination, repair of UV-mediated cyclobutane pyrimidine dimers (CPDs), and activities of cytidine deaminases like AID and APOBEC (2). The trinucleotide base composition in nCg motif overlaps with base preference by UV mutagenesis, which forms pyrimidine-pyrimidine dimers in yCn context. To separate the contribution of yCn and detect true nCg MEML in tissues, we used the approach of sub-motif analyses and split the nCg motif into two sub-motifs, rCg and yCg (Supplementary Table S2). The mutable cytosine in rCg is preceded and followed by a purine, therefore excluding the possibility of CPD formation by UV-damage. yCg on the other hand has a pyrimidine preceding the mutable cytosine and can be converted to a thymine by both spontaneous and UV-mediated deamination. Performing Spearman correlation analyses of nCg MEML with both rCg MEML and yCg MEML allowed us to identify tissues that do not show true spontaneous CpG deamination (Supplementary Table S6c). We detected strong positive nCg-rCg and nCg-yCg correlations in all tissues and sequencing groups, except in dermis and epidermis where nCg-rCg correlation is absent (in epidermis) or weaker (in dermis) compared to nCg-yCg correlation (Fig. 5C, Supplementary Fig. S6A, S7A).

Correlation analyses excluding samples that had either motif MEML=0 showed strong nCg-rCg and nCg-yCg correlations in both epidermis and dermis samples (Supplementary Fig. S6B). To further dissect the effect of UV in skin samples, we analyzed the yCh→yTh motif which overlaps with UV-preferred yCn motif but excludes CpG motifs (Supplementary Tables S6b, S6c). We found a very strong nCg-yCh correlation (WGS: Spearman's ρ=0.9, q-value=<0.0001; WES: Spearman's ρ=0.85, q-value=<0.0001) in epidermis samples. Dermis samples showed a moderately strong nCg-yCh correlation (WGS: Spearman's ρ=0.6, q-value=<0.0001). Based on these sub-motif analyses we concluded that the spontaneous deamination of meCpG is detectable but can be heavily confounded by UV-mutagenesis in skin samples.

Next, we investigated the clock-like feature of meCpG deamination as previously detected in cancers (3). For donors with known age, we calculated average donor-specific MEML value for nCg motif and its sub-motifs, yCg and rCg (Supplementary Table S6d). Spearman correlation analyses showed significant positive correlation between donor age and all three motifs (nCg→nTg, rCg→rTg, yCg→yTg) in tissues where true spontaneous meCpG deamination activity was indicated by sub-motif analyses described above (Fig. 5D, Supplementary Fig. S7B, Supplementary Table S6e).

Mutation motifs yCn→yTn and nTt→nCt detected in several tissues can support UV mutagenesis only in skin

UV radiation is a common and potent environmental mutagen that facilitates many types of genome changes including SBSes. UV causes covalent bond formation between two adjacent pyrimidines that results in cyclobutane pyrimidine dimers (CPD) and pyrimidine 6–4 pyrimidone (6-4PP) formation, with CPDs contributing to >80% of the UVB-mediated mutations in mammalian cells (54). C→T mutations in the yCn context are the most frequent result of UV lesions. The yCn→yTn mutations can result from direct error-prone copying of a cytosine within a CPD by TLS polymerases. Importantly, spontaneous deamination of cytosine changing it to uracil is increased several orders of magnitude in CPDs (64) and can result in C→T substitutions after accurate copying by TLS polymerases and another round of replication. Less frequently, thymine in T-T CPDs can be copied by TLS polymerases causing T→C mutations in the nTt context. While less frequent, nTt motif mutations correlate with yCn in normal human skin and in cancers (40, 47).

We detected yCn MEML in dermis and epidermis, where UV-mutagenesis is expected, as well as in bladder, blood, lung, and spleen (Fig. 6A, B). Dermis samples show a high contribution of yCn MEML in CG-pair mutations (22%), second only to epidermis samples (23% in WGS, 31% in WES) (Fig 6A, Supplementary Table S7a). Sample-specific yCn MEML count range from 0 to 9,106 (median: 104, 95% confidence interval: 73-172) in dermis samples (Supplementary Table S7b). Epidermis yCn MEML range 0 to 948 in WGS samples (median: 184, 95% confidence interval: 0-499) and zero to 871 in WES samples (median: 127, 95% confidence interval: 63-252) (Fig. 6B, Supplementary Table S7b). To independently verify UV mutagenesis in tissues where yCn MEML was detected, we performed spearman correlation analyses of yCn MEML with nTt MEML (a minor motif for UV-mutagenesis) and with rCg MEML (a confounding sub-motif of nCg mutagenesis in meCpG) (Supplementary Tables S2 and S7c). There was significant positive yCn-nTt correlation in skin samples and blood, while yCn-rCg significant positive correlation was detected in lung and bladder (Fig. 6C). Removal of samples that does not have a MEML count for either motif showed a significant positive yCn-nTt correlation only in dermis (WGS) and epidermis (WES) (Fig. 6D). Based on the sub-motif analyses we concluded that only skin samples show UV-mediated yCn mutational motif; the source of yCn MEML in other tissues can likely be attributed to spontaneous CpG deamination or other mutagenic processes. We further calculated donor-specific yCn and nTt MEML values for dermis and epidermis (Supplementary Table S7d) and assessed correlation with donor age (Supplementary Table S7e). We do not see age-dependent accumulation of UV mutational motifs in skin, except for negative correlation between nTt MEML and donor age in epidermis (Fig. 6E, Supplementary Table S7e). Since there was only small number of epidermis samples with non-zero nTt MEML, this correlation should be reconfirmed by independent studies.

Motif analyses confirm mutagenesis by APOBEC3A and APOBEC3B in bladder, breast, lung, small intestine, and liver.

APOBEC (apolipoprotein B mRNA-editing enzyme, catalytic polypeptide-like) cytidine deaminases, part of the antiviral innate immunity and RNA editing systems, are also known to cause hypermutation in genomes of human cancers (2, 51, 63, 65). APOBECs cause Cytosine

(C) to Uracil (U) deamination in single-stranded DNA, which can then lead to different base substitution outcomes contingent on processing by the uracil-DNA glycosylases. If no glycosylation occurs, the replicative polymerases can accurately copy the deaminated uracils as thymines and generate C→T mutations. If uracils are cleaved by glycosylation, the resulting AP-sites sites are copied by error-prone TLS polymerases which can lead to either C→T, C→G, or C→A mutations ((66, 67) and references therein). Analyses of large cancer datasets have shown over representation of APOBEC-mediated C→T and C→G mutations in tCw context, with C→A mutations being barely distinguishable from random mutagenesis (51, 63). The tCw→tTw mutational motif closely resembles COSMIC signature SBS2, while tCw→tGw is analogous to SBS13 (3, 18, 51). APOBEC-induced tCw mutational motif enrichment, as well as mutation clusters (also referred as kataegis) have been identified in multiple cancer types (18, 51, 62, 65, 68). Signature analyses have also identified APOBEC mutagenesis in several healthy tissues (16, 17, 49).

We detected enrichment of tCw mutational motif across several tissues in our dataset. tCw MEML (including tCw→tTw and tCw→tGw) contributed 0% to 11% of total CG-pair mutations in the WGS samples (median: 0% , 95% confidence interval: 0%-0.3%) (Fig. 7A, Supplementary Table S8a). In WES samples, tCw contribution ranged from 0% to 7% of total CG-pair mutations (median: 0%, 95% confidence interval: 0%-0.4%) (Fig. 7A, Supplementary Table S8a). Sample-specific tCw→tTw MEML ranged from 0 to 5,589 in the WGS samples and 0-203 in WES samples (Fig. 7B, Supplementary Table S8b). tCw→tGw MEML ranged from 0 to 854 in WGS samples and 0-97 in WES samples (Fig. 7C, Supplementary Table S8b).

APOBEC-mediated mutations tend to be localized in regions of ssDNA stretches, resulting in clusters of strand-coordinated G or C mutations with inter-mutation distance of $10\text{-}10^4$ bases (62, 63, 65, 69). To further granulate the features of APOBEC mutagenesis, we identified the load and pattern of clustered mutations in our dataset. The percentage of samples with >0 mutation clusters ranged 12%-100% in WGS samples (median: 44%, 95% confidence interval: 33%-70%) and 4%-19% in WES samples (median: 10%, 95% confidence interval: 5%-12%) (Supplementary Table S8c). We then isolated the samples with total cluster count >0 and calculated the mean number of clusters, stratified by tissue and cluster type (Fig. 7D, Supplementary Table S8d). We detected a high bias towards non-coordinated clusters, and some contribution of A- or T-coordinated clusters in all tissue types. The mean number of G- or C- coordinated clusters ranged from 0 to 8 (median range 0-1) in WGS samples; WES samples showed mean 0 to 0.7 (median range 0-1) G- or C- coordinated clusters (Fig. 7D, Supplementary Table S8d).

For the first step of identifying tissues with detectable contribution of APOBEC mutagenesis into mutation load, we defined three specific features as indicators of APOBEC mutagenesis: (i) presence of samples with statistically significant enrichment of combined tCw→tTw and tCw→tGw APOBEC motifs (Supplementary Fig. S8A), (ii) high prevalence of both tCw→tTw and tCw→tGw within G- or C-coordinated clusters in samples showing enrichment with combined APOBEC motif (Supplementary Fig. S8B), and (iii) high prevalence of G- or C-coordinated clusters (Supplementary Fig. S8C). In Supplementary Figure S8, we present additional plots for tissues that satisfied criteria for APOBEC mutagenesis. We identified multiple samples in bladder, breast, lung, liver, and small intestine tissues that showed APOBEC enrichment (Supplementary Fig. S8A). FDR-corrected statistically significant APOBEC enrichment was detected in 18% of bladder, 1% of breast, 0.3% of liver, 24% of lung, and 3% of small intestine WGS samples. In agreement with prior knowledge about APOBEC mutagenesis, there were comparable numbers of tCw→tTw and tCw→tGw mutations in G- or C- coordinated clusters of these tissues, with a small contribution of tCw→tAw mutations (Supplementary Fig. S8B). APOBEC enrichment was also detected in clusters of different sizes in these tissues (Supplementary Fig. S8C). APOBEC enrichment is expected to be less in smaller clusters and

scattered mutations due to a higher chance of these clusters being formed by random mutagenesis in close vicinity. In bladder, we detect multiple clusters across all categories of G- or C- coordinated clusters with an average 3.5-fold APOBEC enrichment. Breast shows one cluster with 5 mutations and low APOBEC enrichment, while other categories of G- or C- coordinated clusters have an average 2.5-fold enrichment. We detected one cluster with 4 mutations and 9-fold APOBEC enrichment in liver samples, while enrichment in other categories of G- or C-coordinated cluster average at 3-fold. Multiple clusters across all categories of G- or C-coordinated mutations were detected in lung and small intestine samples with an average APOBEC enrichment of 3.5-fold. While some of these features were also detectable in dermis samples, APOBEC mutagenesis in G- or C- coordinated clusters was heavily skewed towards tCw→tTw MEML (Supplementary Data S1). Since tCw motif overlaps with UV-preferred yCn motif and causes the same base substitution, we could not distinguish between the contribution of APOBEC and UV mutagenesis in skin samples. In summary, motif-centered analyses lead us to conclude that APOBEC mutagenesis is detectable in samples of normal bladder, breast, liver, lung, and small intestine tissues.

Next, we sought to identify the preference for APOBEC3A (A3A) or APOBEC3B (A3B) in tissues where APOBEC mutagenesis was identified. The A3A have been identified as greater source of cancer mutators, however contribution of A3B is also detectable (36, 38, 51). Experiments in yeast model system, and subsequent analyses of cancer datasets have revealed that hypermutation motif preference is distinguishable between A3A and A3B (36). While A3A prefers ytCa motif (APOBEC-preferred tCa motif preceded by a pyrimidine), A3B prefers rtCa motif (APOBEC-preferred tCa motif preceded by a purine). We calculated the enrichment of both ytCa (A3A-like) and rtCa (A3B-like) motifs across different mutation categories in bladder, breast, liver, lung, and small intestine tissues (Supplementary Fig. S8D, Supplementary Table S8e). Where enrichment of both ytCa and rtCa were statistically significant (Fisher's exact test), we performed Breslow-Day test of homogeneity to compare the odds ratios of the two motif enrichments (Supplementary Table S8f). Bladder, breast, lung, and small intestine showed statistically significant higher ytCa (A3A-like) enrichment than rtCa (A3B-like) across all clustered mutations (Supplementary Fig. S8D). Bladder and lung also showed preference for ytCa (A3A-like) enrichment in scattered and genome-wide mutations. Liver showed a preference for rtCa (A3B-like) enrichment; however, it was not detected to be significantly higher than ytCa (A3A-like) enrichment as both enrichment levels were relatively low compared to the other tissues. Together, our analyses revealed A3A to be the predominant APOBEC mutator in bladder, lung, breast, and small intestine healthy tissue samples.

Increased prevalence of aTn→aCn motif in various noncancer diseases

Next, we sought to compare the prevalence of the knowledge-based motifs in the healthy tissues with the diseased tissue cohorts, which included samples from 6 tissue types and 15 non-cancerous disease categories. We detected aTn motif MEML in brain, colon, liver, lung, and small intestine diseased samples (Fig. 2B, Supplementary Table S9a). Because aTn is an age-dependent motif, we categorized our cohort into three tertiles (0-33.3, 33.4-66.7, 66.8-100 years) of age groups to minimize the confounding effect of age while comparing aTn MEML between healthy and diseased samples using Wilcoxon Rank Sum test. We also only compared tissues originating from the same study within each age group to further minimize batch effect (Fig. 8, Supplementary Table S9b). To further account for the effect of age in different disease conditions, we performed multivariable regression analyses including age and diseases as predictor variables (Supplementary Fig. S9, Supplementary Table S9c). We also performed Spearman correlation analysis between donor age and mean donor MEML to detect clock-like accumulation of aTn MEML in diseased tissues (Supplementary Table S9d).

We did not see any statistically significant difference between healthy and diseased cohorts in the first tercile (0-33.33) of age group, regardless of the disease type. In brain, we detected statistically significant reduction of aTn MEML in samples from donors with Alzheimer's disease (Fig. 8A). Multivariable regression analyses without age categorization identified statistically significant positive effect of Alzheimer's disease on aTn MEML load, while Tourette syndrome showed significant negative effect (Supplementary Fig. S9A). Spearman correlation analyses did not reveal age dependency of aTn accumulation in any brain diseases (Supplementary Table S9d).

In colon, we identified significant positive association of aTn MEML with disease conditions within the two older age cohorts (Fig. 8B). Both Crohn's and ulcerative colitis showed a 2-fold increase in the average aTn MEML within the 33.34-66.7 age group. In the 66.7-100 age group, Crohn's samples showed 4-fold and the ulcerative colitis samples showed 3-fold increase in average aTn MEML. Regression analyses in the whole cohort of colon samples did not detect any significant association of either Crohn's or ulcerative colitis after accounting for the effect of age (Supplementary Fig. S9B). Spearman correlation analyses detected age dependent accumulation of aTn MEML in Crohn's (Spearman's ρ= 0.5, q=0.03) and ulcerative colitis (Spearman's ρ= 0.6, q=<0.001) samples (Supplementary Table S9d).

Lung samples of donors with Chronic Obstructive Pulmonary Disorder (COPD) showed a clear disease-dependent accumulation of aTn MEML (Fig. 8C). Compared to lung samples from healthy donors, samples with COPD showed a 2.5-fold increase in the average aTn MEML within the 33.3-66.7 age group and a 4-fold increase in the 66.7-100 age group. Multivariable regression analyses identified strong positive association of COPD with aTn MEML after accounting for the effect of age (Supplementary Fig. S9C), while no clock-like activity was identified by Spearman correlation analyses (Supplementary Table S9d).

High aTn MEML was detected across all diseased liver samples compared to their healthy counterparts (Fig. 8D). Alcoholic cirrhosis samples showed 2.5-fold increase of average aTn MEML in the second tercile age group and 4-fold increase in the third tercile age group. Non-alcoholic cirrhosis samples were only available in second tercile age group and showed a 2-fold increase in average aTn MEML. Samples with Non-Alcoholic Steatohepatitis (NASH) showed 3-fold aTn MEML increase in the second tercile age group, while samples with Primary Sclerosing Cholangitis (PSC) in the same age group showed 2-fold increase (Fig. 8D). Multivariable regression analysis without age categorization showed strong positive association of all liver diseases except non-alcoholic cirrhosis, while the association of age was no longer significant (Supplementary Fig. S9D). Only donors with NASH (n=5) showed a strong age-dependent accumulation of aTn MEML (Spearman's ρ= 0.9, q=0.004) (Supplementary Table S9d).

Small intestine samples with coeliac disease showed a small but statistically significant reduction of aTn MEML in the second tercile age group, and no effect in the third tercile age group (Fig. 8E). Regression analysis identified age as the strongest predictor of aTn MEML accumulation in small intestine, with coeliac disease showing a negative but statistically insignificant association (Supplementary Fig. S9E). No significant clock-like aTn accumulation was detected by correlation analyses in samples with coeliac disease (Supplementary Table S9d).

Increased prevalence of nCg→nTg motif in various noncancer diseases

We detected nCg MEML in all disease categories across brain, colon, epidermis, liver, lung, and small intestine tissues (Fig. 2B, Supplementary Table S10a). As previously described for healthy samples, we performed spearman correlation analyses between nCg, rCg, and yCg MEML to identify true nCg contribution (Supplementary Table S10b). We detected strong positive correlation of nCg MEML with both rCg and yCg MEML in all disease categories except psoriasis,

a skin disease, which only showed correlation with yCg (Supplementary Fig. S10). We excluded psoriasis from further analyses of association with nCg motif.

We detected significantly high accumulation of nCg MEML in brain tissues of donors with Xeroderma Pigmentosum, while donors with Alzheimer's disease showed a reduction (Fig. 9A). In colon samples, we detected statistically significant 3-fold increase of nCg MEML in both Crohn's and ulcerative colitis diseases across all age terciles (Fig. 9B). In lung samples with COPD, we see an average 3-fold increase of nCg MEML across all age groups (Fig. 9C). In liver, a 4-fold increase of average nCg MEML was detected in donors with alcoholic cirrhosis, 4-fold increase in non-alcoholic cirrhosis, 7-fold increase in NASH, and 6-fold increase in PSC (Fig. 9D). Small intestine samples with coeliac disease showed a modest but significant increase of nCg MEML in the upper age tercile (Fig. 9E).

Multivariable regression analyses after adjusting for the effect of age showed significant positive association of increased nCg MEML with Xeroderma Pigmentosum and Alzheimer's disease in brain, ulcerative colitis in colon, COPD in lung, NASH, PSC, alcoholic and non-alcoholic cirrhosis in liver, and coeliac disease in small intestine tissues (Supplementary Fig. S9, Supplementary Table S10d). Spearman correlation detected clock-like accumulation of nCg MEML only in donors with Tourette's Syndrome and ulcerative colitis (Supplementary Table S10e).

Discussion

In this study, we performed a meta-analysis of the somatic mutation catalogues of cancer-free normal tissues generated in dozens of independent studies to find common sources of mutations. We formed stringent statistical hypotheses to identify the enrichment of expert-curated and experimentally validated mutational motifs preferentially mutated by known mutagenic processes in the mutation catalogues of individual samples. We identified the activities of some known mutagenic mechanisms in expected tissue types, like UV-mutagenesis in skin tissues and clock-like deamination of meCpG motifs across all tissue types. We also found new, ubiquitous motif aTn→aCn associated with exposure to small epoxides and other S_N2 electrophiles across all tissues analyzed. Our previous study had identified this motif to be clock-life in multiple cancers across the PCAWG cancer catalogue (41). Here we show that similar to the spontaneous deamination of methylated CpGs, mutagenesis by exposure to small epoxides accumulates throughout human lifetime and predates diseased states. We also distinguished between the preference for APOBEC3A-like and APOBEC3B-like activity in five tissue types, bladder, breast, lung, liver, and small intestine, where mutagenesis by APOBEC deaminases was detected in this current study and previously reported for both normal and cancerous tissues of some of these organs. These findings were enabled by the application of mutational motif-centered pipeline P-MACD accounting for prior knowledge accumulated in mechanistic research revealing the motif preference of mutagens and the molecular mechanisms of mutagenesis. The following discussion outlines the composition and limitations of the general framework of bioinformatics and statistical analyses that can be utilized for elucidating contributions of endogenous and environmental mutagenic factors into base substitution loads in human tissues.

Framework utilizing knowledge-based motif-centered analyses to dissect the sources of mutagenesis in somatic tissues of individuals

Knowledge produced by prior mechanistic research about distinct trinucleotide motif preference of a mutagenic factor to generate mutations was used for calculating statistically supported enrichment and MEML attributable to the motif-associated mutagenesis. There are only a few trinucleotide motifs so far that have been robustly associated with mutagenic factors (Table 1), but more motifs may be discovered from future efforts of the research community. Since there are only 4 bases and 96 trinucleotide motifs in DNA, a partial overlap, or even complete similarity

between motifs preferred by different mutagens is inevitable. However, information derived from mechanistic research can also be used to identify non-overlapping components of motifs (i.e., sub-motifs) that are expected to be preferentially mutagenized by one out of two or more mechanisms associated with the overlapping motifs (step A, Fig. 10). Motifs and sub-motifs derived from mechanistic knowledge were used to perform motif-centered analyses and generate statistically supported enrichment and MEML values from the mutation catalogs of each individual sample (step B, Fig. 10). In downstream analyses (step C, Fig. 10), these partially interchangeable values were used to explore correlations between different motifs and/or sub-motifs. Revealed correlations and prior mechanistic knowledge were used to resolve ambiguity stemming from motif-motif overlaps. For example, we used correlation between aTn→aCn motif and its sub-motif aTr→aCr, which does not overlap with a minor UV-motif nTt→nCt, to dissect and rule out enrichment of epoxide mutagenesis in epidermis (Fig. 4C). Importantly, mutation load in epidermis was enriched for major UV-motif yCn→yTn, which in turn correlated with the minor UV-motif nTt→nCt (Fig. 6C, D). In general, step of motif and sub-motif construction is aided by correlation analysis applied to motif-motif pairs chosen based on sequence overlap and prior knowledge about mutagens underlying motifs. Sample-specific values produced by motif-centered pipeline can also be utilized in downstream statistical analyses to compare cohorts and perform correlations with the biological features of the samples and donors within cohorts.

Motif-centered analyses can identify mutagenic mechanisms operating universally or in a tissue-specific manner

The most ubiquitous motif identified in multiple samples across all tissue types was nCg→nTg associated with cytosine deamination in 5meCpG (Fig. 2 and Supplementary Fig. S2). The four trinucleotides built into the nCg→nTg mutational motif (C→T mutations in aCg, cCg, gCg, and tCg) mimic the main peaks in COSMIC signature SBS1, a signature reliably extracted by different agnostic signature extraction algorithms in somatic and cancerous tissue types. Both SBS1 signature and nCg→nTg motif are age dependent, conforming to the expectation for endogenous mutational process of non-enzymatic deamination and providing additional assurance in their mechanistic assignment.

Another ubiquitous motif revealed by our analyses in healthy and diseased normal tissues was aTn→aCn associated with mutagenesis by epoxides and other S_N2 reacting electrophiles. Peaks of aTn motif closely matched the peaks of COSMIC signature SBS16 extracted from large PCAWG dataset of human cancer mutations (Supplementary Fig. S3A). However, SBS16 was extracted from only two cancer types (head and neck and liver) (18), while aTn→aCn motif was identified in virtually all cancer types (41). Several studies extracted SBS16 from a limited number of somatic tissue types. SBS16 was found in neurons (46, 70), cirrhotic liver (71), esophagus (17), lung (72), and breast (73). Of note, SBS16 was extracted from breast tissues by only one out of three different signature extraction algorithms utilized, and was reported as a low-confidence signature by the authors (73). SBS16 was also only detected in 3 out 24 healthy tissues and 3 out of 14 diseased tissues by refitting of somatic mutations analyzed in this study with the published COSMIC signatures (Fig 1, Supplementary Fig. S1 and S2). On the contrary, our motif-centered analyses found widespread prevalence of aTn→aCn motif in all tissue types analyzed (Fig 2). In addition, motif-centered analyses utilizing sub-motif construction and motif-motif correlation separated aTn mutagenesis from confounding input of T→C mutations by UV-mutagenesis (Fig. 4C).

Framework of motif centered analysis further proved to be productive in identifying tissue-specific mutation mechanisms, as exemplified by the detection of UV and APOBEC mutagenesis. UV-associated mutational motifs yCn and nTt were used based on prior mechanistic evidence and were found only in skin (Fig. 6). Sub-motif analyses allowed to rule out UV-like mutagenesis

as confounded by other mechanisms in several other tissues where yCn motif was detected. Peaks corresponding to trinucleotide motifs yCn and nTt are detectable among the 96-motif spectra of UV-associated COSMIC signatures SBS7a,b and SBS7c,d, respectively, however other peaks were also present in these signatures (Supplementary Fig. S3B). Trinucleotides in APOBEC-associated motif tCw→tTw corresponds to SBS2, while tCw→tGw corresponds to SBS13 peaks (Supplementary Fig. S3B). Motif-centered analyses identified APOBEC mutagenesis in bladder, liver, lung, breast, and small intestine (Fig. 7, Supplementary Fig. S8), as opposed to signature refitting which identified low contribution of SBS2 and SBS13 only in bladder. (Fig 1B, Supplementary table S3c). Construction of tetranucleotide motifs based on prior knowledge about motif preference by APOBEC3A and APOBEC3B (36) allowed the assignment of APOBEC3A as the predominant mutator in tissues where APOBEC mutagenesis was identified (Supplementary Fig. S8), an outcome not achievable by signature analyses.

We also detected sporadic presence of some motifs in multiple tissues and diseases. Samples with enrichment of gCn→gAn motif, which is associated with acetaldehyde exposure and found primarily enriched in liver cancers (58), were detected in multiple somatic tissue types analyzed in our study (12 out of 24; Fig. 2, Supplementary table S4). cTg→cAg motif associated with exposure to aristolochic acid (AA) was detected in healthy colon and bladder, and in both healthy and diseased samples of liver and lung (Fig. 2, Supplementary table S4). SBS22a and SBS22b are associated with AA exposure and contain peaks mimicking cTg→cAg motif among other peaks. SBS22 has been extracted from cancers in upper urinary tract, liver, kidney, and from lung cancer in never-smoking East Asian individuals (74, 75). SBS22 was also extracted from three healthy liver tissue donors and from donors with alcohol-related liver diseases (60, 71). To our knowledge, this is the first indication of AA-induced mutagenesis in normal lung tissues.

We note that the estimated motif-associated MEML can be reduced by the number of mutational mechanisms operating and preferentially mutagenizing the same base in a sample. However, calculation of the minimum estimate of mutation load in a motif provides a baseline value associated with a mutagenic process that can be compared against the baseline value in another sample. Further limitations of motif-centered analyses are due to the restrictive availability of knowledge about high confidence, experimentally validated motifs and the unavoidable overlap between some motifs that cannot be resolved by sub-motif approach. Signature extraction method on the other hand has unique capability to find new mutation patterns amenable for hypothesis generation. We therefore view both approaches as complementary and essential in identifying and validating sources of somatic mutations.

Motif-specific mutational burdens can serve as indicators of an individual's inherited susceptibilities and cumulative exposures over the lifespan

We explored all motifs and all datasets for potential association between somatic mutagenesis and disease, and found several diseases associated with higher prevalence of motif-specific mutation burdens caused by deamination of 5meCpG and/or exposure to small epoxides (Table 2).

Table 2. Summary of somatic mutagenesis in non-cancer diseases compared to their corresponding healthy tissues detected by motif-centered analyses

Tissue	Disease name	Disease specific physiology	Small epoxide associated mutagenesis (aTn→aCn)	Spontaneous deamination of meCpG (nCg→nTg)
Brain	Alzheimer's disease	Amyloid plaques and tau tangles (not fully understood)	- Decreased mutation	- Decreased mutation[1]
Brain	Xeroderma Pigmentosum[2]	DNA repair defect		- Increased mutation
Brain	Tourette's Syndrome	Neurotransmitter disruption (not fully understood)		- Clock-like[3]
Colon	Crohn's disease	Chronic inflammation; autoimmune	- Clock-like[3] - Increased mutation[4]	- Increased mutation
Colon	Ulcerative colitis	Chronic inflammation; autoimmune	- Clock-like[3] - Increased mutation[5]	- Clock-like[3] - Increased mutation
Lung	Chronic Obstructive Pulmonary Disease	Chronic inflammation	- Increased mutation	- Increased mutation
Liver	Alcoholic Cirrhosis	Chronic inflammation, fibrosis	- Increased mutation	- Increased mutation
Liver	Non-Alcoholic Cirrhosis	Chronic inflammation, fibrosis		- Increased mutation
Liver	Non-Alcoholic Steatohepatitis	Chronic inflammation, fat accumulation	- Clock-like[3] - Increased mutation	- Clock-like[3] - Increased mutation
Liver	Primary Sclerosing Cholangitis	Chronic inflammation; autoimmune	- Increased mutation	- Increased mutation
Small intestine	Coeliac	Autoimmune reaction to gluten	- Decreased mutation[6]	- Increased mutation[7]

[1] In upper age tercile of one study
[2] Non-neurological disease caused by defect in global nucleotide excision repair (NER)
[3] In the diseased cohort of the specified tissue
[4] In median age tercile
[5] In median and upper age terciles
[6] In lower age tercile
[7] In upper age tercile

Importantly, increased mutagenesis in some diseases was found for only one out of the two ubiquitous clock-like motifs which suggested an involvement of disease-specific physiological causes as opposed to a strictly age-dependent increase in mutagenesis. Several diseases associated with motif-specific mutagenesis are also associated with increased inflammation. The excess of mutations in non-neoplastic inflammatory diseases can stem from a higher rate of exposure and DNA damage compared to healthy tissues. Continued exposure to xenobiotic sources of DNA damage, like smoking in COPD patients and alcohol consumption in cirrhosis patients, increases the load of mutagenic lesions. Xenobiotic precursors can be endogenously metabolized into reactive small epoxides by CYP2E1 and other CYP epoxygenases primarily in the liver and released back into the body (76, 77). Reactive oxygen and nitrogen species (RONs) produced in inflammatory diseases can overwhelm the DNA damage repair pathways and interfere with DNA repair efficiency (78). Reactive oxygen species may further promote deamination of meCpG dinucleotides (79).

We detected a high burden of meCpG mutagenesis, but not of small epoxide motif mutagenesis, in the neurons of donors with Xeroderma Pigmentosa carrying mutations in XPA or XPD which eliminate the capacity for global nucleotide excision repair (NER) of bulky DNA lesions (80). However, U:G mis-pair created by meCpG deamination is a substrate for base-excision repair or for non-canonical mismatch repair, rather than for NER (81). Future mechanistic studies may shed light on this apparent inconsistency.

The effect of age and disease on somatic mutagenesis in normal tissues can also be supplemented by the impact of individuals' genotype, which is well-established in cancers (82) and has also been shown for several normal tissues (83, 84). Specifically, impact of germline genotype was established on mutagenic processes in cancers that are associated with somatic mutagenesis motifs nCg (meCpG deamination) and tCw (APOBEC) revealed in this study. Germline and somatic variants in mismatch repair complex MutSα are associated with hypermutation of meCpG motifs in cancers (85). Germline mutant alleles of meCpG binding glycosylase MBD4 also predispose to meCpG mutagenesis in cancers (32, 86, 87). Common polymorphisms in APOBEC3 gene cluster cause predisposition to cancer and exacerbate APOBEC mutation load in tumors (26, 32, 88, 89). Thus, motif-associated mutations can be utilized as a phenotype for germline association studies to identify predisposition and vulnerability to specific mutagenic processes.

Since motif-specific somatic mutagenesis are mechanistically linked to their sources, it allows quantification of the activities of endogenous and environmental factors that increase somatic mutation burden. Detection and monitoring of these mutagenic activities in normal tissues can prompt early diagnosis of cancer and non-cancerous diseases, which in turn may facilitate disease prevention, management, and improved treatment outcomes.

Data access

All mutation calls analyzed in this study are available to download in VCF format at https://vijglab.einsteinmed.edu/SomaMutDB/download/ or in the supplementary material of the indicated papers. All data generated in this study, including numerical values underlying figures and the summary statistics are in the Supplementary Tables. P-MACD output for APOBEC cluster analyses are available in Supplementary Data S1. P-MACD package to perform motif-centered analyses is deposited at https://doi.org/10.5281/zenodo.8018096 ; all versions of P-MACD and future updates are available at https://github.com/NIEHS/P-MACD.

Acknowledgements

This work was supported by the NIH, National Institute of Environmental Health Sciences Intramural Research Program Project Z1AES103266 to D.A.G. The contributions of the NIH authors are considered Works of the United States Government. The findings and conclusions presented in this paper are those of the authors and do not necessarily reflect the views of the NIH or the U.S. Department of Health and Human Services. We are thankful to Dr. Ashley Brooks for help with vcf2maf tool, to Dr. Min Shi for consultation on multivariable regression analyses, to Drs Rajula Alleva-Elango and Natalya Degtyareva for advice on manuscript, and to Lois Wyrick for help with illustrations.

Author contributions

S.M.S- Conceptualization (Lead), Data curation (Lead), Formal analysis (Lead), Investigation (Equal), Methodology (Equal), Software (Supporting), Visualization (Lead), Writing - original draft (Lead), Writing - review & editing (Lead)

Y.-C.H. – Formal analysis (Supporting), Software (Supporting)

L.J.K. – Software (Lead)

D.A.G. – Conceptualization (Lead), Formal analysis (Supporting), Funding acquisition (Lead), Investigation (Equal), Methodology (Equal), Project administration (Lead), Supervision (Lead), Writing - original draft (Equal), Writing - review & editing (Equal)

Funding

This work was supported by the US National Institutes of Health Intramural Research Program Project Z1AES103266 to D.A.G.

Conflict of interest

The authors declare no conflict of interest.

Figure legends

Figure 1: Somatic mutation spectra and contribution of COSMIC signatures in healthy tissues. **A**. Median counts for each base substitution including reverse complements are shown in descending order for healthy WGS and WES samples. **B.** Relative contributions of published COSMIC signatures in the mutation profiles of WGS healthy tissues. All source data are available in Supplementary Table S3.

Figure 2: Prevalence of knowledge-based motifs in normal tissues. The percentages of samples with zero and non-zero MEML counts for the 11 known mutational motifs are shown for (**A**) healthy and (**B**) diseased tissues. Only WGS samples are shown. WES samples are shown in Supplementary Fig. S3. All source data are available in Supplementary Table S4a, b.

Figure 3: Correlation between mutational motifs and signatures. Correlation matrix showing Spearman's *ρ* for agnostically extracted COSMIC SBS signatures vs mutational motifs associated with **(A)** exposure to small epoxides and S_N2 electrophiles (aTn→aCn), **(B)** spontaneous deamination of meCpG (nCg→nTg), **(C)** UV-mutagenesis (yCn→yTn and nTt→nCt), and **(D)** APOBEC-mutagenesis (tCw→tTw and tCw→tGw) for healthy tissues indicated on y-axis. Numbers in parenthesis indicate total number of samples in different tissue types. Grey boxes indicate statistically insignificant correlations after correction for multiple hypothesis using Benjamini-Hochberg method. All source data are available in Supplementary Table S4c. Profiles of COSMIC signatures used for correlations with motifs are shown on Figure S3.

Figure 4: aTn mutational motif in healthy normal cells. A. The fraction (%) of aTn→aCn MEML within total AT-pair mutations (T→A, T→C, T→G, and reverse complement) is shown on Y-axis. The tissue types are plotted on X-axis. Left panel – WGS samples; right panel – WES samples. The total aTn MEML count for a tissue is shown above the respective bars. **B**. Sample-specific aTn→aCn MEML counts shown in jitter plots. X-axis indicates tissue types; labels above panels indicate WGS and WES groups. **C**. Correlation matrix showing aTn→aCn MEML versus aTr→aCr MEML to identify true aTn mutational motif. Spearman correlations were performed between sample-specific aTn and aTr MEML counts, including MEML=0 for either motif. Grey circles indicate P value >0.05 after correction for multiple hypothesis using Benjamini-Hochberg method within each sequencing group (WGS or WES). No circles indicate insufficient samples with MEML>0 for a tissue type to perform correlation analyses. **D.** Correlation matrix showing donor age versus mean donor MEML of aTn and aTr motifs. Spearman correlations were performed between donor age and mean MEML count of all samples from an individual donor for the indicated tissues and mutational motifs, including MEML=0 for both motifs. Grey circles indicate P value >0.05 after correction for multiple hypothesis using Benjamini-Hochberg method for a given motif within each sequencing group (WGS or WES). No circles indicate insufficient individual donors with mean MEML>0 for to perform correlation analyses. All source data and statistical analyses can be found in Supplementary Table S5.

Figure 5: nCg mutational motif in healthy normal cells. A. The fraction (%) of nCg→nTg MEML count within total CG-pair mutations (C→A, C→G, C→T, and reverse complement) is shown on Y-axis. The tissue types are plotted on X-axis. Left panel – WGS samples; right panel

– WES samples. The total nCg MEML count for a tissue is shown above the respective bars. **B.** Sample-specific nCg→nTg MEML counts shown in jitter plots. X-axis indicates tissue types; labels above panels indicate WGS and WES groups. **C.** Correlation matrix showing nCg→nTg MEML versus rCg→rTg MEML, and nCg→nTg MEML versus yCg→yTg MEML, to identify true nCg mutational motif. Spearman correlations were performed between sample-specific nCg, rCg, and yCg MEML counts, including MEML=0 for either motif. Grey circles indicate P value >0.05 after correction for multiple hypothesis using Benjamini-Hochberg method within each sequencing group (WGS or WES). No circles indicate insufficient samples with MEML>0 for a tissue type to perform correlation analyses. **D.** Correlation matrix showing donor age versus mean donor MEML of nCg, rCg, and yCg motifs. Spearman correlations were performed between donor age and mean MEML count of all samples from an individual donor for the indicated tissues and mutational motifs, including MEML=0 for both motifs. Grey circles indicate P value >0.05 after correction for multiple hypothesis using Benjamini-Hochberg method for a given motif within each sequencing group (WGS or WES). No circles indicate insufficient individual donors with mean MEML>0 for to perform correlation analyses. All source data and statistical analyses can be found in Supplementary Table S6.

Figure 6: UV mutational motifs in healthy normal cells. A. The fraction (%) of yCn→yTn MEML count in total CG-pair mutations (C→A, C→G, C→T, and reverse complement) is shown on Y-axis. The tissue types are plotted on X-axis. Left panel – WGS samples; right panel – WES samples. The total yCn MEML count for a tissue is shown above the respective bars. **B.** Sample-specific yCn→yTn MEML counts shown in jitter plots. X-axis indicates tissue types; labels above panels indicate WGS and WES groups. **C.** Spearman correlation matrix showing correlations of sample-specific values of yCn→yTn MEML versus nTt→nCt MEML, and yCn→yTn MEML versus rCg→rTg MEML to eliminate confounding effects of overlapping motifs and to support hypothesis about minor UV-motif contribution of UV-mutagenesis in tissue groups that contained samples with yCn MEML. Grey circles indicate P value >0.05 after correction for multiple hypothesis using Benjamini-Hochberg method within each sequencing group (WGS or WES). No circles indicate insufficient samples with MEML>0 for a tissue type to perform correlation analyses. Samples with MEML=0 for either motif was included. **D**. Same as **C**, but samples with MEML=0 for either motif were excluded. **E.** Mean of nTt MEML values (including MEML=0) for samples from epidermis of each donor plotted against donor age. Only epidermis, but not dermis, showed statistically significant correlation after correction for multiple hypotheses testing (Spearman's ρ= -0.8, q=0.03). All source data and statistical analyses for all tissue types can be found in Supplementary Table S7.

Figure 7: APOBEC tCw mutational motif in healthy normal cells. A. The fraction (%) of tCw→tTw and tCw→tGw MEML count in total CG-pair mutations (C→A, C→G, C→T, and reverse complement) is shown on Y-axis. The tissue types are plotted on X-axis. Left panel – WGS samples; right panel – WES samples. The total tCw MEML count for a tissue is shown above the respective bars. **B.** Sample-specific tCw→tTw MEML counts shown in jitter plots. X-axis indicates tissue types; labels above panels indicate WGS and WES groups. **C.** Sample-specific tCw→tGw MEML counts shown in jitter plots. X-axis indicates tissue types; labels above panels indicate WGS and WES groups. **D.** Mean number of mutation clusters for samples with total number of clusters >0 in a tissue type. All source data and statistical analyses can be found in Supplementary Table S8.

Figure 8: aTn motif in diseased tissues. aTn MEML in healthy and diseased samples are shown in a boxplot for brain **(A**), colon **(B)**, lung **(C)**, liver **(D)**, and small intestine **(E)**. X-axes indicate age groups where samples were available. Labels above panels indicate source study of the samples. Only WGS samples are shown. Asterisks in boxplots represent statistical significance (Wilcoxon Rank Sum test) compared to the healthy samples within each study and age group. *P

value ≤ 0.05, **P value ≤ 0.01, ***P value ≤ 0.001. All source data and statistical analyses can be found in Supplementary Table S9.

Figure 9: nCg motif in diseased tissues. nCg MEML in healthy and diseased samples are shown in a boxplot for brain **(A)**, colon **(B)**, lung **(C)**, liver **(D)**, and small intestine **(E)**. X-axes indicate age groups where samples were available. Labels above panels indicate source study of the samples. Only WGS samples are shown. Asterisks in boxplots represent statistical significance (Wilcoxon Rank Sum test) compared to the healthy samples within each study and age group. *P value ≤ 0.05, **P value ≤ 0.01, ***P value ≤ 0.001. All source data and statistical analyses can be found in Supplementary Table S10.

Figure 10: Framework of analyses performed in this study. A. Motifs and sub-motifs are constructed based on mechanistic knowledge about the trinucleotide preference of different mutagenic processes. **B.** Motif-centered analyses are performed on the mutation catalogue of each sample to detect enrichment and MEML attributable to the associated mutagenic process. **C.** Enrichment and MEML values are utilized in downstream analyses to find correlations with other motifs, sub-motifs, and with the features of individual samples and donors, and to perform comparisons between different cohorts.

Supplementary information

Supplementary figures

Supplementary Figure S1. Somatic mutation spectra and contribution of COSMIC signatures in diseased tissues. **A**. Median counts for each base substitution including reverse complements are shown in descending order for diseased WGS and WES samples. **B.** Relative contributions of published COSMIC signatures in the mutation profiles of WGS diseased tissues. All source data are available in Supplementary Table S3.

Supplementary Figure S2. SBS signatures and mutational motifs in exome-sequenced samples. **A.** Relative contributions of published COSMIC signatures in the mutation profiles of WES samples are shown for healthy and diseased tissues. **B-C**. The percentages of samples with zero and non-zero MEML counts for the 11 known mutational motifs calculated for WES samples in healthy **(B)** and diseased **(C)** tissues. Source data are available in Supplementary Tables S3 and S4.

Supplementary Figure S3. COSMIC signature profiles and correlating motifs. Plots displaying mutation profiles for GRCh38 with assigned etiologies were downloaded from COSMIC website and shown for signatures **(A)** SBS1, SBS5, SBS16, **(B)** SBS7a, SBS7b, SBS2, and SBS13. Motifs correlating with the signatures are indicated on each plot with vertical bars under corresponding motif peaks in signature spectra. Bar colors indicate individual motifs.

Supplementary Figure S4. Analysis of aTn→aCn sub-motifs to detect true presence of aTn motif in healthy tissues. Scatter plots showing aTn motif MEML plotted against aTr motif MEML in WGS samples across different tissues. Blue line indicates line of best fit from a simple linear model.

Supplementary Figure S5. Analyses of aTn motif and sub-motifs in samples with non-zero MEML values. A. Correlation matrix showing Spearman correlation between aTn→aCn MEML and aTr→aCr MEML excluding either MEML =0 to identify true aTn mutational motif. Grey circles indicate P value >0.05 after correction for multiple hypothesis using Benjamini-Hochberg method within each sequencing group (WGS or WES). No circles indicate insufficient samples with MEML>0 for a tissue type to perform correlation analyses. **B.** Correlation matrix showing donor age versus mean donor MEML of aTn and aTr motifs excluding either MEML=0. Spearman

correlations were performed between donor age and mean MEML count of all samples from an individual donor for the indicated tissues and mutational motifs. Only tissues with sufficient number of donors to support age-correlation analyses are shown. Grey circles indicate P value >0.05 after correction for multiple hypothesis using Benjamini-Hochberg method for a given motif within each sequencing group (WGS or WES). No circles indicate insufficient individual donors with mean MEML>0 for to perform correlation analyses. All source data and statistical analyses can be found in Supplementary Table S5.

Supplementary Figure S6. Analysis of nCg→nTg sub-motifs and their correlation with each other in healthy tissues. A. Scatter plot showing nCg→nTg MEML plotted against MEML of sub-motif rCg→rTg, the component of nCg non-overlapping to UV-motif yCn, in WGS samples across different tissues. Blue line indicates line of best fit from a simple linear model. **B.** Correlation matrix showing Spearman correlation of nCg→nTg with sub-motifs rCg→rTg (UV non-overlapping) and yCg→yTg (UV overlapping), excluding either MEML =0. Grey circles indicate P value >0.05 after correction for multiple hypothesis using Benjamini-Hochberg method within each sequencing group (WGS or WES). No circles indicate insufficient samples with MEML>0 for a tissue type to perform correlation analyses. C. Scatter plot showing nCg→nTg MEML plotted against MEML of yCh→yTh, the component of UV-motif yCn non-overlapping to nCg, in WGS samples of dermis and epidermis. Blue line indicates line of best fit from a simple linear model. All source data and statistical analyses can be found in Supplementary Table S6.

Supplementary Figure S7. Analysis of nCg→nTg sub-motifs and their correlations with donor age in healthy tissues. A. Scatter plot showing nCg→nTg MEML plotted against MEML of sub-motif yCg→yTg, the component of nCg overlapping to UV-motif yCn, in WGS samples across different tissues. Blue line indicates line of best fit from a simple linear model. **B.** Correlation matrix showing Spearman correlation of donor age with donor-specific mean MEML value for nCg→nTg and sub-motifs rCg→rTg (UV non-overlapping) and yCg→yTg (UV overlapping), excluding either MEML =0. Grey circles indicate P value >0.05 after correction for multiple hypothesis using Benjamini-Hochberg method within each sequencing group (WGS or WES). No circles indicate insufficient samples with MEML>0 for a tissue type to perform correlation analyses. All source data and statistical analyses can be found in Supplementary Table S6.

Supplementary Figure S8: Tissues with multiple features indicating APOBEC mutagenesis. A. Fold-enrichment of APOBEC mutagenesis motif over the expected occurrence of random mutagenesis in the indicated tissues. Samples are categorized into color coded bins based on their FDR corrected q-values (Benjamini-Hochberg) and fold enrichment values. Fold enrichment bin sizes are increments of 1 unit. All samples displaying a q-value >0.05 are placed in one bin (black) regardless of the fold APOBEC enrichment in the sample. The maximum fold enrichment for each bin is indicated in the figure legend, with the number of samples in its category shown in parentheses. **B.** The number of mutations categorized into three possible types of substitutions at the tCw motif (complementary mutations included) within C- or G-coordinated clusters in the indicated tissues. **C.** Fold enrichment of the APOBEC motif mutations in clusters of different sizes of two categories – C- or G-coordinated, non-coordinated, as well as in non-clustered (scattered) mutations in the indicated tissues. Values above the bars display the total number of mutation clusters in each class and in parentheses the total numbers of APOBEC motif mutations in a category. **D.** Enrichment of ytCa (APOBEC3A-like) motif and rtCa (APOBEC3B-like) motif among genome-wide, scattered, clustered, and G- or C- coordinated clustered mutations in the indicated tissues. The blue dashed vertical line indicates level of no enrichment. Where enrichment of both ytCa and rtCa motifs were statistically significant (Fisher's Exact P-value ≤0.05), Breslow-Day test of homogeneity was performed to compare the odds ratios of the two motif enrichments. Asterisks indicate significant difference at P-value ≤0.05. Source data for plots **A**, **B**, and **C** are available in

Supplementary Data S1. Source data and statistical analyses for ytCa and rtCa enrichment **(D)** can be found in Supplementary Table S8e and S8f.

Supplementary Figure S9. Multivariable regression analyses of aTn and nCg motifs in non-cancer diseases. *β*-coefficients from multivariable regression analyses using donor age and disease status as predictor variables are plotted for brain **(A)**, liver **(B)**, colon **(C)**, lung **(D)**, and small intestine **(E)**. *P value ≤ 0.05, **P value ≤ 0.01, ***P value ≤ 0.001. Source data are available in Supplementary Tables S9c and S10d.

Supplementary Figure S10. Analyses of sub-motifs to detect true spontaneous meCpG cytosine deamination-mediated nCg→nTg in diseased tissues. Correlation matrix showing Spearman correlation of nCg→nTg with sub-motifs rCg→rTg (UV non-overlapping) and yCg→yTg (UV overlapping), including MEML = 0 **(A)** and excluding pairs with either member's MEML =0 **(B)** in different disease categories. Grey circles indicate P value >0.05 after correction for multiple hypothesis using Benjamini-Hochberg method within each sequencing group (WGS or WES). No circles indicate insufficient samples with MEML>0 for a tissue type to perform correlation analyses. Source data are available in Supplementary Table S10b.

Supplementary Tables

Supplementary Table S1: Origins of mutation calls for samples analyzed in this study.

Supplementary Table S2: Sub-motifs of knowledge-based motifs with overlapping and non-overlapping components.

Supplementary Table S3: Somatic mutation spectra and COSMIC SBS signatures in normal cells. Contains numeric values underlying Figure 1, Supplementary Figures S1, S2a.

Supplementary Table S4: Prevalence of knowledge-based motifs in normal tissues. Contains numeric values underlying Figures 2, 3, Supplementary Figure S2b.

Supplementary Table S5: aTn mutational motif in normal healthy cells. Contains numeric values underlying Figure 4, Supplementary Figures S4, S5.

Supplementary Table S6: nCg mutational motif in normal healthy cells. Contains numeric values underlying Figure 5, Supplementary Figures S6, S7.

Supplementary Table S7: UV mutational motif in normal cells. Contains numeric values underlying Figure 6.

Supplementary Table S8: APOBEC mutational motif in healthy normal tissues. Contains numeric values underlying Figure 7, Supplementary Figure S8.

Supplementary Table S9: Prevalence of aTn motif in diseased tissues. Contains numeric values underlying Figure 8, Supplementary Figure S9.

Supplementary Table S10: Prevalence of nCg mutational motif in diseased samples. Contains numeric values underlying Figure 9, Supplementary Figures S9, S10.

Supplementary Data

Supplementary Data S1: Raw output of P-MACD motif and cluster analyses to detect APOBEC mutagenesis. Contains numeric values underlying Supplementary Figure S8.

References

1. Lawrence MS, Stojanov P, Polak P*, et al.* Mutational heterogeneity in cancer and the search for new cancer-associated genes. Nature. 2013;499(7457):214-8.
2. Roberts SA, Gordenin DA. Hypermutation in human cancer genomes: footprints and mechanisms. Nat Rev Cancer. 2014;14(12):786-800.
3. Alexandrov LB, Nik-Zainal S, Wedge DC*, et al.* Signatures of mutational processes in human cancer. Nature. 2013;500(7463):415-21.
4. Ames BN, Durston WE, Yamasaki E, Lee FD. Carcinogens are mutagens: a simple test system combining liver homogenates for activation and bacteria for detection. Proceedings of the National Academy of Sciences of the United States of America. 1973;70(8):2281-5.
5. Loeb LA, Springgate CF, Battula N. Errors in DNA replication as a basis of malignant changes. Cancer research. 1974;34(9):2311-21.
6. Erickson RP. Somatic gene mutation and human disease other than cancer. Mutation research. 2003;543(2):125-36.
7. Erickson RP. Recent advances in the study of somatic mosaicism and diseases other than cancer. Curr Opin Genet Dev. 2014;26:73-8.
8. Erickson RP. The importance of de novo mutations for pediatric neurological disease--It is not all in utero or birth trauma. Mutation research Reviews in mutation research. 2016;767:42-58.
9. Saini N, Gordenin DA. Somatic mutation load and spectra: A record of DNA damage and repair in healthy human cells. Environ Mol Mutagen. 2018;59(8):672-86.
10. Martincorena I, Campbell PJ. Somatic mutation in cancer and normal cells. Science. 2015;349(6255):1483-9.
11. Maslov AY, Vijg J. Somatic mutation burden in relation to aging and functional life span: implications for cellular reprogramming and rejuvenation. Curr Opin Genet Dev. 2023;83:102132.
12. Zhang L, Lee M, Maslov AY, Montagna C, Vijg J, Dong X. Analyzing somatic mutations by single-cell whole-genome sequencing. Nature protocols. 2024;19(2):487-516.
13. Evrony GD, Hinch AG, Luo C. Applications of Single-Cell DNA Sequencing. Annu Rev Genomics Hum Genet. 2021;22:171-97.
14. Shea A, Sun S, Kennedy J, Zhang L, Vijg J, Dong X. SomaMutDB 2.0: A comprehensive database for exploring somatic mutations and their functional impact in normal human tissues. Nucleic Acids Res. 2026;54(D1):D1291-d300.
15. Sun S, Wang Y, Maslov AY, Dong X, Vijg J. SomaMutDB: a database of somatic mutations in normal human tissues. Nucleic Acids Res. 2022;50(D1):D1100-d8.
16. Yaacov A, Rosenberg S, Simon I. Mutational signatures association with replication timing in normal cells reveals similarities and differences with matched cancer tissues. Scientific reports. 2023;13(1):7833.
17. Moore L, Cagan A, Coorens THH*, et al.* The mutational landscape of human somatic and germline cells. Nature. 2021;597(7876):381-6.
18. Alexandrov LB, Kim J, Haradhvala NJ*, et al.* The repertoire of mutational signatures in human cancer. Nature. 2020;578(7793):94-101.
19. Alexandrov LB, Nik-Zainal S, Wedge DC, Campbell PJ, Stratton MR. Deciphering signatures of mutational processes operative in human cancer. Cell reports. 2013;3(1):246-59.
20. Zhang T, Joubert P, Ansari-Pour N*, et al.* Genomic and evolutionary classification of lung cancer in never smokers. Nat Genet. 2021;53(9):1348-59.
21. Sui Y, Qi L, Zhang K*, et al.* Analysis of APOBEC-induced mutations in yeast strains with low levels of replicative DNA polymerases. Proceedings of the National Academy of Sciences of the United States of America. 2020;117(17):9440-50.
22. Gerhauser C, Favero F, Risch T*, et al.* Molecular Evolution of Early-Onset Prostate Cancer Identifies Molecular Risk Markers and Clinical Trajectories. Cancer Cell. 2018;34(6):996-1011 e8.

23. Ponomarev GV, Fatykhov B, Nazarov VA*, et al.* APOBEC mutagenesis is low in most types of non-B DNA structures. iScience. 2022;25(7):104535.
24. Kazanov MD, Roberts SA, Polak P*, et al.* APOBEC-Induced Cancer Mutations Are Uniquely Enriched in Early-Replicating, Gene-Dense, and Active Chromatin Regions. Cell reports. 2015;13(6):1103-9.
25. Henderson S, Chakravarthy A, Su X, Boshoff C, Fenton TR. APOBEC-mediated cytosine deamination links PIK3CA helical domain mutations to human papillomavirus-driven tumor development. Cell reports. 2014;7(6):1833-41.
26. Middlebrooks CD, Banday AR, Matsuda K*, et al.* Association of germline variants in the APOBEC3 region with cancer risk and enrichment with APOBEC-signature mutations in tumors. Nat Genet. 2016;48(11):1330-8.
27. de Bruin EC, McGranahan N, Mitter R*, et al.* Spatial and temporal diversity in genomic instability processes defines lung cancer evolution. Science. 2014;346(6206):251-6.
28. Zhang J, Fujimoto J, Zhang J*, et al.* Intratumor heterogeneity in localized lung adenocarcinomas delineated by multiregion sequencing. Science. 2014;346(6206):256-9.
29. Cortes-Ciriano I, Lee JJ, Xi R*, et al.* Comprehensive analysis of chromothripsis in 2,658 human cancers using whole-genome sequencing. Nat Genet. 2020;52(3):331-41.
30. Robertson AG, Kim J, Al-Ahmadie H*, et al.* Comprehensive Molecular Characterization of Muscle-Invasive Bladder Cancer. Cell. 2017;171(3):540-56 e25.
31. Hurst CD, Alder O, Platt FM*, et al.* Genomic Subtypes of Non-invasive Bladder Cancer with Distinct Metabolic Profile and Female Gender Bias in KDM6A Mutation Frequency. Cancer Cell. 2017;32(5):701-15 e7.
32. Consortium ITP-CAoWG. Pan-cancer analysis of whole genomes. Nature. 2020;578(7793):82-93.
33. Davis CF, Ricketts CJ, Wang M*, et al.* The somatic genomic landscape of chromophobe renal cell carcinoma. Cancer Cell. 2014;26(3):319-30.
34. Akdemir KC, Le VT, Kim JM*, et al.* Somatic mutation distributions in cancer genomes vary with three-dimensional chromatin structure. Nat Genet. 2020;52(11):1178-88.
35. Cancer Genome Atlas Research N, Albert Einstein College of M, Analytical Biological S*, et al.* Integrated genomic and molecular characterization of cervical cancer. Nature. 2017;543(7645):378-84.
36. Chan K, Roberts SA, Klimczak LJ*, et al.* An APOBEC3A hypermutation signature is distinguishable from the signature of background mutagenesis by APOBEC3B in human cancers. Nat Genet. 2015;47(9):1067-72.
37. Petljak M, Alexandrov LB, Brammeld JS*, et al.* Characterizing Mutational Signatures in Human Cancer Cell Lines Reveals Episodic APOBEC Mutagenesis. Cell. 2019;176(6):1282-94 e20.
38. Petljak M, Dananberg A, Chu K*, et al.* Mechanisms of APOBEC3 mutagenesis in human cancer cells. Nature. 2022;607(7920):799-807.
39. Zhang T, Sang J, Hoang PH*, et al.* APOBEC affects tumor evolution and age at onset of lung cancer in smokers. Nature communications. 2025;16(1):4711.
40. Saini N, Giacobone CK, Klimczak LJ*, et al.* UV-exposure, endogenous DNA damage, and DNA replication errors shape the spectra of genome changes in human skin. PLoS Genet. 2021;17(1):e1009302.
41. Hudson KM, Klimczak LJ, Sterling JF*, et al.* Glycidamide-induced hypermutation in yeast single-stranded DNA reveals a ubiquitous clock-like mutational motif in humans. Nucleic Acids Res. 2023;51(17):9075-100.
42. Lodato MA, Rodin RE, Bohrson CL*, et al.* Aging and neurodegeneration are associated with increased mutations in single human neurons. Science. 2017.
43. Miller MB, Huang AY, Kim J*, et al.* Somatic genomic changes in single Alzheimer's disease neurons. Nature. 2022.

44. Lodato MA, Woodworth MB, Lee S*, et al.* Somatic mutation in single human neurons tracks developmental and transcriptional history. Science. 2015;350(6256):94-8.
45. Lee-Six H, Olafsson S, Ellis P*, et al.* The landscape of somatic mutation in normal colorectal epithelial cells. Nature. 2019;574(7779):532-7.
46. Ganz J, Luquette LJ, Bizzotto S*, et al.* Contrasting somatic mutation patterns in aging human neurons and oligodendrocytes. Cell. 2024;187(8):1955-70.e23.
47. Saini N, Roberts SA, Klimczak LJ*, et al.* The Impact of Environmental and Endogenous Damage on Somatic Mutation Load in Human Skin Fibroblasts. PLoS Genet. 2016;12(10):e1006385.
48. Blokzijl F, Janssen R, van Boxtel R, Cuppen E. MutationalPatterns: comprehensive genome-wide analysis of mutational processes. Genome Medicine. 2018;10(1):33.
49. Wang Y, Robinson PS, Coorens THH*, et al.* APOBEC mutagenesis is a common process in normal human small intestine. Nat Genet. 2023.
50. Li R, Du Y, Chen Z*, et al.* Macroscopic somatic clonal expansion in morphologically normal human urothelium. 2020;370(6512):82-9.
51. Roberts SA, Lawrence MS, Klimczak LJ*, et al.* An APOBEC cytidine deaminase mutagenesis pattern is widespread in human cancers. Nat Genet. 2013;45(9):970-6.
52. Wickham H. Data analysis. ggplot2: elegant graphics for data analysis: Springer; 2016. p. 189-201.
53. Hoppe J. Adobe Illustrator CC : a complete course and compendium of features. 1st edition ed. San Rafael, CA: Rocky Nook, Inc.; 2020.
54. You Y-H, Lee D-H, Yoon J-H, Nakajima S, Yasui A, Pfeifer GP. Cyclobutane Pyrimidine Dimers Are Responsible for the Vast Majority of Mutations Induced by UVB Irradiation in Mammalian Cells*. J Biol Chem. 2001;276(48):44688-94.
55. Pfeifer GP. Mutagenesis at methylated CpG sequences. Curr Top Microbiol Immunol. 2006;301:259-81.
56. Degtyareva NP, Placentra VC, Gabel SA*, et al.* Changes in metabolic landscapes shape divergent but distinct mutational signatures and cytotoxic consequences of redox stress. Nucleic Acids Res. 2023;51(10):5056-72.
57. Saini N, Sterling JF, Sakofsky CJ*, et al.* Mutation signatures specific to DNA alkylating agents in yeast and cancers. Nucleic Acids Res. 2020;48(7):3692-707.
58. Vijayraghavan S, Porcher L, Mieczkowski PA, Saini N. Acetaldehyde makes a distinct mutation signature in single-stranded DNA. Nucleic Acids Res. 2022.
59. Rosenquist TA, Grollman AP. Mutational signature of aristolochic acid: Clue to the recognition of a global disease. DNA Repair (Amst). 2016;44:205-11.
60. Li R, Di L, Li J*, et al.* A body map of somatic mutagenesis in morphologically normal human tissues. Nature. 2021;597(7876):398-403.
61. Olafsson S, McIntyre RE, Coorens T*, et al.* Somatic Evolution in Non-neoplastic IBD-Affected Colon. Cell. 2020;182(3):672-84.e11.
62. Roberts SA, Sterling J, Thompson C*, et al.* Clustered mutations in yeast and in human cancers can arise from damaged long single-strand DNA regions. Mol Cell. 2012;46(4):424-35.
63. Mertz TM, Collins CD, Dennis M, Coxon M, Roberts SA. APOBEC-Induced Mutagenesis in Cancer. Annu Rev Genet. 2022.
64. Peng W, Shaw BR. Accelerated deamination of cytosine residues in UV-induced cyclobutane pyrimidine dimers leads to CC-->TT transitions. Biochemistry. 1996;35(31):10172-81.
65. Nik-Zainal S, Alexandrov LB, Wedge DC*, et al.* Mutational processes molding the genomes of 21 breast cancers. Cell. 2012;149(5):979-93.
66. Saini N, Gordenin DA. Hypermutation in single-stranded DNA. DNA Repair (Amst). 2020;91-92:102868.

67. Dennen MS, Kockler ZW, Roberts SA, Burkholder AB, Klimczak LJ, Gordenin DA. Hypomorphic mutation in the large subunit of replication protein A affects mutagenesis by human APOBEC cytidine deaminases in yeast. G3 Genes|Genomes|Genetics. 2024;14(10):jkae196.
68. Sakofsky CJ, Saini N, Klimczak LJ*, et al.* Repair of multiple simultaneous double-strand breaks causes bursts of genome-wide clustered hypermutation. PLoS biology. 2019;17(9):e3000464.
69. Chan K, Gordenin DA. Clusters of Multiple Mutations: Incidence and Molecular Mechanisms. Annu Rev Genet. 2015;49:243-67.
70. Abascal F, Harvey LMR, Mitchell E*, et al.* Somatic mutation landscapes at single-molecule resolution. Nature. 2021;593(7859):405-10.
71. Brunner SF, Roberts ND, Wylie LA*, et al.* Somatic mutations and clonal dynamics in healthy and cirrhotic human liver. Nature. 2019;574(7779):538-42.
72. Yoshida K, Gowers KHC, Lee-Six H*, et al.* Tobacco smoking and somatic mutations in human bronchial epithelium. Nature. 2020.
73. Nishimura T, Kakiuchi N, Yoshida K*, et al.* Evolutionary histories of breast cancer and related clones. Nature. 2023;620(7974):607-14.
74. Chevalier A, Guo T, Gurevich NQ, Xu J, Yajima M, Campbell JD. Characterization of Mutational Signatures in Tumors from a Large Chinese Population. Cancer Research Communications. 2025;5(8):1466-76.
75. Díaz-Gay M, Zhang T, Hoang PH*, et al.* The mutagenic forces shaping the genomes of lung cancer in never smokers. Nature. 2025;644(8075):133-44.
76. Zanger UM, Schwab M. Cytochrome P450 enzymes in drug metabolism: regulation of gene expression, enzyme activities, and impact of genetic variation. Pharmacology & therapeutics. 2013;138(1):103-41.
77. Chen C, Wang DW. Chapter Seven - Cytochrome P450-CYP2 Family-Epoxygenase Role in Inflammation and Cancer. In: Hardwick JP, editor. Advances in Pharmacology: Academic Press; 2015. p. 193-221.
78. Kay J, Thadhani E, Samson L, Engelward B. Inflammation-induced DNA damage, mutations and cancer. DNA Repair. 2019;83:102673.
79. Cao H, Jiang Y, Wang Y. Kinetics of deamination and Cu(II)/H 2 O 2 /Ascorbate-induced formation of 5-methylcytosine glycol at CpG sites in duplex DNA. Nucleic Acids Research. 2009;37(19):6635-43.
80. Lehmann J, Seebode C, Martens MC, Emmert S. Xeroderma Pigmentosum - Facts and Perspectives. Anticancer Res. 2018;38(2):1159-64.
81. Chen J, Furano AV. Breaking bad: The mutagenic effect of DNA repair. DNA Repair. 2015;32(0):43-51.
82. Hodgson SV, Foulkes WD, Maher ER, Turnbull C. Inherited Susceptibility to Cancer: Past, Present and Future. Annals of Human Genetics. 2025;89(5):354-65.
83. Robinson PS, Thomas LE, Abascal F*, et al.* Inherited MUTYH mutations cause elevated somatic mutation rates and distinctive mutational signatures in normal human cells. Nature Communications. 2022;13(1):3949.
84. Robinson PS, Coorens THH, Palles C*, et al.* Increased somatic mutation burdens in normal human cells due to defective DNA polymerases. Nature Genetics. 2021;53(10):1434-42.
85. Flynn A, Waszak SM, Weischenfeldt J. Somatic CpG hypermutation is associated with mismatch repair deficiency in cancer. Molecular systems biology. 2024;20(9):1006-24-24.
86. Palles C, West HD, Chew E*, et al.* Germline MBD4 deficiency causes a multi-tumor predisposition syndrome. Am J Hum Genet. 2022;109(5):953-60.
87. Querido I, Pinto C, Arinto P*, et al.* A Novel Deleterious Variant and a Founder Effect in Four New Families of MBD4-Associated Neoplasia Syndrome Recruited Over a Period of 20 Years. Clinical genetics. 2025.

88. Nik-Zainal S, Wedge DC, Alexandrov LB*, et al.* Association of a germline copy number polymorphism of APOBEC3A and APOBEC3B with burden of putative APOBEC-dependent mutations in breast cancer. Nat Genet. 2014;46(5):487-91.
89. Gansmo LB, Romundstad P, Hveem K*, et al.* APOBEC3A/B deletion polymorphism and cancer risk. Carcinogenesis. 2018;39(2):118-24.

Figure 1

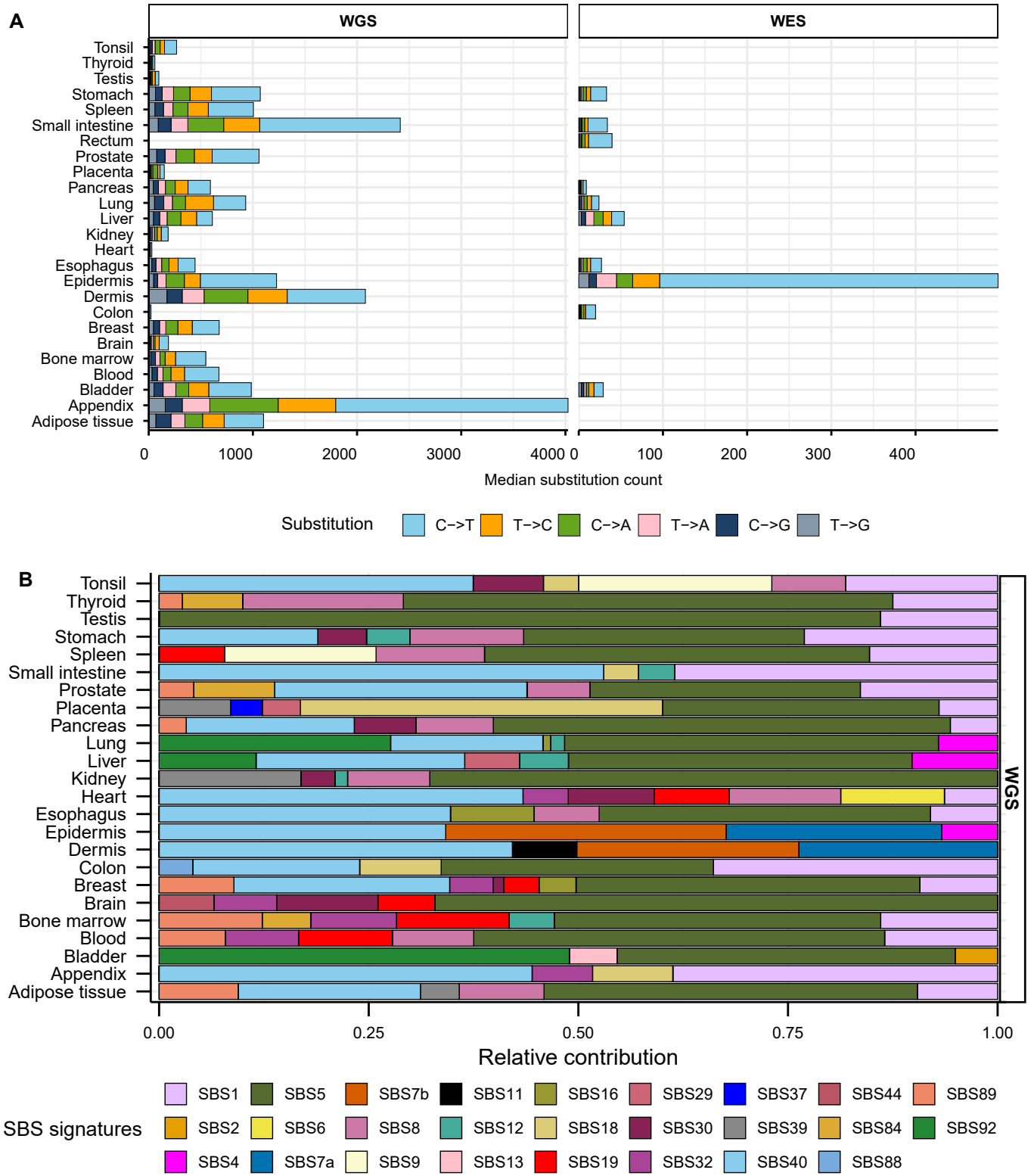
A
WGS
WES
Tonsil
Thyroid
Testis
Stomach
Spleen
Small intestine
Rectum
Prostate
Placenta
Pancreas
Lung
Liver
Kidney
Heart
Esophagus
Epidermis
Dermis
Colon
Breast
Brain
Bone marrow
Blood
Bladder
Appendix
Adipose tissue
0
1000
2000
3000
4000
0
100
200
300
400
Median substitution count
Substitution
C->T
T->C
C->A
T->A
C->G
T->G
B
WGS
0.00
0.25
0.50
0.75
1.00
Relative contribution
SBS signatures
SBS1
SBS5
SBS7b
SBS11
SBS16
SBS29
SBS37
SBS44
SBS89
SBS2
SBS6
SBS8
SBS12
SBS18
SBS30
SBS39
SBS84
SBS92
SBS4
SBS7a
SBS9
SBS13
SBS19
SBS32
SBS40
SBS88

Figure 2

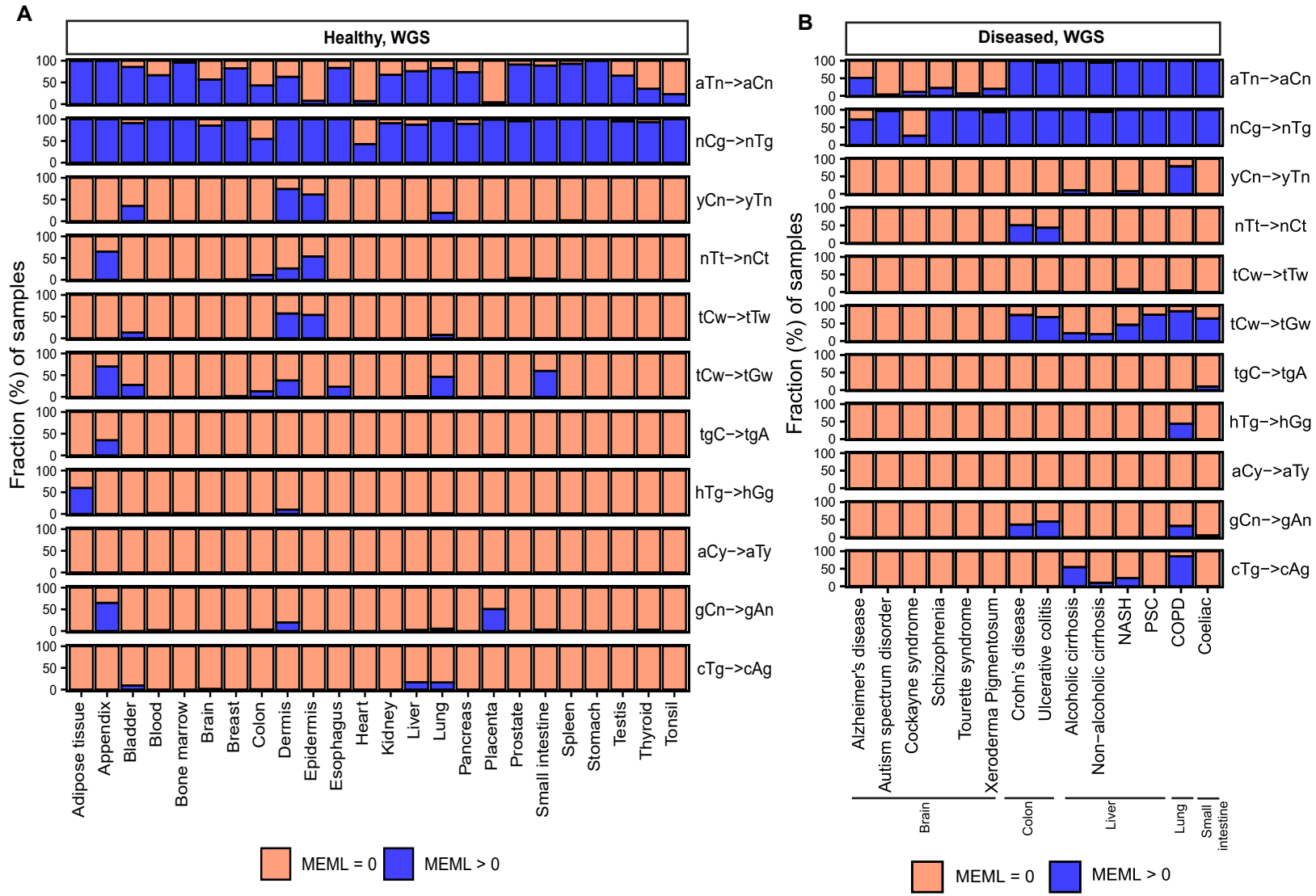
A
Healthy, WGS
Fraction (%) of samples
100
50
0
aTn->aCn
nCg->nTg
yCn->yTn
nTt->nCt
tCw->tTw
tCw->tGw
tgC->tgA
hTg->hGg
aCy->aTy
gCn->gAn
cTg->cAg
Adipose tissue
Appendix
Bladder
Blood
Bone marrow
Brain
Breast
Colon
Dermis
Epidermis
Esophagus
Heart
Kidney
Liver
Lung
Pancreas
Placenta
Prostate
Small intestine
Spleen
Stomach
Testis
Thyroid
Tonsil
MEML = 0
MEML > 0
B
Diseased, WGS
Fraction (%) of samples
Alzheimer's disease
Autism spectrum disorder
Cockayne syndrome
Schizophrenia
Tourette syndrome
Xeroderma Pigmentosum
Crohn's disease
Ulcerative colitis
Alcoholic cirrhosis
Non-alcoholic cirrhosis
NASH
PSC
COPD
Coeliac
Brain
Colon
Liver
Lung
Small intestine
MEML = 0
MEML > 0

Figure 3

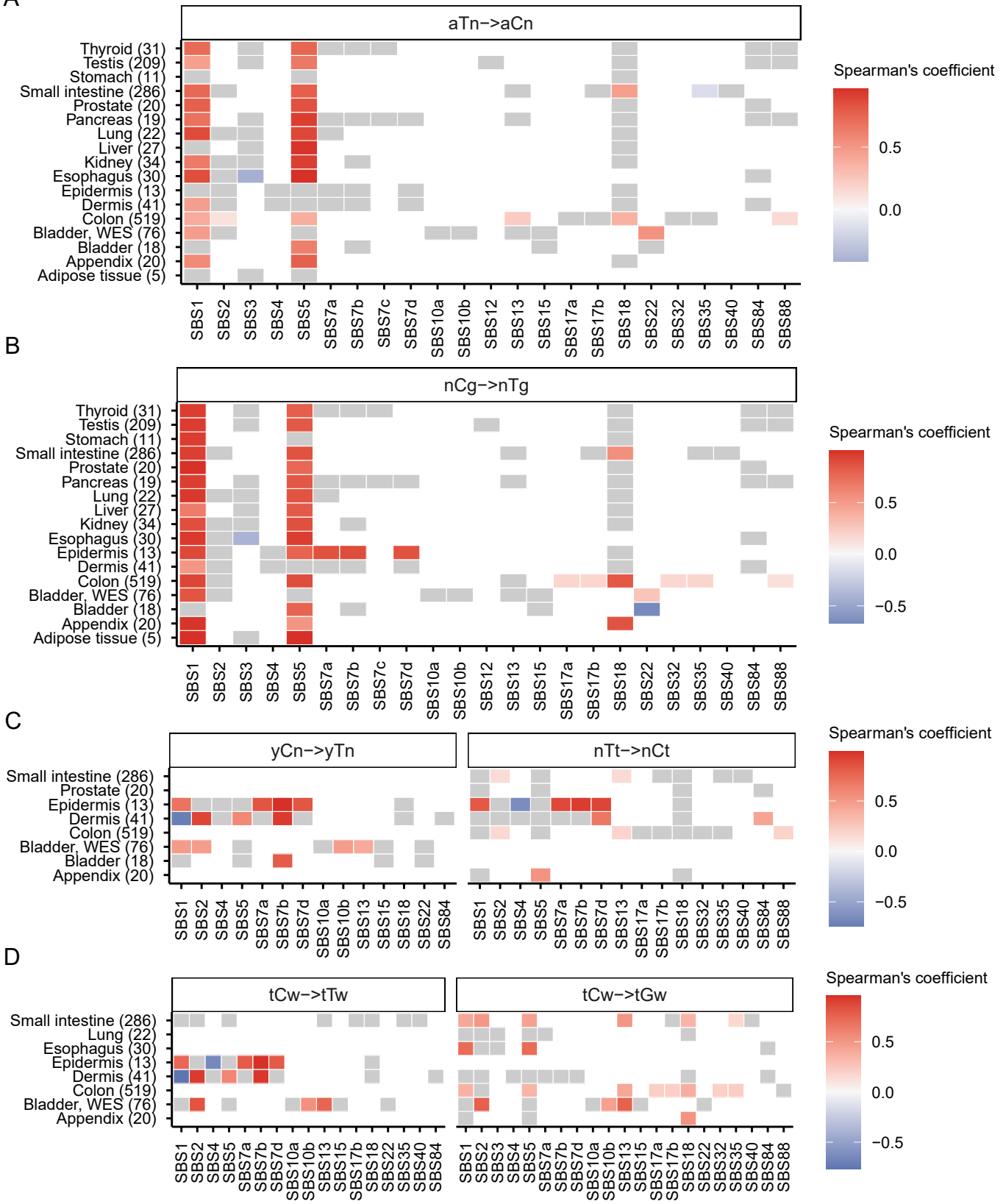
A
aTn->aCn
Thyroid (31)
Testis (209)
Stomach (11)
Small intestine (286)
Prostate (20)
Pancreas (19)
Lung (22)
Liver (27)
Kidney (34)
Esophagus (30)
Epidermis (13)
Dermis (41)
Colon (519)
Bladder, WES (76)
Bladder (18)
Appendix (20)
Adipose tissue (5)
SBS1 SBS2 SBS3 SBS4 SBS5 SBS7a SBS7b SBS7c SBS7d SBS10a SBS10b SBS12 SBS13 SBS15 SBS17a SBS17b SBS18 SBS22 SBS32 SBS35 SBS40 SBS84 SBS88
Spearman's coefficient
0.5
0.0
B
nCg->nTg
Thyroid (31)
Testis (209)
Stomach (11)
Small intestine (286)
Prostate (20)
Pancreas (19)
Lung (22)
Liver (27)
Kidney (34)
Esophagus (30)
Epidermis (13)
Dermis (41)
Colon (519)
Bladder, WES (76)
Bladder (18)
Appendix (20)
Adipose tissue (5)
SBS1 SBS2 SBS3 SBS4 SBS5 SBS7a SBS7b SBS7c SBS7d SBS10a SBS10b SBS12 SBS13 SBS15 SBS17a SBS17b SBS18 SBS22 SBS32 SBS35 SBS40 SBS84 SBS88
Spearman's coefficient
0.5
0.0
−0.5
C
yCn->yTn
nTt->nCt
Small intestine (286)
Prostate (20)
Epidermis (13)
Dermis (41)
Colon (519)
Bladder, WES (76)
Bladder (18)
Appendix (20)
SBS1 SBS2 SBS4 SBS5 SBS7a SBS7b SBS7d SBS10a SBS10b SBS13 SBS15 SBS18 SBS22 SBS84
SBS1 SBS2 SBS4 SBS5 SBS7a SBS7b SBS7d SBS13 SBS17a SBS17b SBS18 SBS32 SBS35 SBS40 SBS84 SBS88
Spearman's coefficient
0.5
0.0
−0.5
D
tCw->tTw
tCw->tGw
Small intestine (286)
Lung (22)
Esophagus (30)
Epidermis (13)
Dermis (41)
Colon (519)
Bladder, WES (76)
Appendix (20)
SBS1 SBS2 SBS4 SBS5 SBS7a SBS7b SBS7d SBS10a SBS10b SBS13 SBS15 SBS17b SBS18 SBS22 SBS35 SBS40 SBS84
SBS1 SBS2 SBS3 SBS4 SBS5 SBS7a SBS7b SBS7d SBS10a SBS10b SBS13 SBS15 SBS17a SBS17b SBS18 SBS22 SBS32 SBS35 SBS40 SBS84 SBS88
Spearman's coefficient
0.5
0.0
−0.5

Figure 4

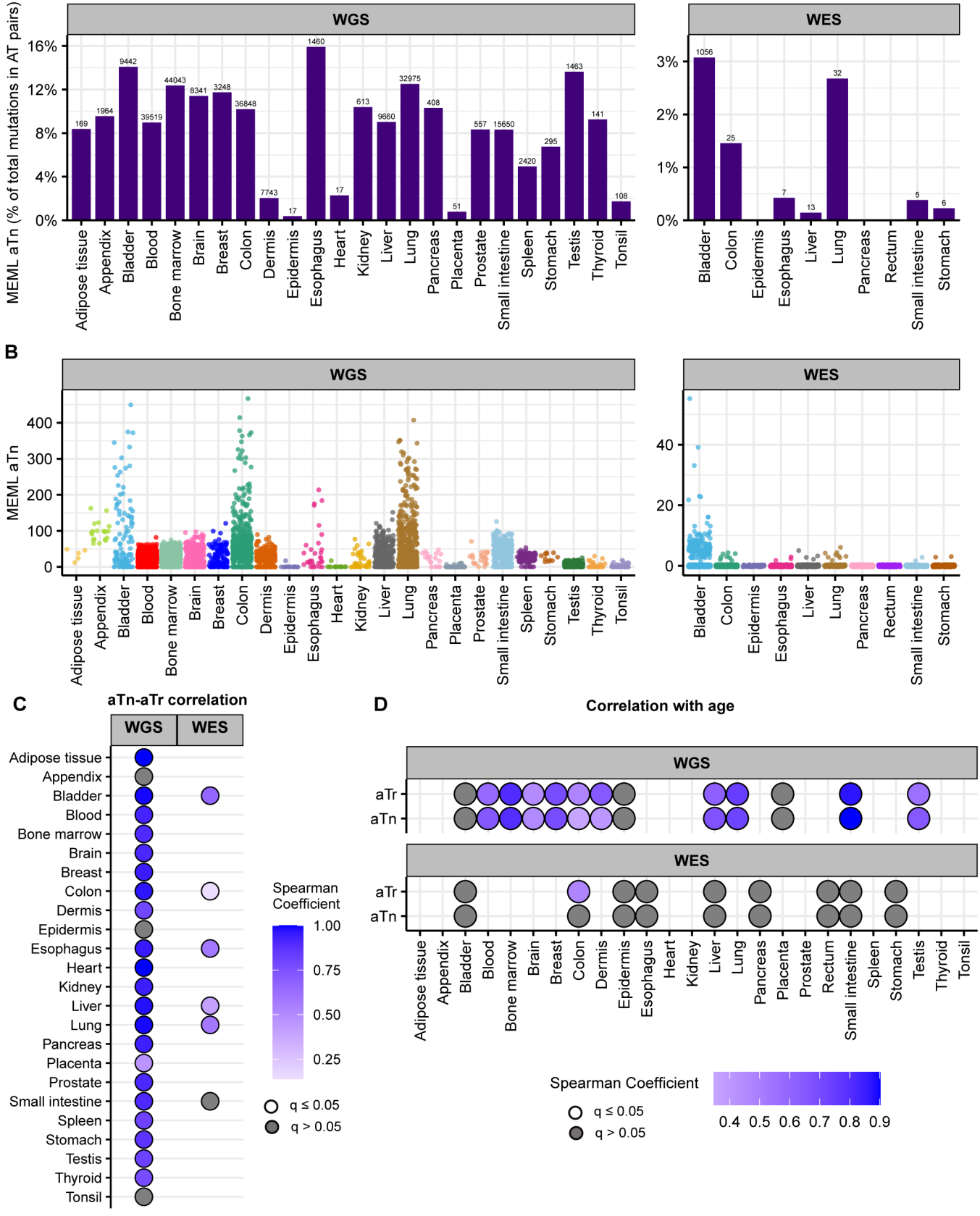
A
WGS
WES
MEML aTn (% of total mutations in AT pairs)
16%
12%
8%
4%
0%
3%
2%
1%
0%
169
1964
9442
39519
44043
8341
3248
36848
7743
17
1460
17
613
9660
32975
408
51
557
15650
2420
295
1463
141
108
1056
25
7
13
32
5
6
Adipose tissue
Appendix
Bladder
Blood
Bone marrow
Brain
Breast
Colon
Dermis
Epidermis
Esophagus
Heart
Kidney
Liver
Lung
Pancreas
Placenta
Prostate
Small intestine
Spleen
Stomach
Testis
Thyroid
Tonsil
Bladder
Colon
Epidermis
Esophagus
Liver
Lung
Pancreas
Rectum
Small intestine
Stomach
B
WGS
WES
MEML aTn
400
300
200
100
0
40
20
0
Adipose tissue
Appendix
Bladder
Blood
Bone marrow
Brain
Breast
Colon
Dermis
Epidermis
Esophagus
Heart
Kidney
Liver
Lung
Pancreas
Placenta
Prostate
Small intestine
Spleen
Stomach
Testis
Thyroid
Tonsil
Bladder
Colon
Epidermis
Esophagus
Liver
Lung
Pancreas
Rectum
Small intestine
Stomach
C
aTn-aTr correlation
WGS
WES
Adipose tissue
Appendix
Bladder
Blood
Bone marrow
Brain
Breast
Colon
Dermis
Epidermis
Esophagus
Heart
Kidney
Liver
Lung
Pancreas
Placenta
Prostate
Small intestine
Spleen
Stomach
Testis
Thyroid
Tonsil
Spearman Coefficient
1.00
0.75
0.50
0.25
q ≤ 0.05
q > 0.05
D
Correlation with age
WGS
WES
aTr
aTn
aTr
aTn
Adipose tissue
Appendix
Bladder
Blood
Bone marrow
Brain
Breast
Colon
Dermis
Epidermis
Esophagus
Heart
Kidney
Liver
Lung
Pancreas
Placenta
Prostate
Rectum
Small intestine
Spleen
Stomach
Testis
Thyroid
Tonsil
Spearman Coefficient
q ≤ 0.05
q > 0.05
0.4
0.5
0.6
0.7
0.8
0.9

Figure 5

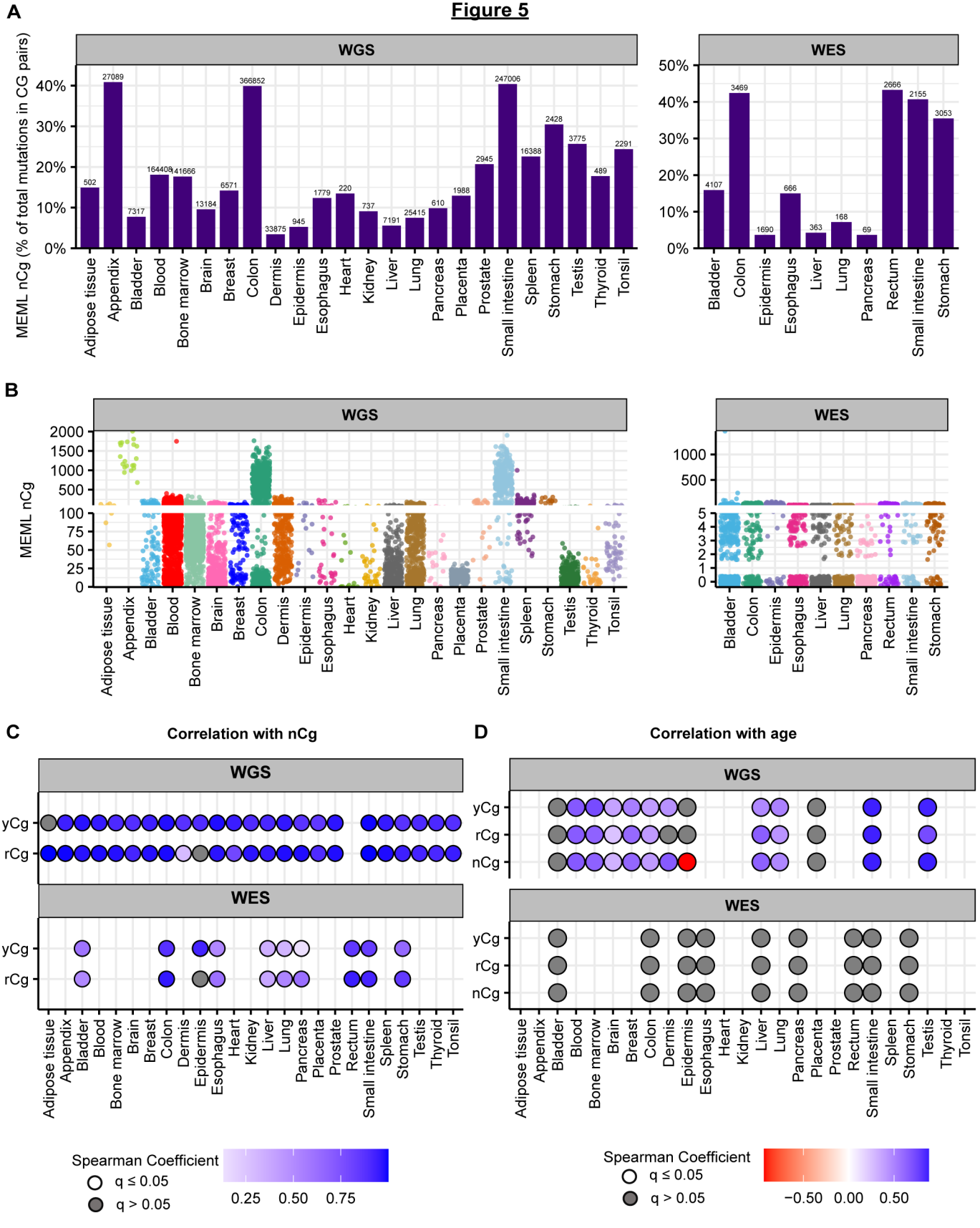
A
WGS
WES
MEML nCg (% of total mutations in CG pairs)
0%
10%
20%
30%
40%
50%
502
27089
7317
164408
141666
13184
6571
366852
33875
945
1779
220
737
7191
25415
610
1988
2945
247006
16388
2428
3775
489
2291
4107
3469
1690
666
363
168
69
2666
2155
3053
Adipose tissue
Appendix
Bladder
Blood
Bone marrow
Brain
Breast
Colon
Dermis
Epidermis
Esophagus
Heart
Kidney
Liver
Lung
Pancreas
Placenta
Prostate
Small intestine
Spleen
Stomach
Testis
Thyroid
Tonsil
Rectum
B
MEML nCg
2000
1500
1000
500
100
75
50
25
0
5
4
3
2
1
C
Correlation with nCg
D
Correlation with age
yCg
rCg
nCg
Spearman Coefficient
q ≤ 0.05
q > 0.05
0.25
0.50
0.75
−0.50
0.00
0.50

Figure 6

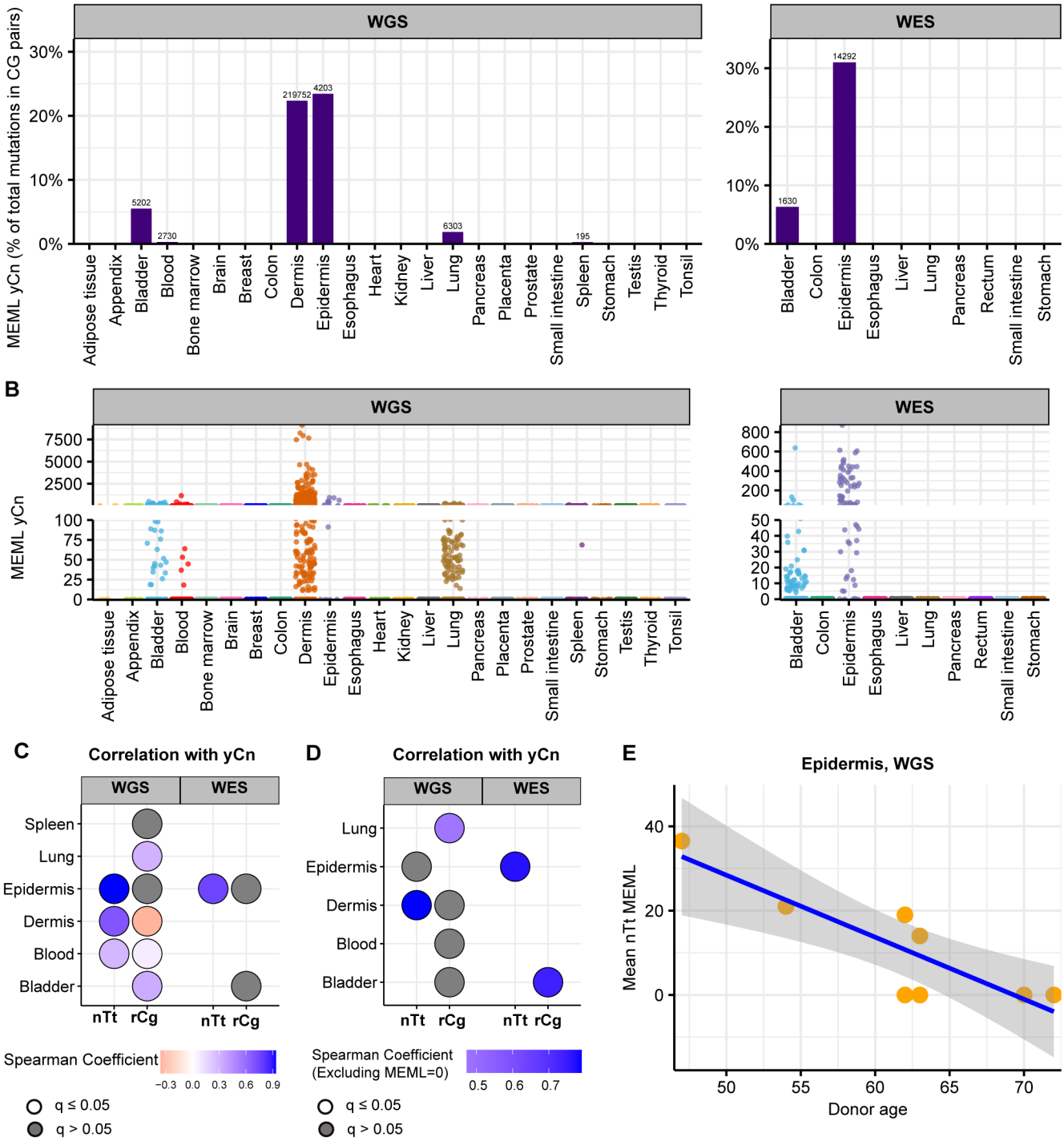
A
WGS
WES
MEML yCn (% of total mutations in CG pairs)
30%
20%
10%
0%
5202
2730
219752
4203
6303
195
1630
14292
Adipose tissue
Appendix
Bladder
Blood
Bone marrow
Brain
Breast
Colon
Dermis
Epidermis
Esophagus
Heart
Kidney
Liver
Lung
Pancreas
Placenta
Prostate
Small intestine
Spleen
Stomach
Testis
Thyroid
Tonsil
Rectum
B
MEML yCn
7500
5000
2500
100
75
50
25
0
800
600
400
200
50
40
30
20
10
C
Correlation with yCn
nTt
rCg
Spleen
Lung
Epidermis
Dermis
Blood
Bladder
Spearman Coefficient
−0.3 0.0 0.3 0.6 0.9
q ≤ 0.05
q > 0.05
D
Correlation with yCn
Spearman Coefficient
(Excluding MEML=0)
0.5 0.6 0.7
E
Epidermis, WGS
Mean nTt MEML
Donor age
50
55
60
65
70

Figure 7

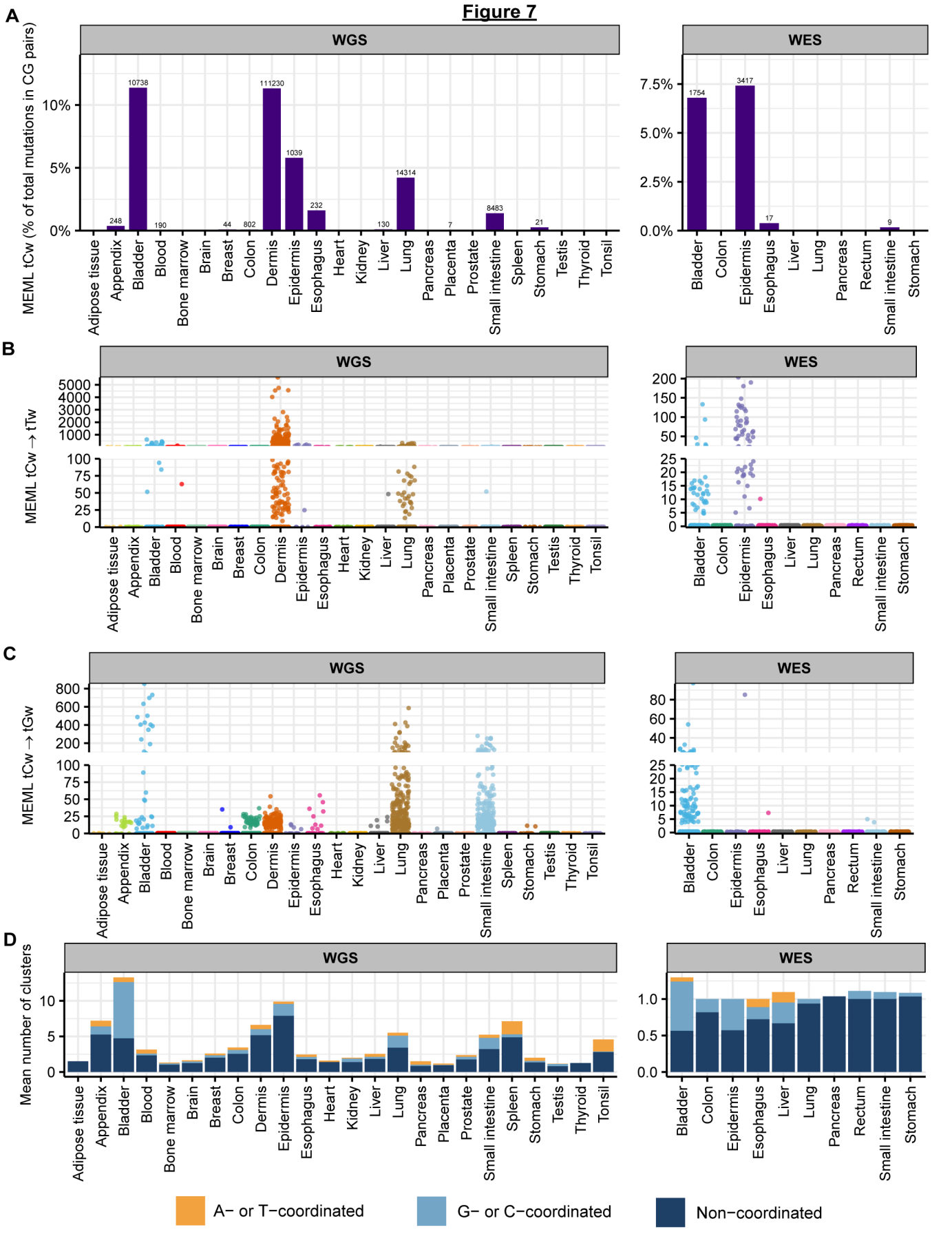
A
WGS
WES
MEML tCw (% of total mutations in CG pairs)
10%
5%
0%
7.5%
5.0%
2.5%
0.0%
248
10738
190
44
802
111230
1039
232
130
14314
7
8483
21
1754
3417
17
9
Adipose tissue
Appendix
Bladder
Blood
Bone marrow
Brain
Breast
Colon
Dermis
Epidermis
Esophagus
Heart
Kidney
Liver
Lung
Pancreas
Placenta
Prostate
Small intestine
Spleen
Stomach
Testis
Thyroid
Tonsil
Rectum
B
MEML tCw → tTw
C
MEML tCw → tGw
D
Mean number of clusters
A− or T−coordinated
G− or C−coordinated
Non−coordinated

Figure 8

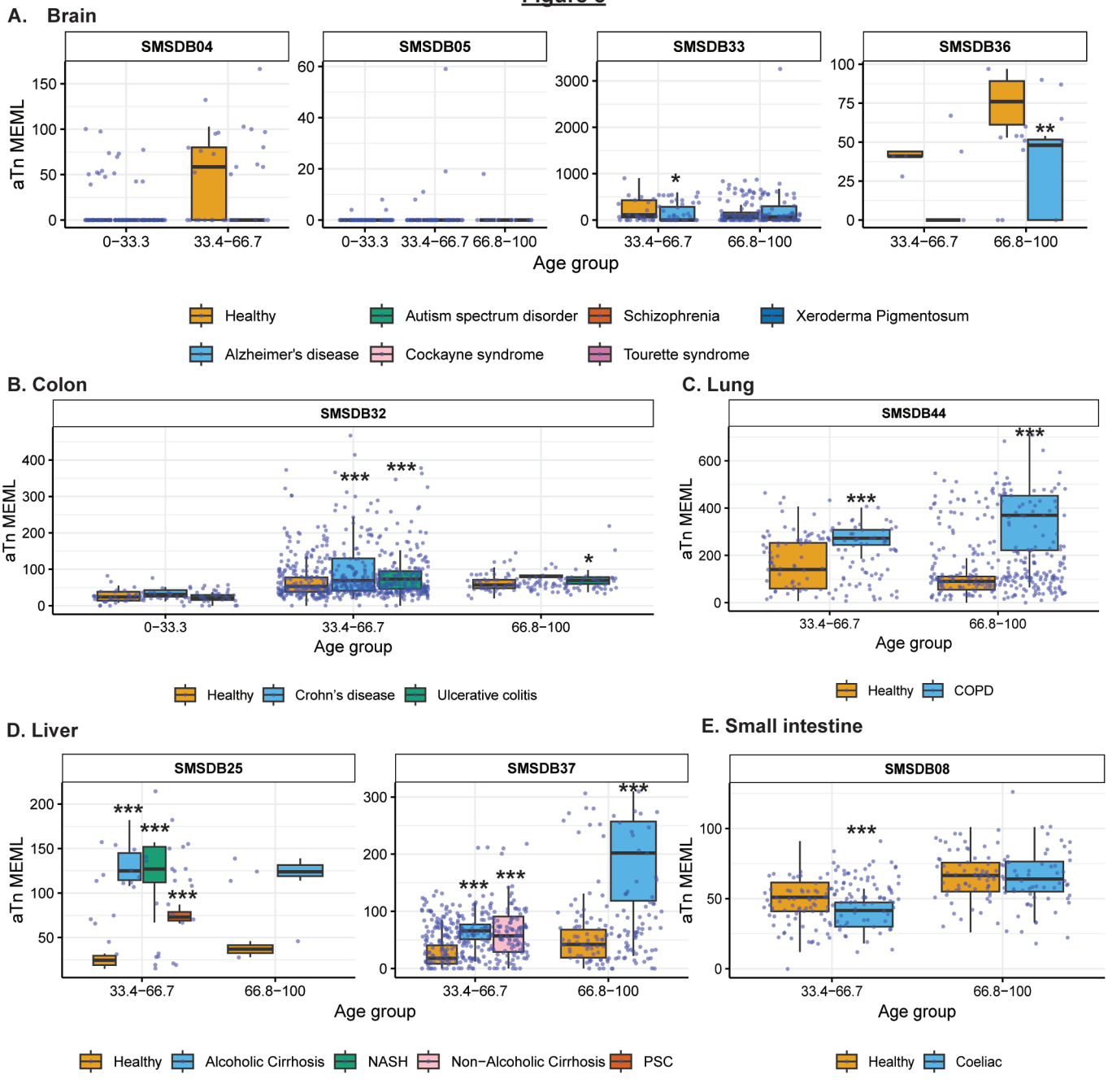
A. Brain
SMSDB04
SMSDB05
SMSDB33
SMSDB36
aTn MEML
0–33.3
33.4–66.7
66.8–100
Age group
Healthy
Autism spectrum disorder
Schizophrenia
Xeroderma Pigmentosum
Alzheimer's disease
Cockayne syndrome
Tourette syndrome
B. Colon
SMSDB32
Crohn's disease
Ulcerative colitis
C. Lung
SMSDB44
COPD
D. Liver
SMSDB25
SMSDB37
Alcoholic Cirrhosis
NASH
Non–Alcoholic Cirrhosis
PSC
E. Small intestine
SMSDB08
Coeliac

Figure 9

A. Brain

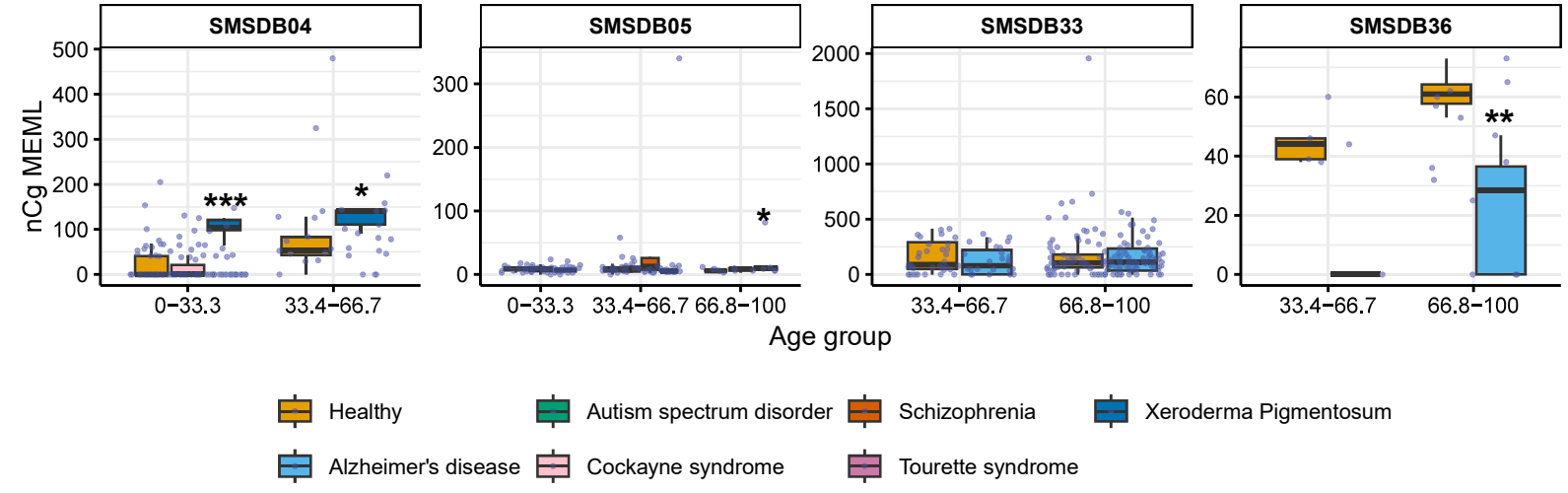

B. Colon

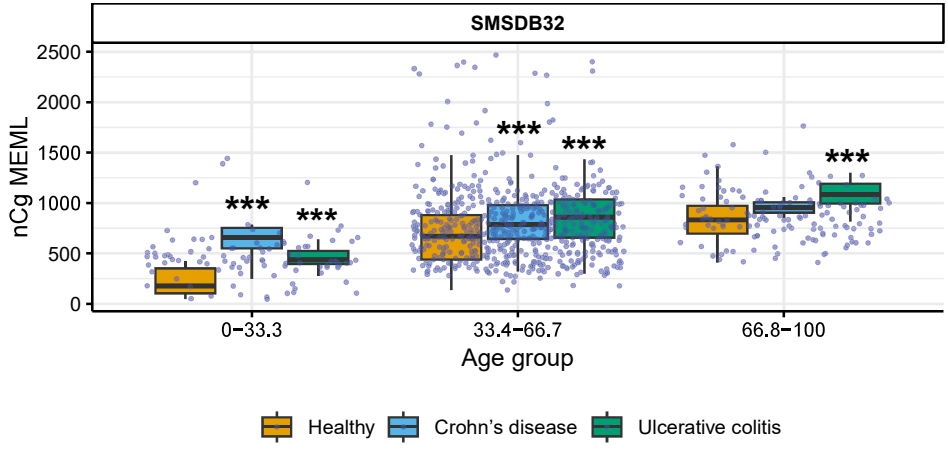

C. Lung

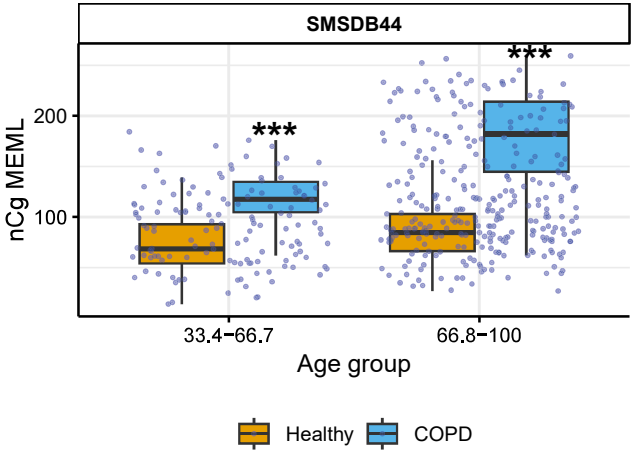

D. Liver

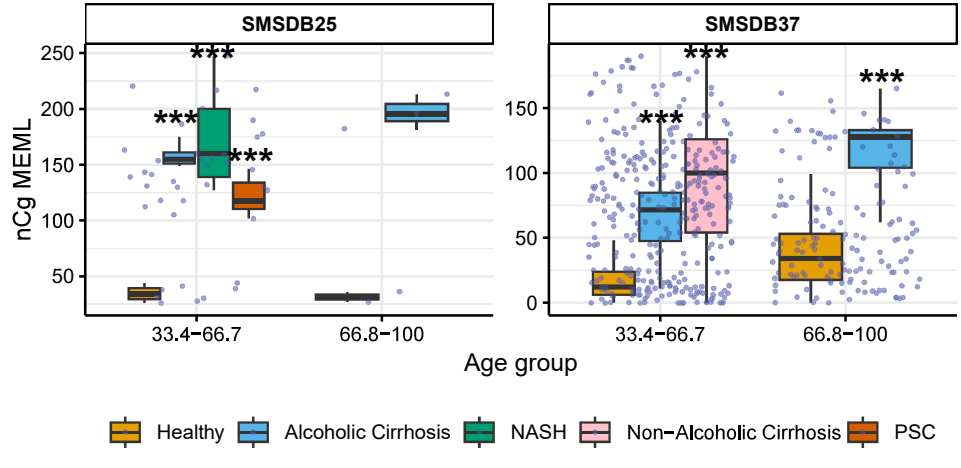

E. Small intestine

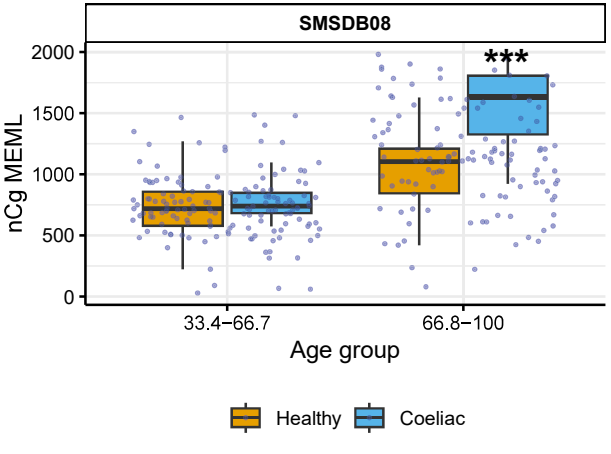

Figure 10

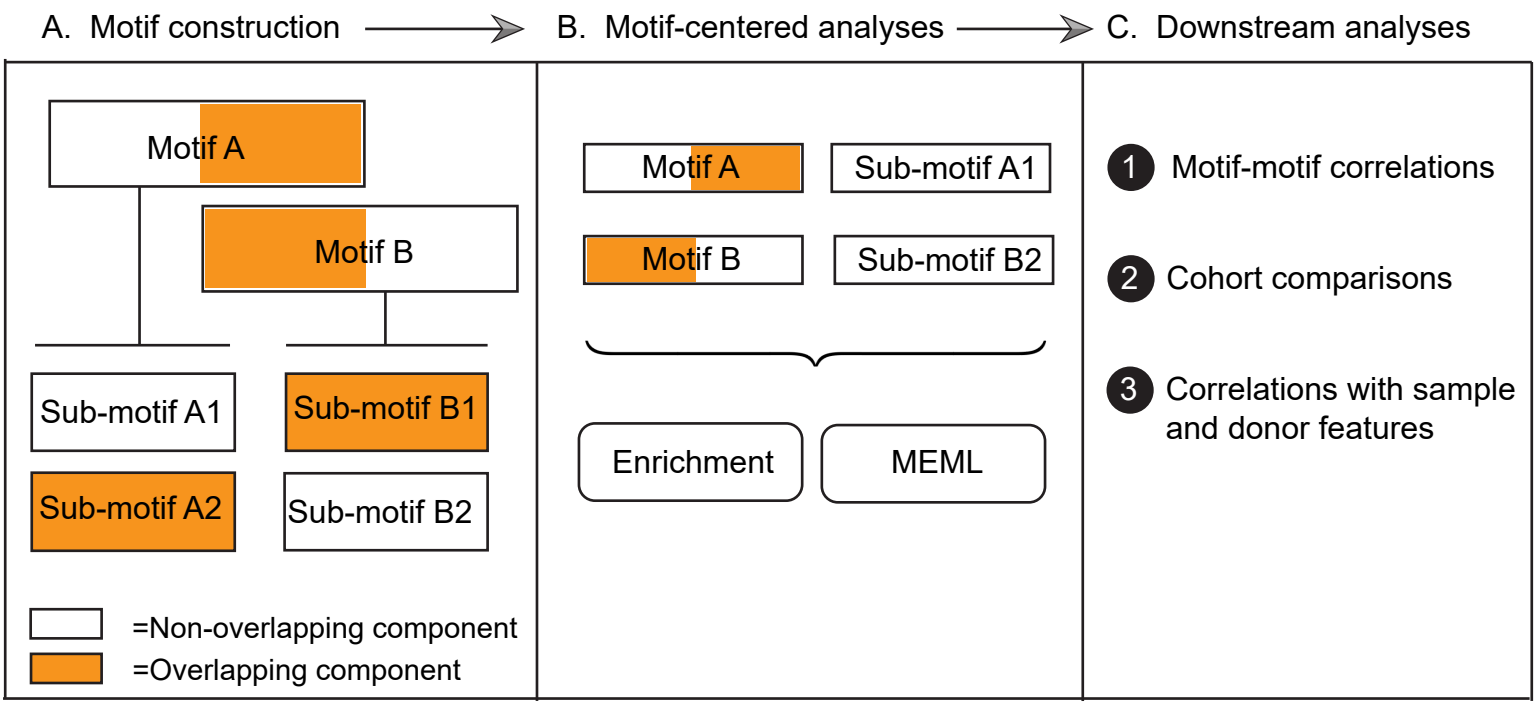
A. Motif construction
B. Motif-centered analyses
C. Downstream analyses
Motif A
Motif B
Sub-motif A1
Sub-motif B1
Sub-motif A2
Sub-motif B2
=Non-overlapping component
=Overlapping component
Motif A
Sub-motif A1
Motif B
Sub-motif B2
Enrichment
MEML
1 Motif-motif correlations
2 Cohort comparisons
3 Correlations with sample and donor features

Figure S1

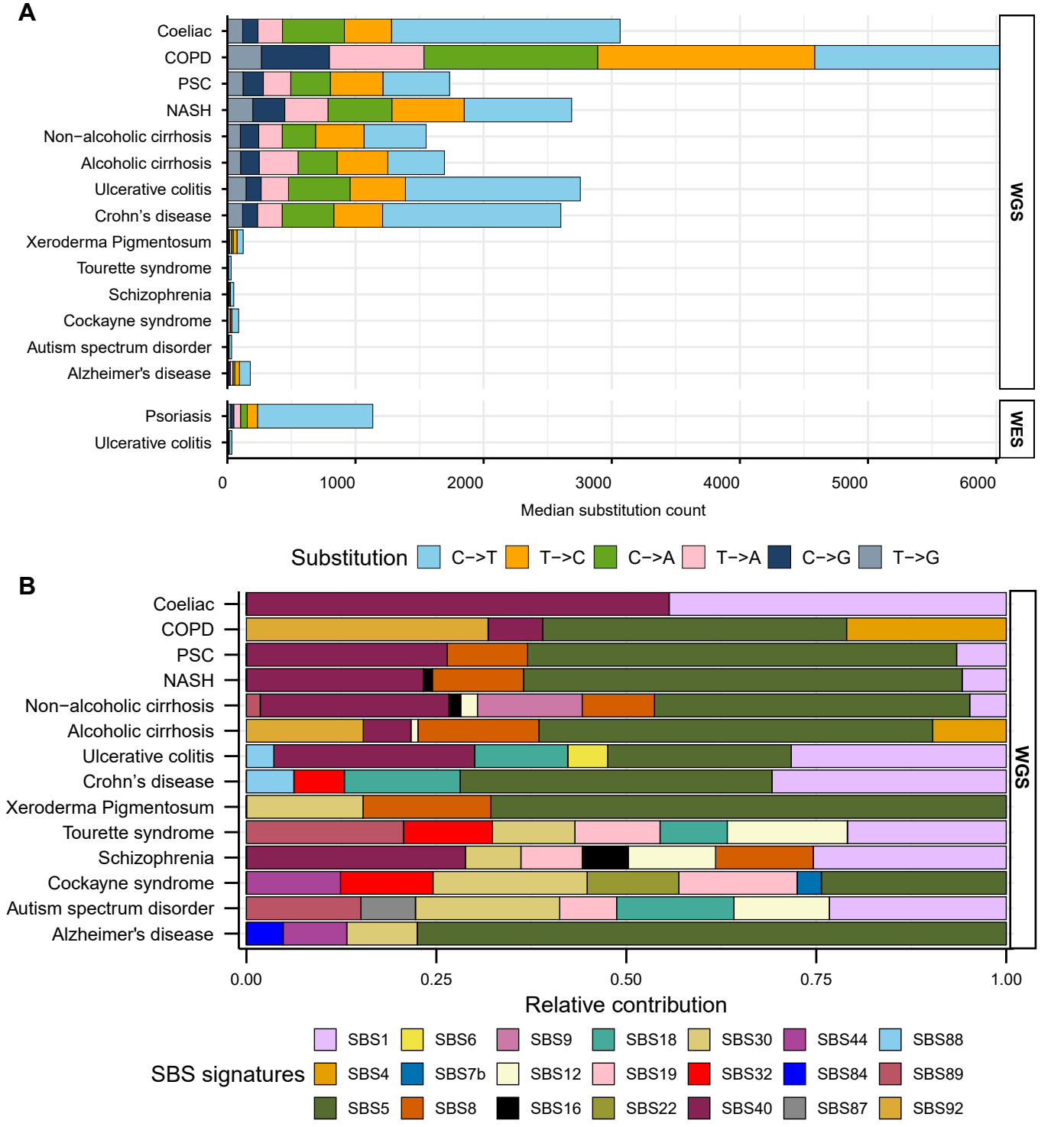
A
Coeliac
COPD
PSC
NASH
Non−alcoholic cirrhosis
Alcoholic cirrhosis
Ulcerative colitis
Crohn's disease
Xeroderma Pigmentosum
Tourette syndrome
Schizophrenia
Cockayne syndrome
Autism spectrum disorder
Alzheimer's disease
Psoriasis
Ulcerative colitis
WGS
WES
0
1000
2000
3000
4000
5000
6000
Median substitution count
Substitution
C−>T
T−>C
C−>A
T−>A
C−>G
T−>G
B
Coeliac
COPD
PSC
NASH
Non−alcoholic cirrhosis
Alcoholic cirrhosis
Ulcerative colitis
Crohn's disease
Xeroderma Pigmentosum
Tourette syndrome
Schizophrenia
Cockayne syndrome
Autism spectrum disorder
Alzheimer's disease
WGS
0.00
0.25
0.50
0.75
1.00
Relative contribution
SBS signatures
SBS1
SBS6
SBS9
SBS18
SBS30
SBS44
SBS88
SBS4
SBS7b
SBS12
SBS19
SBS32
SBS84
SBS89
SBS5
SBS8
SBS16
SBS22
SBS40
SBS87
SBS92

Figure S2

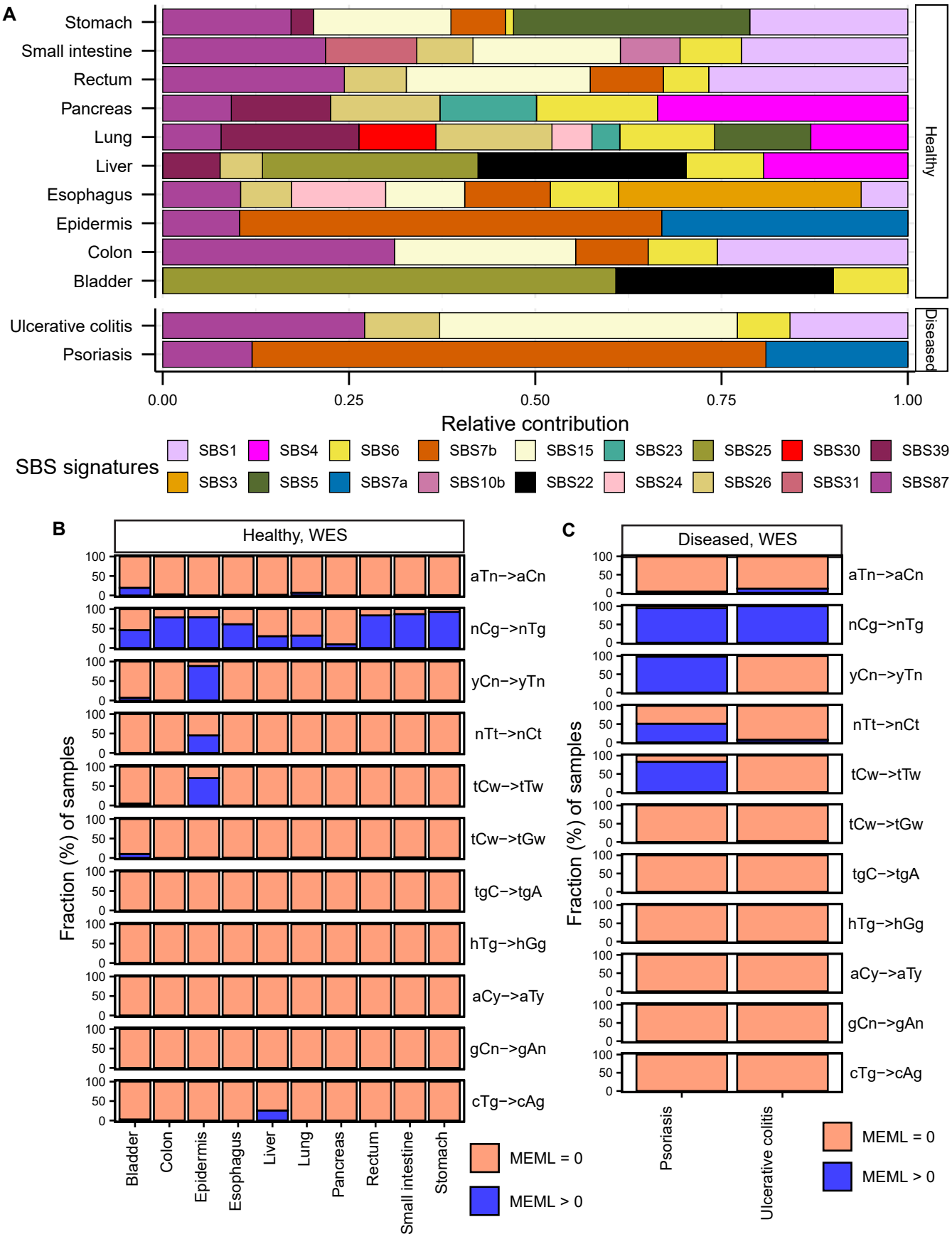
A
Stomach
Small intestine
Rectum
Pancreas
Lung
Liver
Esophagus
Epidermis
Colon
Bladder
Healthy
Ulcerative colitis
Psoriasis
Diseased
0.00
0.25
0.50
0.75
1.00
Relative contribution
SBS signatures
SBS1
SBS3
SBS4
SBS5
SBS6
SBS7a
SBS7b
SBS10b
SBS15
SBS22
SBS23
SBS24
SBS25
SBS26
SBS30
SBS31
SBS39
SBS87
B
Healthy, WES
Fraction (%) of samples
aTn->aCn
nCg->nTg
yCn->yTn
nTt->nCt
tCw->tTw
tCw->tGw
tgC->tgA
hTg->hGg
aCy->aTy
gCn->gAn
cTg->cAg
Bladder
Colon
Epidermis
Esophagus
Liver
Lung
Pancreas
Rectum
Small intestine
Stomach
MEML = 0
MEML > 0
C
Diseased, WES
Fraction (%) of samples
aTn->aCn
nCg->nTg
yCn->yTn
nTt->nCt
tCw->tTw
tCw->tGw
tgC->tgA
hTg->hGg
aCy->aTy
gCn->gAn
cTg->cAg
Psoriasis
Ulcerative colitis
MEML = 0
MEML > 0

Figure S3A

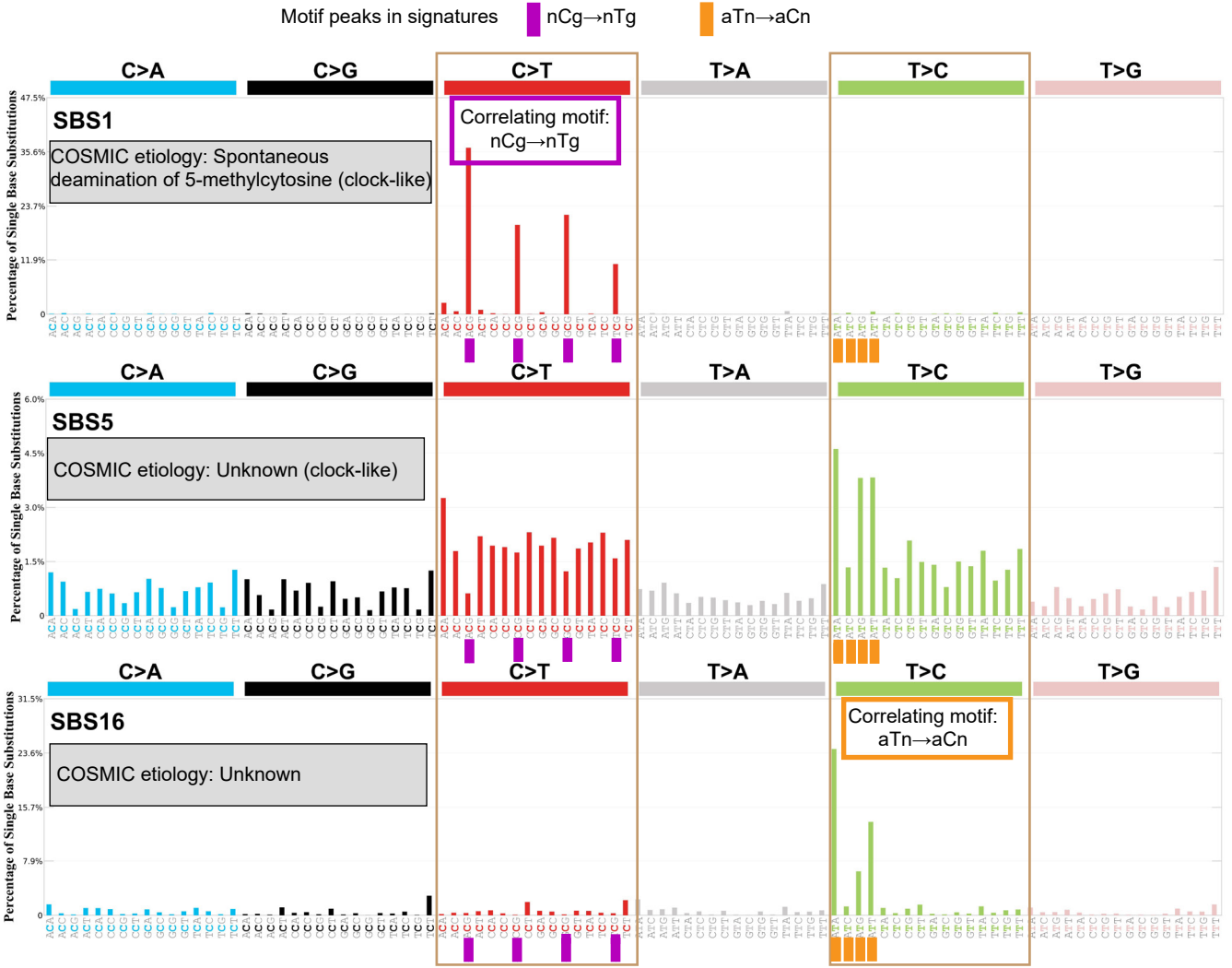
Motif peaks in signatures
nCg→nTg
aTn→aCn
C>A
C>G
C>T
T>A
T>C
T>G
SBS1
COSMIC etiology: Spontaneous deamination of 5-methylcytosine (clock-like)
Correlating motif: nCg→nTg
SBS5
COSMIC etiology: Unknown (clock-like)
SBS16
COSMIC etiology: Unknown
Correlating motif: aTn→aCn
Percentage of Single Base Substitutions

Figure S3B

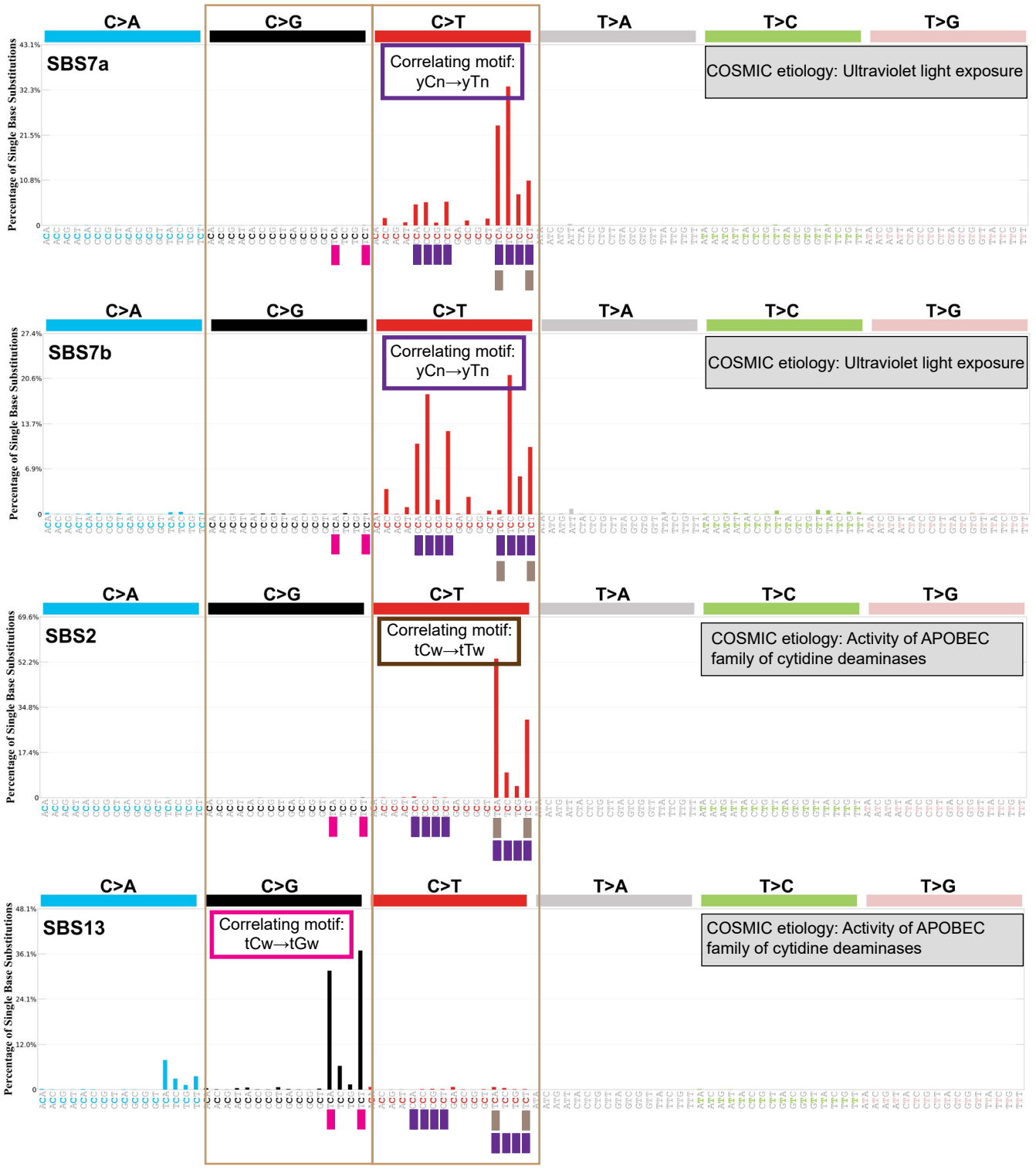
Motif peaks in signatures
yCn→yTn
tCw→tTw
tCw→tGw
C>A
C>G
C>T
T>A
T>C
T>G
SBS7a
Correlating motif: yCn→yTn
COSMIC etiology: Ultraviolet light exposure
SBS7b
Correlating motif: yCn→yTn
COSMIC etiology: Ultraviolet light exposure
SBS2
Correlating motif: tCw→tTw
COSMIC etiology: Activity of APOBEC family of cytidine deaminases
SBS13
Correlating motif: tCw→tGw
COSMIC etiology: Activity of APOBEC family of cytidine deaminases
Percentage of Single Base Substitutions

Figure S4

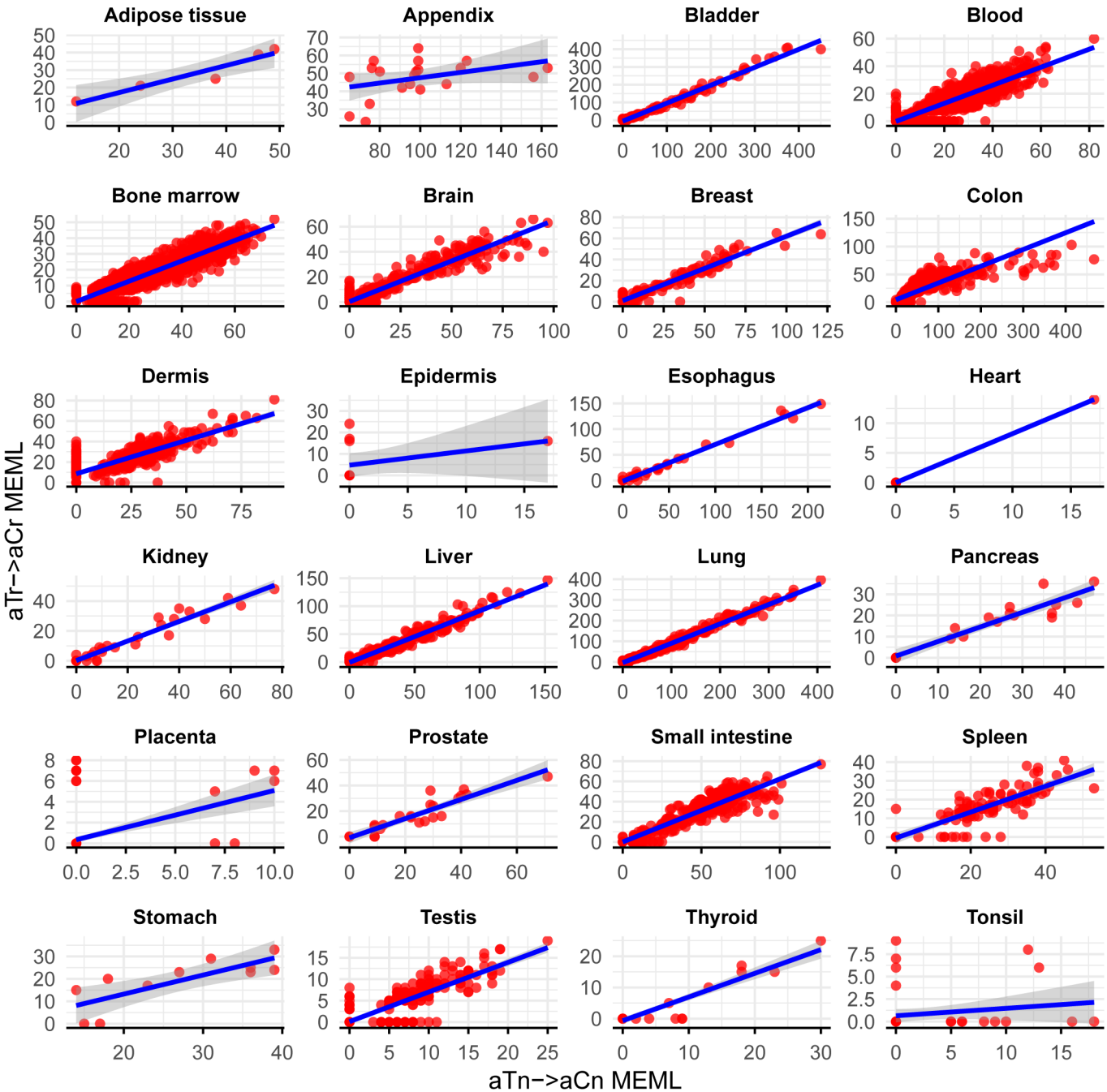
Adipose tissue
Appendix
Bladder
Blood
Bone marrow
Brain
Breast
Colon
Dermis
Epidermis
Esophagus
Heart
Kidney
Liver
Lung
Pancreas
Placenta
Prostate
Small intestine
Spleen
Stomach
Testis
Thyroid
Tonsil
aTr->aCr MEML
aTn->aCn MEML

Figure S5

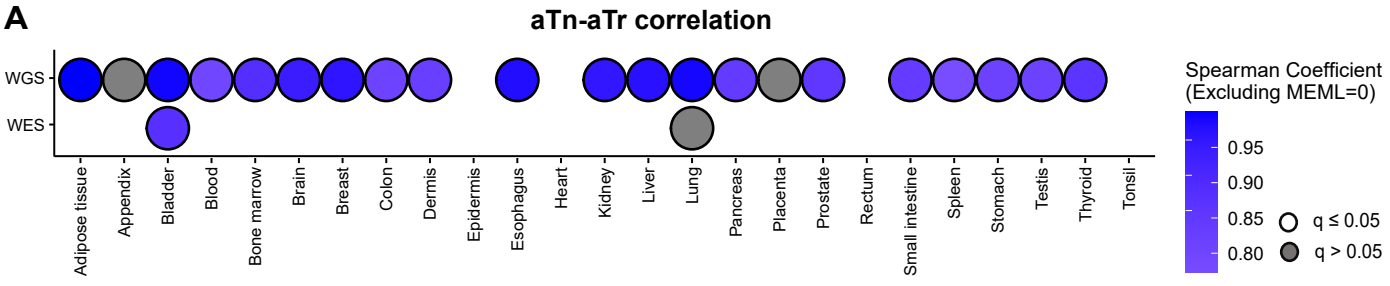
A
aTn-aTr correlation
WGS
WES
Adipose tissue
Appendix
Bladder
Blood
Bone marrow
Brain
Breast
Colon
Dermis
Epidermis
Esophagus
Heart
Kidney
Liver
Lung
Pancreas
Placenta
Prostate
Rectum
Small intestine
Spleen
Stomach
Testis
Thyroid
Tonsil
Spearman Coefficient
(Excluding MEML=0)
0.95
0.90
0.85
0.80
q ≤ 0.05
q > 0.05

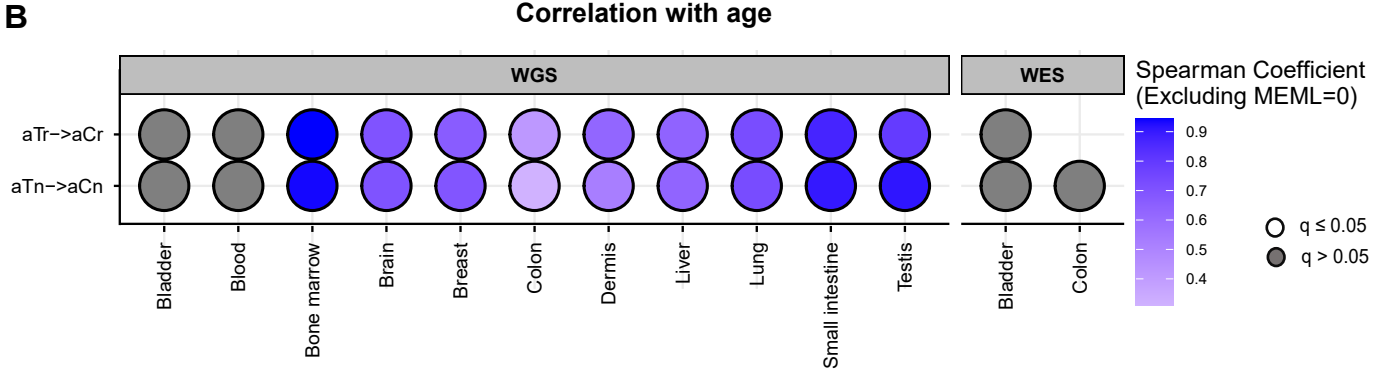
B
Correlation with age
WGS
WES
aTr−>aCr
aTn−>aCn
Bladder
Blood
Bone marrow
Brain
Breast
Colon
Dermis
Liver
Lung
Small intestine
Testis
Bladder
Colon
Spearman Coefficient
(Excluding MEML=0)
0.9
0.8
0.7
0.6
0.5
0.4
q ≤ 0.05
q > 0.05

Figure S6

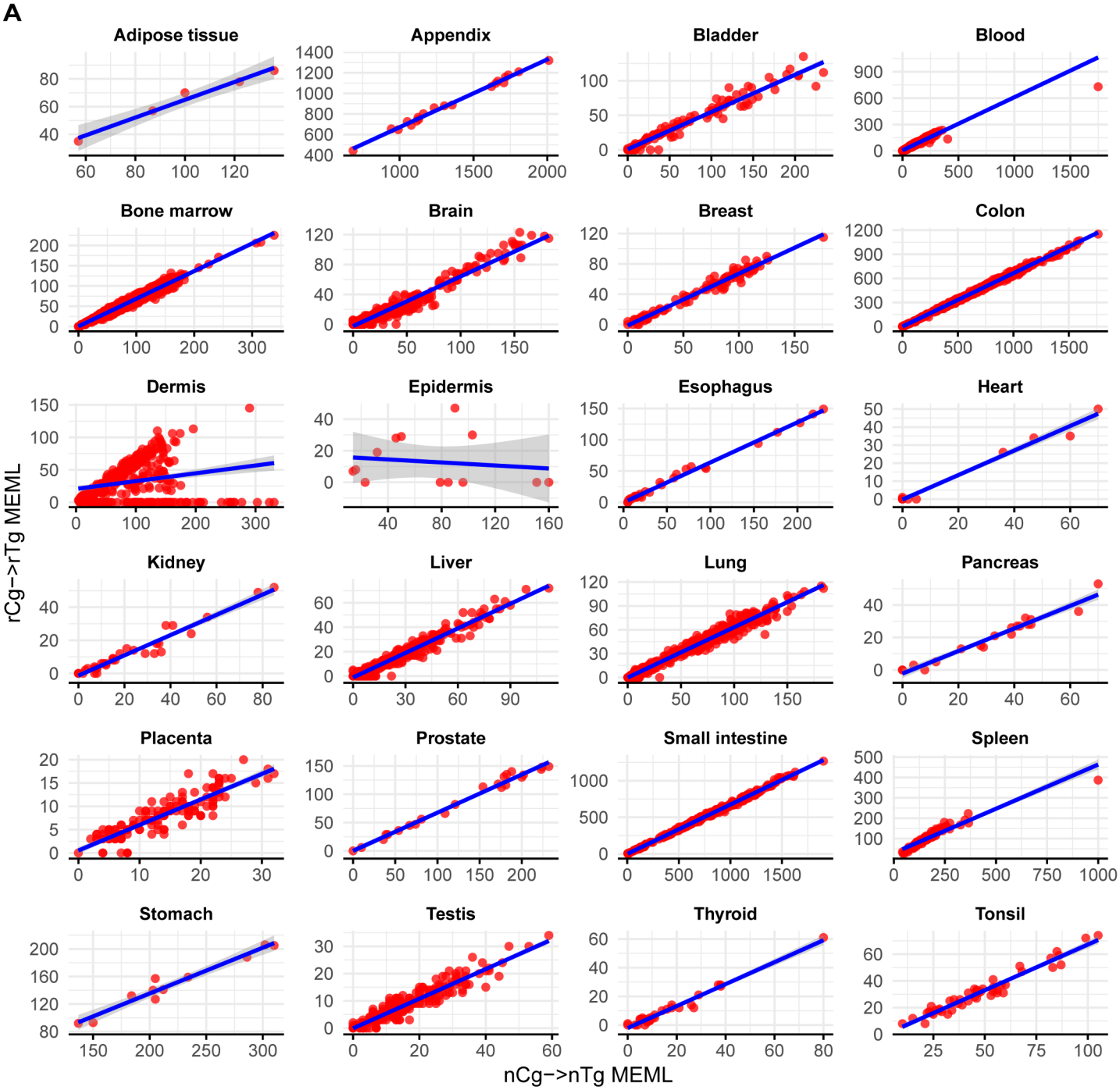
A
Adipose tissue
Appendix
Bladder
Blood
Bone marrow
Brain
Breast
Colon
Dermis
Epidermis
Esophagus
Heart
Kidney
Liver
Lung
Pancreas
Placenta
Prostate
Small intestine
Spleen
Stomach
Testis
Thyroid
Tonsil
rCg->rTg MEML
nCg->nTg MEML

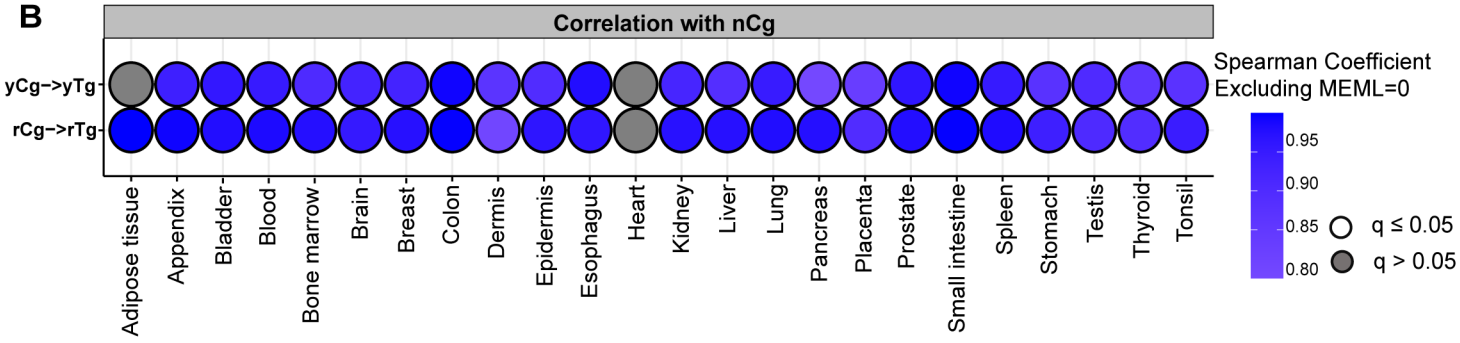
B
Correlation with nCg
yCg->yTg
rCg->rTg
Adipose tissue
Appendix
Bladder
Blood
Bone marrow
Brain
Breast
Colon
Dermis
Epidermis
Esophagus
Heart
Kidney
Liver
Lung
Pancreas
Placenta
Prostate
Small intestine
Spleen
Stomach
Testis
Thyroid
Tonsil
Spearman Coefficient
Excluding MEML=0
0.95
0.90
0.85
0.80
q ≤ 0.05
q > 0.05

Figure S7

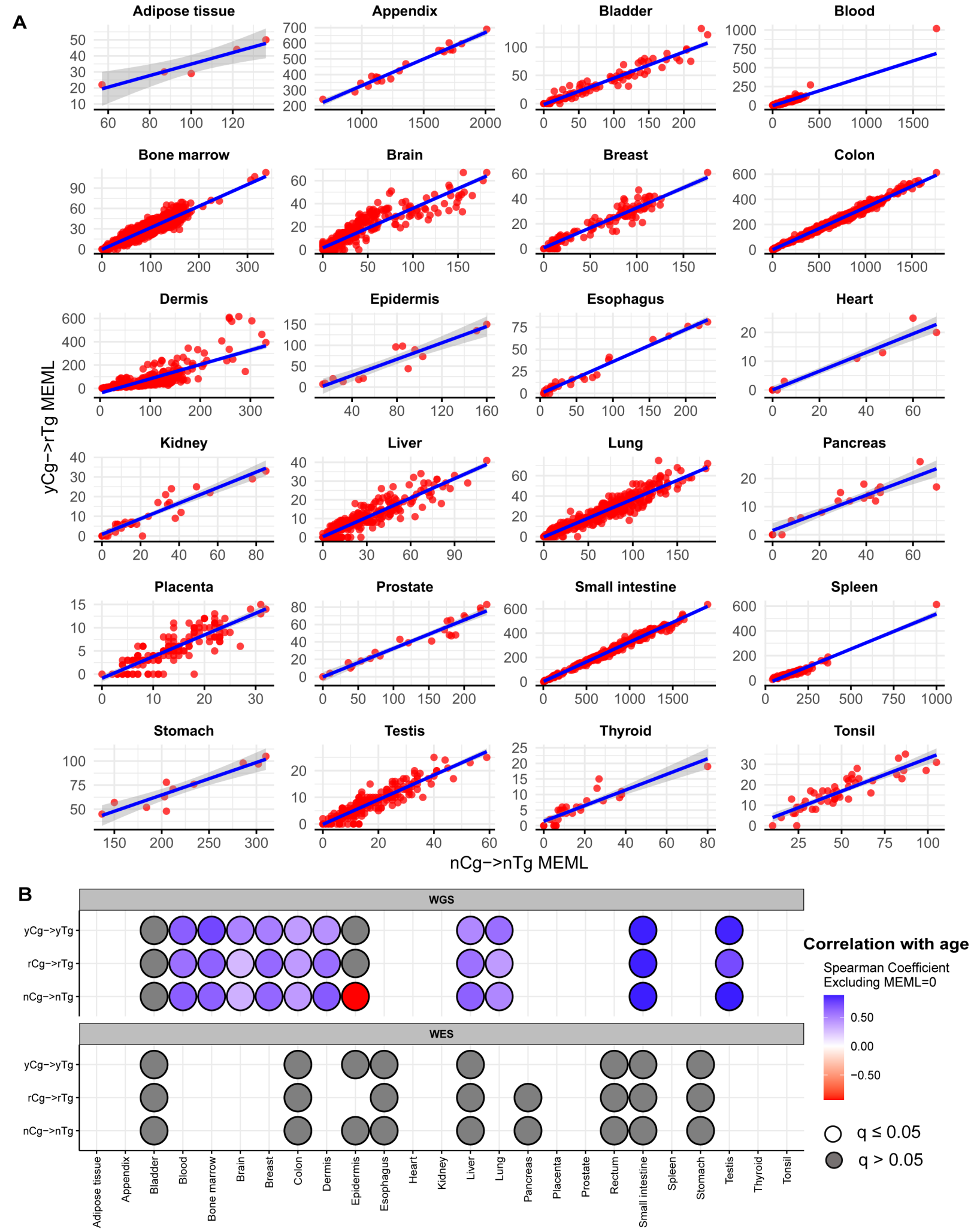
A
Adipose tissue
Appendix
Bladder
Blood
Bone marrow
Brain
Breast
Colon
Dermis
Epidermis
Esophagus
Heart
Kidney
Liver
Lung
Pancreas
Placenta
Prostate
Small intestine
Spleen
Stomach
Testis
Thyroid
Tonsil
yCg->rTg MEML
nCg->nTg MEML
B
WGS
WES
yCg->yTg
rCg->rTg
nCg->nTg
Adipose tissue
Appendix
Bladder
Blood
Bone marrow
Brain
Breast
Colon
Dermis
Epidermis
Esophagus
Heart
Kidney
Liver
Lung
Pancreas
Placenta
Prostate
Rectum
Small intestine
Spleen
Stomach
Testis
Thyroid
Tonsil
Correlation with age
Spearman Coefficient
Excluding MEML=0
0.50
0.00
−0.50
q ≤ 0.05
q > 0.05

Figure S8

A B C D

Bladder

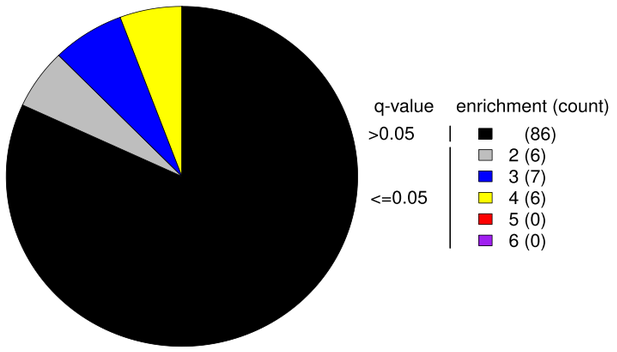

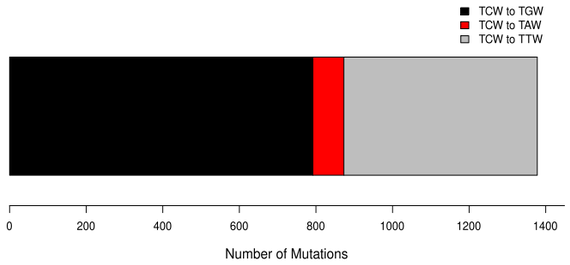

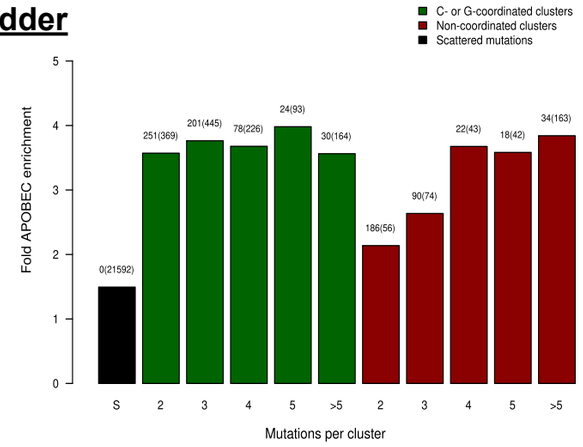

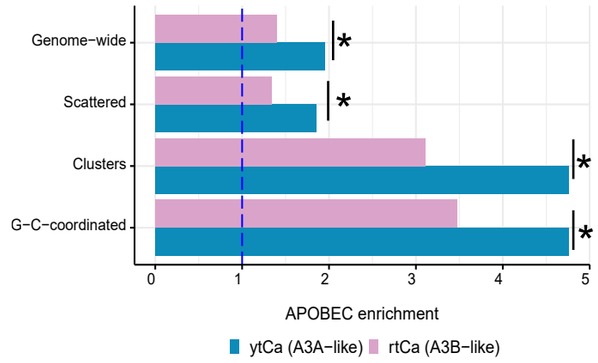

Breast

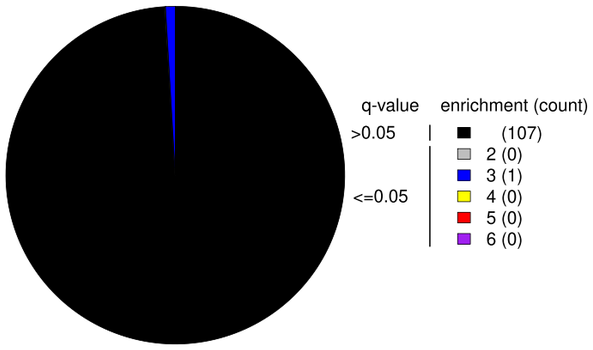

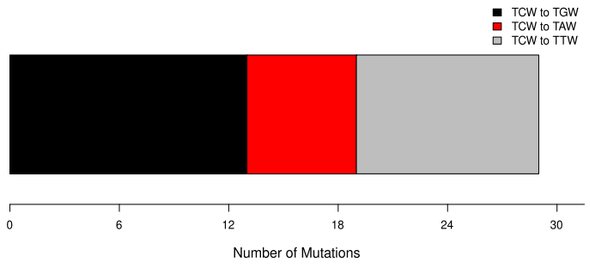

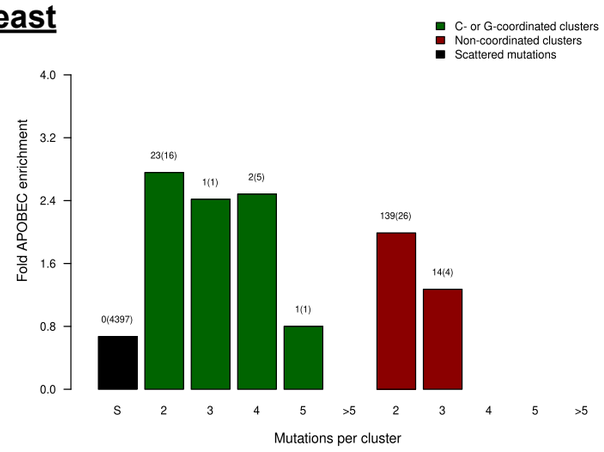

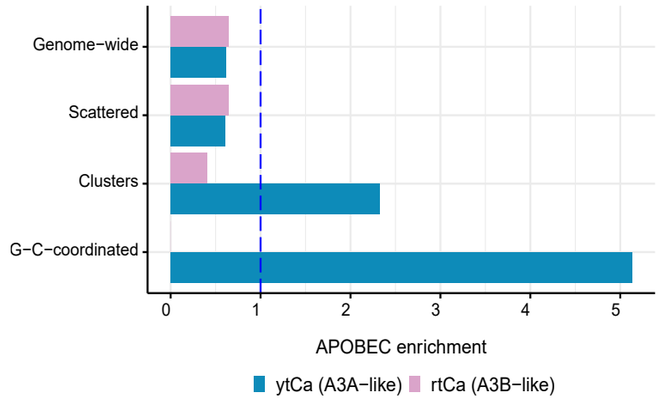

Liver

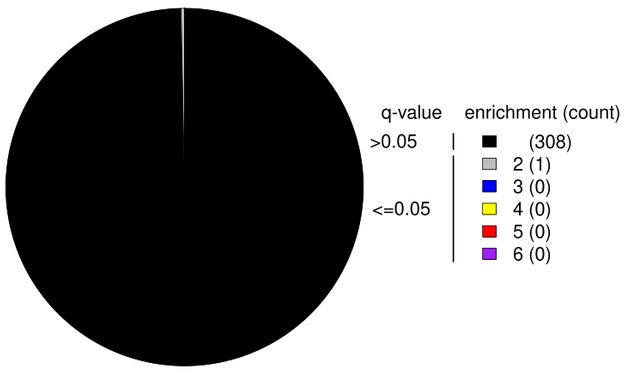

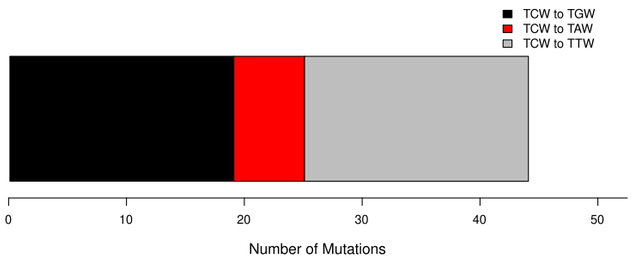

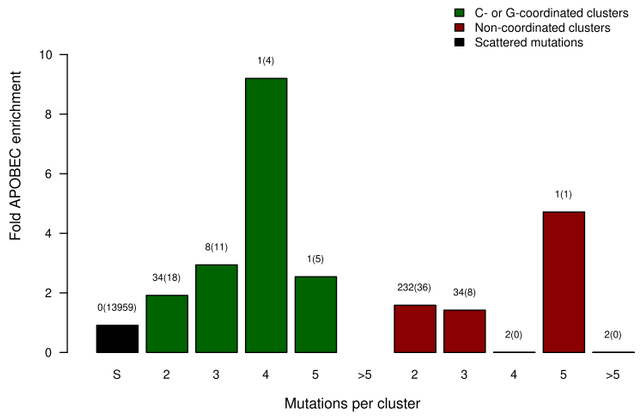

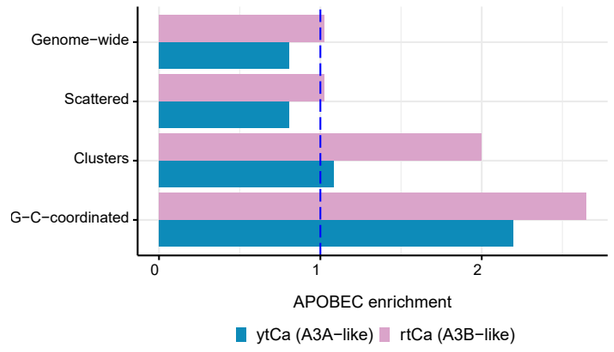

Lung

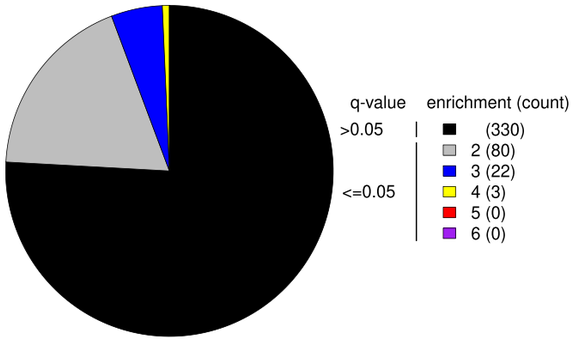

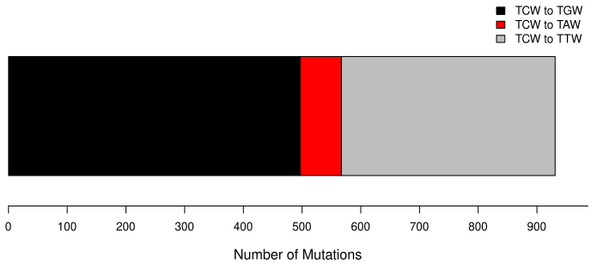

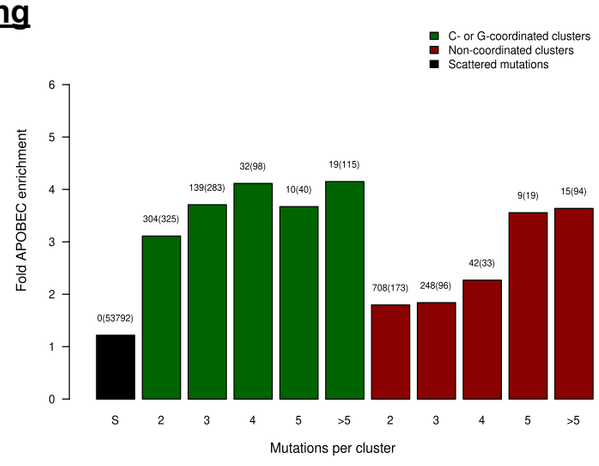

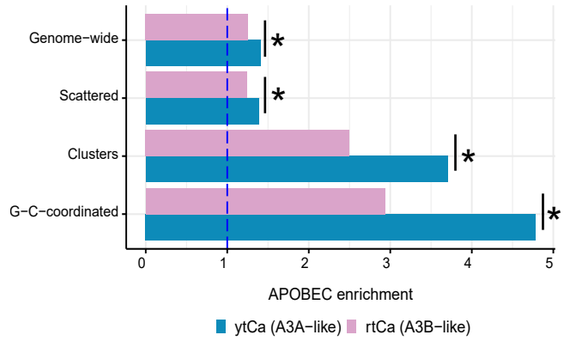

Small Intestine

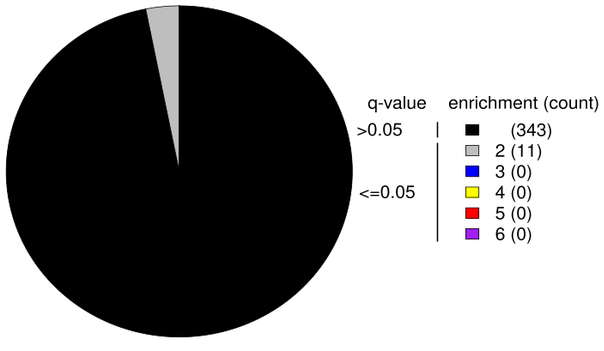

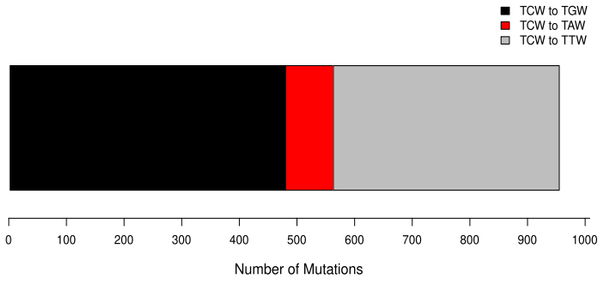

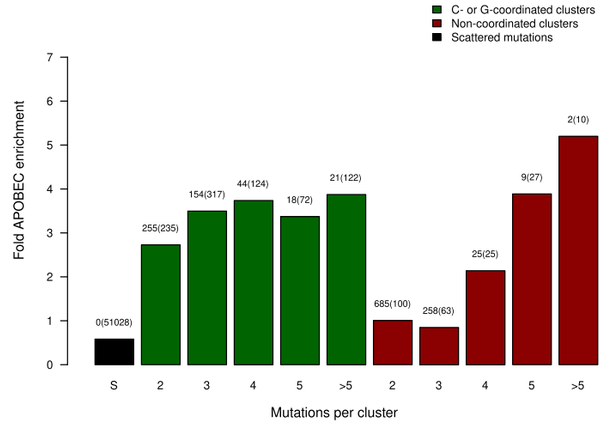

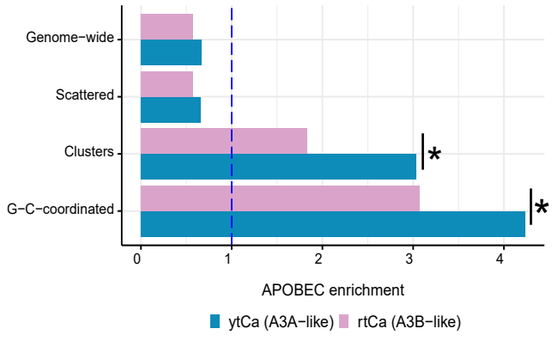

Figure S9

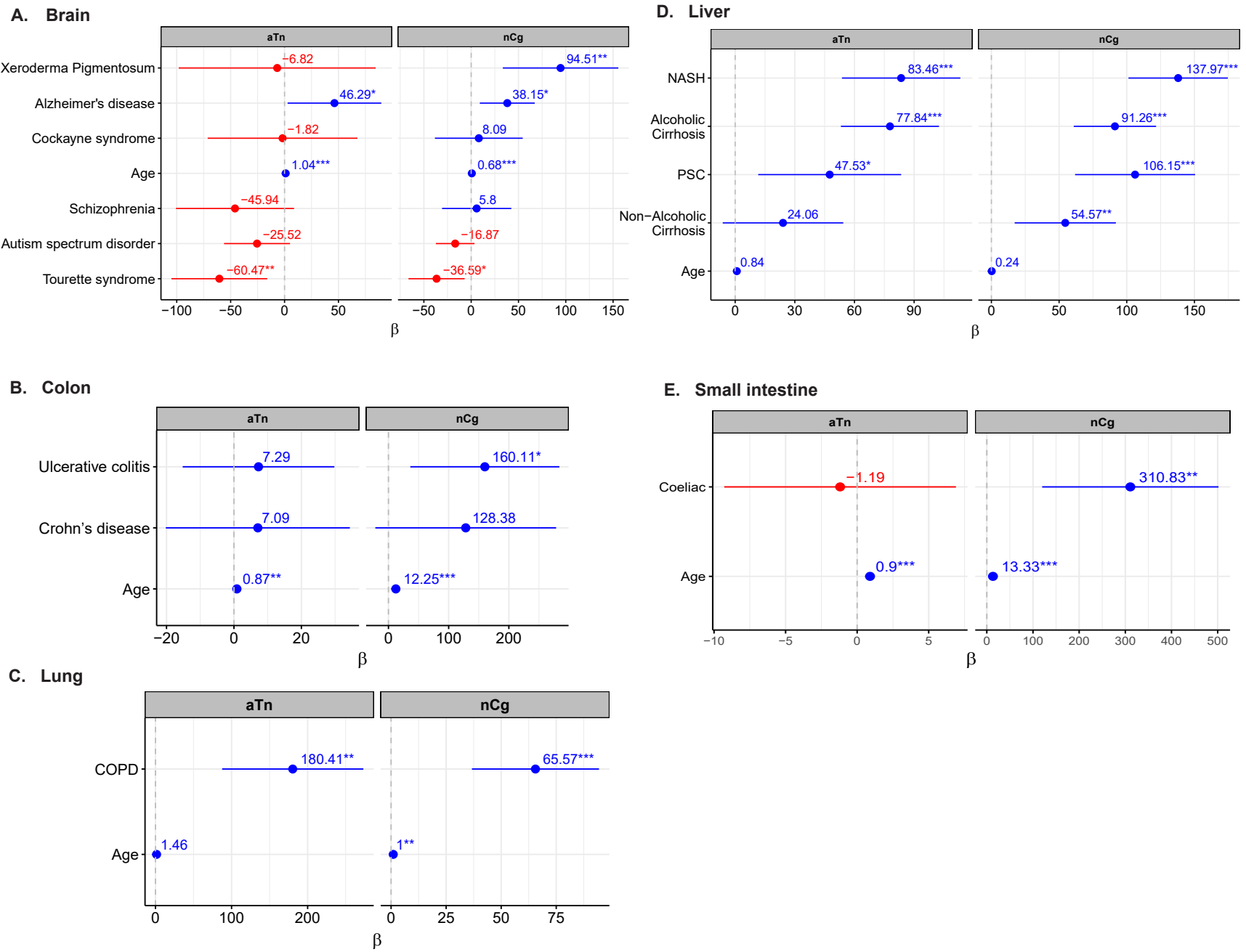
A. Brain
aTn
nCg
Xeroderma Pigmentosum
Alzheimer's disease
Cockayne syndrome
Age
Schizophrenia
Autism spectrum disorder
Tourette syndrome
−6.82
46.29*
−1.82
1.04***
−45.94
−25.52
−60.47**
94.51**
38.15*
8.09
0.68***
5.8
−16.87
−36.59*
−100 −50 0 50
−50 0 50 100 150
β
D. Liver
NASH
Alcoholic Cirrhosis
PSC
Non−Alcoholic Cirrhosis
Age
83.46***
77.84***
47.53*
24.06
0.84
137.97***
91.26***
106.15***
54.57**
0.24
0 30 60 90
0 50 100 150
β
B. Colon
Ulcerative colitis
Crohn's disease
Age
7.29
7.09
0.87**
160.11*
128.38
12.25***
−20 0 20
0 100 200
β
E. Small intestine
Coeliac
Age
−1.19
0.9***
310.83**
13.33***
−10 −5 0 5
0 100 200 300 400 500
β
C. Lung
COPD
Age
180.41**
1.46
65.57***
1**
0 100 200
0 25 50 75
β

Figure S10

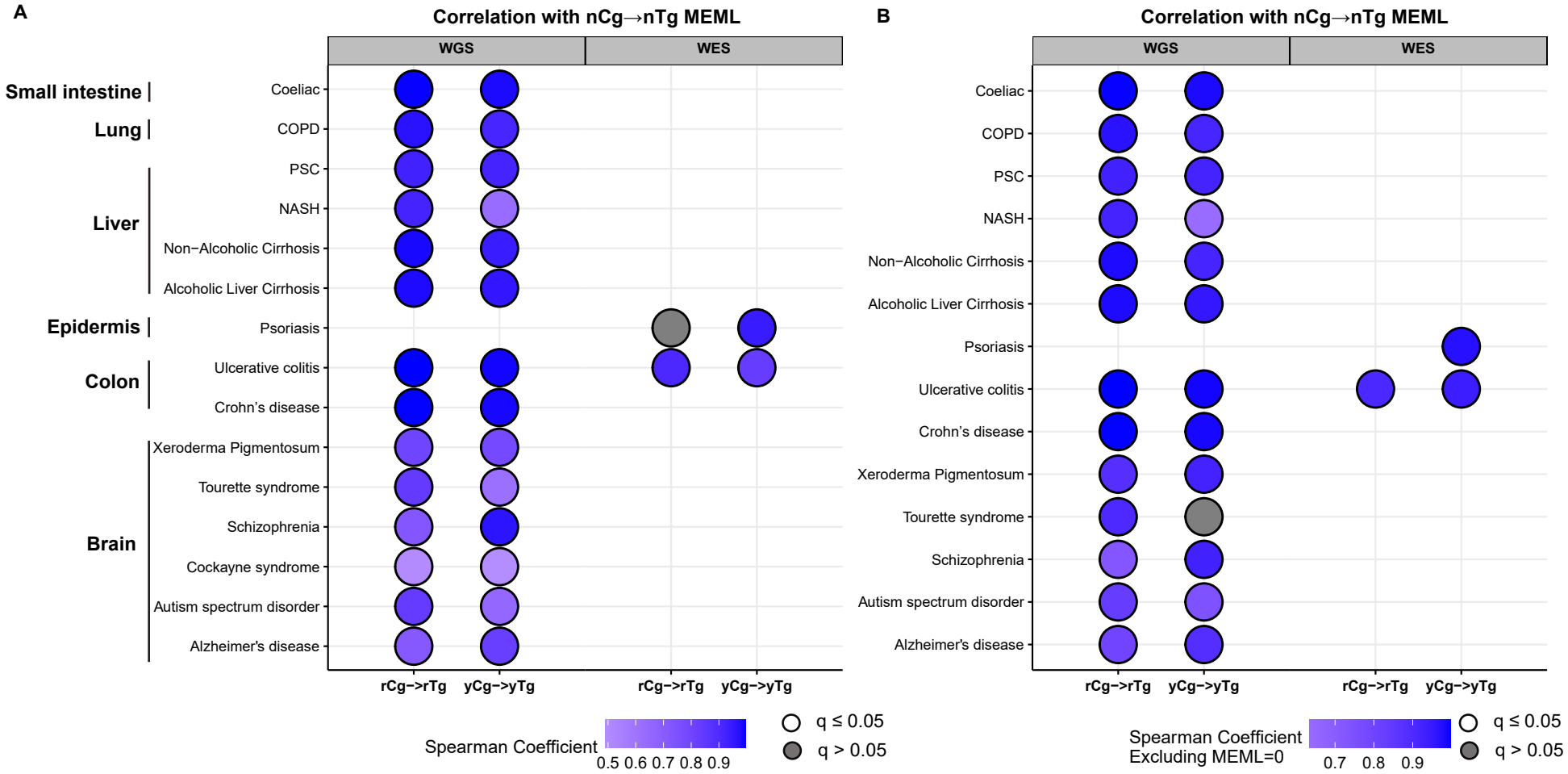
A
Correlation with nCg→nTg MEML
WGS
WES
Small intestine
Lung
Liver
Epidermis
Colon
Brain
Coeliac
COPD
PSC
NASH
Non−Alcoholic Cirrhosis
Alcoholic Liver Cirrhosis
Psoriasis
Ulcerative colitis
Crohn's disease
Xeroderma Pigmentosum
Tourette syndrome
Schizophrenia
Cockayne syndrome
Autism spectrum disorder
Alzheimer's disease
rCg->rTg
yCg->yTg
rCg->rTg
yCg->yTg
Spearman Coefficient
0.5 0.6 0.7 0.8 0.9
q ≤ 0.05
q > 0.05
B
Correlation with nCg→nTg MEML
WGS
WES
Coeliac
COPD
PSC
NASH
Non−Alcoholic Cirrhosis
Alcoholic Liver Cirrhosis
Psoriasis
Ulcerative colitis
Crohn's disease
Xeroderma Pigmentosum
Tourette syndrome
Schizophrenia
Autism spectrum disorder
Alzheimer's disease
rCg->rTg
yCg->yTg
rCg->rTg
yCg->yTg
Spearman Coefficient
Excluding MEML=0
0.7 0.8 0.9
q ≤ 0.05
q > 0.05